

Engineering Documents

University of Pennsylvania

Year 1995

Multiple Light Scattering from Isotropic and Anisotropic Turbid Media

Ming Hsu Kao
University of Pennsylvania,

University of Pennsylvania, Dissertation, 1995.

This paper is posted at ScholarlyCommons@Penn.
<http://repository.upenn.edu/seas.docs/7>

MULTIPLE LIGHT SCATTERING FROM ISOTROPIC
AND ANISOTROPIC TURBID MEDIA

MING HSU KAO

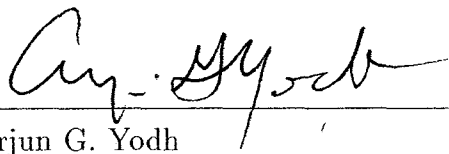
A DISSERTATION

in

DEPARTMENT OF PHYSICS AND ASTRONOMY

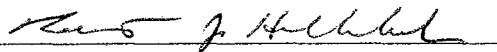
Presented to the Faculties of the University of Pennsylvania in Partial Fulfillment
of the Requirements for the Degree of
Doctor of Philosophy.

1995



Arjun G. Yodh

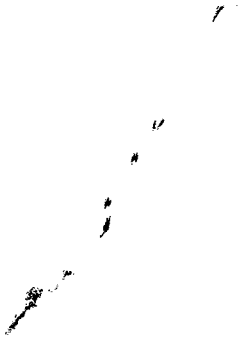
Supervisor of Dissertation



Robert J. Hollebeek

Graduate Group Chairperson

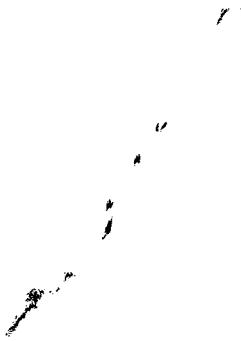
MATH-PHYSICS/QC/001/1995/K17



© Copyright 1995

by

Ming Hsu Kao



To: My Parents and My Wife

Acknowledgements

There are lots of people I should express my appreciation for the accomplishment of this dissertation. The very first person I should thank, of course, is my advisor, Arjun Yodh. Without his support and help, this dissertation would never exist. I also thank Dave Pine for his expert guidance in studying Diffusing-Wave Spectroscopy. Regarding the project of multiple light scattering in nematic liquid crystal, I especially thank Holger Stark and Tom Lubensky for sharing their physical insight with me. Peter Collings is the person I should thank for his contributions to the design of the liquid crystal experiments. I also thank Mohsen Yeganeh, Peter Kaplan, Joe Culver, Jining Qi, Dave Boas, Maureen O'Leary, Tony Dinsmore, Bill Angerer, and Kristen Jester for their help and sharings.

Abstract

Multiple Light Scattering From Isotropic and Anisotropic Turbid Media

Ming H. Kao

Arjun G. Yodh

This dissertation presents three multiple light scattering experiments in isotropic and anisotropic turbid media. Diffusing-Wave Spectroscopy(DWS) and its variants have been applied to study dynamical behavior in these systems and its limitations have been studied in detail.

In the first experiment presented in this dissertation, Diffusing-Wave Interferometry(DWI) is used to investigate Brownian motion on time scales less than the hydrodynamic fluid vorticity diffusion time. We found that the dynamic behavior of the Brownian particle was not well described by the well known Langevin theory which ignores the time-dependent hydrodynamic interactions.

DWS is based on the diffusion approximation for photon transport in strong scattering systems. The diffusion approximation, however, breaks down when the dimensions of the studied sample becomes comparable to the photon transport mean free path in the sample. In some applications of DWS, one does not have control of the sample dimension. For these cases, it is necessary to determine when DWS can be applied accurately. The second experiment in this thesis presents detailed studies of these issues.

DWS has achieved notable success for the study of isotropic turbid media. It

is tempting to extend its application to anisotropic turbid media. In the third experiment presented in this dissertation, we have studied this possibility and found that DWS can be successfully adapted for the study of turbid nematic liquid crystals. We performed static transmission measurements on these systems and we have found that the diffusion coefficient along the direction of director is different from that perpendicular to the direction of director. We were also able to extract useful information of the hydrodynamics about the system via DWS measurements.

Contents

Acknowledgements	iv
1 Introduction	1
1.1 Historical Perspectives	1
1.2 Brief Review of Light Scattering Problem	2
1.3 Physical Properties of Latex Sphere	5
1.4 Brief Introduction of Nematic Liquid Crystal	8
2 Brownian Dynamics on Hydrodynamic Times Scales-A DWS Application	11
2.1 Multiple Light Scattering and Diffusing Wave Spectroscopy(DWS) . .	11
2.2 Formulation of Diffusing-Wave Spectroscopy	16
2.2.1 Single Scattering	16
2.2.2 Multiple Scattering	18
2.3 Brownian Motion in Hydrodynamic Time Scales	25
2.4 Diffusing-Wave Interferometry(DWI)	35
2.5 Experiment Set-up	36
2.6 Results and Conclusions	41
3 Breakdown of DWS	48
3.1 Photon Diffusion Approximation	48
3.2 Practical Considerations in Applying DWS	54

3.3	Experiment Set-up	58
3.4	Results and Conclusions	61
4	Multiple Light Scattering in Nematic Liquid Crystals	69
4.1	Director Fluctuations in Nematic Liquid Crystals	69
4.2	Light Scattering in Nematic Liquid Crystal	76
4.3	Dynamics of the Director Field	84
4.4	Computer Simulation	91
4.5	Experiment set up and results	101
5	Conclusions	108
A	Code List of The Simulation Performed in Chapter 4	109

List of Figures

1.1	A plane wave scattered by a sphere. The incident wave propagates along the Z -axis with its electric field in X -axis and magnetic field in Y -axis. The scattered wave propagates in the direction of $(\sin \theta \cos \phi, \sin \theta \sin \phi, \cos \theta)$. The electric field of the scattered wave can be decomposed into E_ϕ which is the projection on $X - Y$ plane and E_θ which is the projection on the plane specified by Z -axis and \mathbf{k}_f . The diameter of the sphere is comparable to the wavelength of incident wave.	4
1.2	A example of the inter-particle potential in polystyrene sphere suspension: Here we plot potentials between two spheres in a 2000\AA -diameter polystyrene sphere suspension. $V(r)$ represents the interaction energy between two spheres using DLVO potential and $W(r)$ is the van der Waals potential between two spheres. The screen length is 50\AA . r is the distance between the centers of two spheres.	7
1.3	A model system of nematic liquid crystal: \mathbf{n} is the director which is along the average direction of all the molecules.	10
2.1	A simple DWS set-up for the transmission geometry: The Laser impinges as a focused beam on one side of the sample, and the scattered photons are collected from the other side. The signals from PMT is send to an electronic correlator.	15
2.2	An example of single light scattering.	16

2.3	Persistence length in polymer: Each monomer of length l has a bond which makes an angle θ with its neighbor. l^* represents the the length scale over which the polymer bends significantly.	19
2.4	A photon experiences N scattering events: \mathbf{k}_i is the wavevector for the photon propagating from particle (i) at position \mathbf{r}_i to particle ($i + 1$) at position \mathbf{r}_{i+1}	20
2.5	A very short laser pulse is incident from the left-hand side of the sample. The photons are scattered many times before they exit the sample. The output pulse is broadened in time as a result of the fact that photons arrive at different times. The shape of this pulse defines $P(t)$, the probability that a photon takes a time t to emerge from sample.	23
2.6	Multiple Scattering in a correlated system: The scattering is not determined solely by the scatterers themselves.	24
2.7	A simple Michelson Interferometer: The speckle field $E(t)$ is divided at the interferometer entrance, directed along two spatially separated paths of differing length, and then recombined.	35
2.8	Experiment set-up for probing Brownian Motion in hydrodynamic time scales	38
2.9	Examples of intensity scan as a function of time	39
2.10	Measurement result of $g_1(\tau)$	40
2.11	rms displacement as a function of time	44
2.12	Scaled rms displacements	46
3.1	Scattering in isotropic medium: $d\mathbf{S}$ is a surface element located at the origin and with its normal vector in the direction of $+Z$. dV is a volume element located at position \mathbf{r} . $U(\mathbf{r})$ is the photon energy density at position \mathbf{r} . θ is the angle between \mathbf{r} and the normal vector of $d\mathbf{S}$	49

3.2	Photon diffusion in one-dimension	52
3.3	Reflection at boundaries	56
3.4	Experiment set-up in probing the limitation of DWS	59
3.5	In this graph, we show static transmission as a function of cell thickness for different polarization channels. The triangle symbols represent the data obtained with the output polarization parallel to the input polarization. The solid diamond symbols represent the data obtained with the output polarization 45° off the input polarization. The circle symbols represent the data obtained with the output polarization perpendicular to the input polarization.	62
3.6	Results obtained from static and dynamic measurements: l_{DWS}^* is the inverted l^* obtained by fitting the measured $g_1(\tau)$ with eqn. 3.14. l_{Mie}^* is the l^* calculated by using Mie theory and eqn. 2.34. In the static transmission graph, Y-axis is the ratio of the l^* obtained by the procedure described in Section 3.3 to l_{Mie}^* . L is the cell thickness. The meanings of the symbols are the same as in the previous figure	64
3.7	Depolarization thickness as a function of particle diameter: All the samples are prepared with l^* about $140\mu\text{m}$	65
3.8	When can use the plane-wave/slab solution in DWS? The studied sample was a 4.4%, $0.460\mu\text{m}$ -diam. polystyrene spheres suspension with cell thickness $L = 750\mu\text{m}$. The beam diameter was controlled by a variable iris whose diameter ranged from 1 mm to 20 mm	66
3.9	Effect of reflection at boundaries: Dynamical measurement was performed for a 1.6%, $0.460\mu\text{m}$ -diam. polystyrene spheres suspension for various cell thickness. The sample cell was not immersed in water. The inverted l_{DWS}^* was calculated with and without considering the diffusive reflectivity.	67
4.1	A model system of nematic liquid crystal	71

4.2	Three fundamental types of deformation	75
4.3	Light propagation in uniaxial medium: Light propagates with an angular dependent speed. Z-axis is the axis for the extraordinary refractive index	77
4.4	A new \mathbf{q} -dependent, coordinates system: \mathbf{e}_1 is perpendicular to both $\hat{\mathbf{z}}$ and \mathbf{q} and \mathbf{e}_2 is perpendicular to both $\hat{\mathbf{z}}$ and \mathbf{e}_1	79
4.5	Magnetic coherence length	81
4.6	Differential cross-sections for K15 nematic liquid with $\xi = 10\mu m$: The incident direction(+ x -axis) is perpendicular to the direction direction(z -axis). (a) ordinary mode photon scattered into extraordinary mode photon. (b) extraordinary mode photon scattered into ordinary mode photon. (c) extraordinary mode photon scattered into extraordinary mode photon.	85
4.7	Three fundamental geometries for viscosity measurements: (a) director perpendicular to both flow velocity and gradient of flow velocity, (b) director parallel to flow velocity but perpendicular gradient of flow velocity, and (c) director parallel to gradient of flow velocity but perpendicular to flow velocity.	88
4.8	Logical procedures of the simulation	95
4.9	Z-X cross-sectional view of the positional distribution of the photons: (a) $t = 10\text{psec}$ (b) $t = 100\text{psec}$	97
4.10	Z-Y cross-sectional view of the positional distribution of the photons: (a) $t = 10\text{psec}$ (b) $t = 100\text{psec}$	98
4.11	Y-X cross-sectional view of the positional distribution of the photons: (a) $t = 10\text{psec}$ (b) $t = 100\text{psec}$	99
4.12	Results of simulation: (a) Photon diffusion coefficients are derived from eqn. 4.78. (b) The x -component of the averaged photon position approaches a constant value.	100

4.13	Sample holder and cell.	102
4.14	Experiment set-up for measuring anisotropy in photon diffusion . . .	104
4.15	Results of diffusive transmission measurement	105
4.16	Results of dynamical measurements	107

Chapter 1

Introduction

1.1 Historical Perspectives

The Brownian motion of particles in a fluid is a problem with spectacular historical roots [1, 2] and continues to provide us with intriguing new physics. Recently there has been resurging interest in the *first steps* of these motions [3, 4, 5, 6, 7, 8]. This is largely a result of new experimental probes, such as *Diffusing-Wave Spectroscopy*(DWS) [7, 9, 10, 11], that enable us to measure particle displacements down to 1\AA or even smaller, and thereby offer the possibility to quantitatively test hydrodynamic theories [4, 6] of nondiffusive particle motion, especially in the first random walk step. In the first experiment we present here, we use *Diffusing-Wave Interferometry* (DWI)[12, 13] to resolve the mean square displacement, $\langle \Delta r^2(\tau) \rangle$, of particles in hard-sphere suspensions during the first twenty nanoseconds of their motion. These are the shortest time scales ever probed in the study of Brownian dynamics.

Although DWS has been successfully applied in probing dynamics in various system, it has its limits when the dimension of the sample is not much bigger than the *transport mean free path* l^* . In fact, many researchers simply try to insure that the thickness of cell is at least ten times l^* as a rule of thumb. Other factors,

such as input spot size, diffuse reflection, also play important roles in analyzing and interpreting the measured data. Furthermore, DWS is based on the scalar photon diffusion approximation which assumes the input photon is unpolarized. This is generally not true if we use a laser beam as the light source. In the second experiment presented here, we present detailed investigations of these issues.

Multiple light scattering is a complex problem. In isotropic turbid media, we can use the photon diffusion approximation for the case of strong multiple scattering. The simplicity of the photon diffusion approximation allures us to expand its validity to other systems. One might ask, is it possible to use the photon diffusion approximation as well as DWS in an anisotropic turbid media, such as an optically thick liquid crystal? In two recent papers coherent backscattering has been observed from turbid nematics[15, 17], thus strongly indicating the validity of photon diffusion in these systems. In the third experiment of this dissertation, we performed both static transmission measurements and dynamic temporal correlation measurements in K15 nematic liquid crystals. The experimental results suggest that DWS and the photon diffusion approximation can be applied to nematic liquid crystal, though with some interesting modifications. We have also performed computer simulations to investigate the multiple scattering phenomenon in nematic liquid crystals. Our results agree with a rigorous theoretical calculation[18] and corroborate our experimental findings.

1.2 Brief Review of Light Scattering Problem

Light scattering is a physical phenomenon that we encounter every moment while our eyes are open. From the blue sky to the glory sunset, from clear water to turbid milk, almost everywhere, nature guides the light in order to make our life full of colors and wonders. While we are enjoying what nature has endowed us, one might ask questions like: “ Why is the sky blue?”, “ Why does milk look white?”, “ Why does water

look clear?”. All of these questions can be answered when one fully understands “How light propagates through matter”. We know visible light is a propagating electromagnetic field. In different media, light travels at different speeds. From our high school science course, we know Snell’s law which tells us that light changes its direction as it travels from one medium to another medium. This phenomenon can be treated in a more rigorous way by solving Maxwell’s equations. Ideally, we can treat any electro-magnetic field problem with Maxwell’s equations. In practice, however, for only very few cases, can one obtain simple analytical solutions. Let’s look at a superficially simple problem : Plane-wave electro-magnetic fields scattered by a sphere. This problem actually leads to the so called ‘Mie theory’ which offers an analytical solution with pretty complicated form. For the scattering problem sketched in Fig. 1.1 where the incident wave vector \mathbf{k}_i is along the Z -axis and the incident electric field \mathbf{E} is along the X -axis, using Mie theory, the scattered fields can be expressed as[14]:

$$\begin{aligned}
 E_\phi &= -\frac{ie^{ik_f r}}{k_f r} E_o S_1(\theta) \sin \phi, \\
 E_\theta &= \frac{ie^{ik_f r}}{k_f r} E_o S_2(\theta) \cos \phi, \\
 S_1(\theta) &= \sum_{n=1}^{\infty} \frac{2n+1}{n(n+1)} [a_n \pi_n(\cos \theta) + b_n \tau_n(\cos \theta)], \\
 S_2(\theta) &= \sum_{n=1}^{\infty} \frac{2n+1}{n(n+1)} [a_n \tau_n(\cos \theta) + b_n \pi_n(\cos \theta)] \quad (1.1)
 \end{aligned}$$

where $\mathbf{k}_f \equiv (k_f \sin \theta \cos \phi, k_f \sin \theta \sin \phi, k_f \cos \theta)$ is the wave vector of the scattered wave, r is the distance from the sphere, π_n and τ_n are functions related to Legendre polynomials, the a_n and b_n ’s are Mie scattering coefficients. In the limit where the particle size is much smaller than the wavelength, the above results reduce to the well known Rayleigh scattering. Rayleigh showed that, for natural light with incident intensity I_o , the scattered intensity I has the following dependence on the wavelength:

$$I \propto I_o (1 + \cos^2 \theta) \frac{1}{\lambda^4}. \quad (1.2)$$

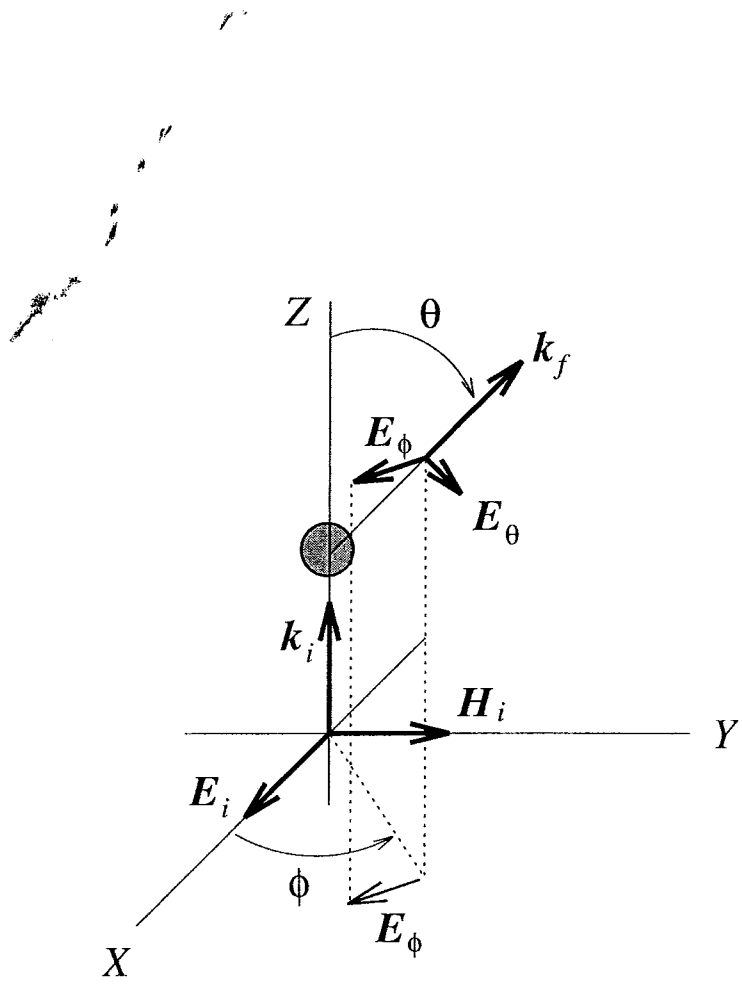


Figure 1.1: A plane wave scattered by a sphere. The incident wave propagates along the Z -axis with its electric field in X -axis and magnetic field in Y -axis. The scattered wave propagates in the direction of $(\sin \theta \cos \phi, \sin \theta \sin \phi, \cos \theta)$. The electric field of the scattered wave can be decomposed into E_ϕ which is the projection on $X - Y$ plane and E_θ which is the projection on the plane specified by Z -axis and \mathbf{k}_f . The diameter of the sphere is comparable to the wavelength of incident wave.

When we look into the clear sky (but not into the sun), the light which enters our eyes has been scattered at least one time. According to eqn. (1.2), since the blue light is much easier than red light to be scattered, most of the light entering our eyes are blue and that explains why the sky looks blue. Similar sorts of arguments can be extended to, though not directly, explain why milk looks white. The scatterers in the milk are about the size of the visible light wavelength and strongly scatter the visible light. The light experiences many scattering events before it emerges from the milk with roughly the same probability whether it is blue or red. Furthermore, multiple scattering processes also cause the incident photons to lose their relative spatial relations. Therefore when we illuminate the milk with white light, it looks white and opaque. The light scattered back into our eyes is diffuse, with little change of spectral content.

Later, the so called *dynamic light scattering* (DLS) technique opened the door for the use of light scattering as a probe of the dynamics of materials. Though success has been achieved, the dynamic light scattering technique is limited to a single scattering sample and the length scale that can be studied is about the order of the wavelength used. About a half dozen years ago, scientists began to investigate the possibility of breaking this limitation. This led to the development of *diffusing-wave spectroscopy* (DWS). Using DWS, the length scale that can be studied dynamically, and can be pushed down to one thousandth of the light wavelength or even lower. In this dissertation, we will discuss both the applications and limitations of DWS.

1.3 Physical Properties of Latex Sphere

In many DWS experiments carried out in this dissertation, the sample used consists of polystyrene spheres in water suspensions. The polystyrene sphere has surface protons attached to sulphonic acid groups at the end of each polystyrene chain which lie on the surface of the sphere. When mixed with water, these protons dissociate

from the sphere and thus the sphere is negatively charged and surrounded by counter-ions in the water. The Coulomb repulsion between spheres is significantly modified by the screening effect caused by these counter-ions. One can also add acid to the suspension to change the screening length.

The interactions between suspended polystyrene spheres are quite complicated. Actually, there are four kinds of interactions: hard sphere repulsion, screened Coulomb repulsion, van der Waals attraction and hydrodynamic interactions. The hard sphere repulsion is required to assure these spheres are not penetrable. The screened Coulomb repulsion can be modeled by the Debye-Huckel potential[19, 20]:

$$V(r) = \frac{Z^* e^2 e^{-\kappa r} e^{2\kappa R}}{\epsilon r (1 + \kappa R)^2}, \quad (1.3)$$

where $Z^* e$ is the effective charge on the surface of the sphere, κ is the inverse screening length, R is the radius of sphere, and ϵ is the dielectric constant of water. The van der Waals potential between two spheres is given by

$$V(r) = -A \left[\frac{4R^2}{(r^2 - 4R^2)} + \frac{4R^2}{r^2} + 2 \ln \left(\frac{r^2 - 4R^2}{r^2} \right) \right], \quad (1.4)$$

where A is the Hamaker constant. For polystyrene sphere suspension, A is in the order of 10^{-13} erg. As we add up all these interactions, the total potential is quite interesting. Fig. 1.2 shows what a typical inter-particle potential looks like in the polystyrene sphere suspension. To be more quantitative, let's take the following example: $2R \sim 0.1 \mu m$, $Z^* e \sim 300$. The van der Waals attraction dominates in the region $< 20 \text{ \AA}$ from the sphere surface with primary minimum about $800 k_B T$ deep. At distance $> 20 \text{ \AA}$, the screened Coulomb repulsion dominates with a barrier as high as $250 k_B T$. Typically, the barrier makes the primary minimum inaccessible, and the polystyrene spheres are stable against flocculation. As we have mentioned, we may change the concentration of the counter-ions to modify the Coulomb repulsion. For example, if we increase the concentration of counter-ions to 10^{16} cm^{-3} by adding HCl, the Coulomb barrier height will decrease to only about $10 k_B T$. At the same time, the screening length decreases as well. To model the polystyrene sphere suspension

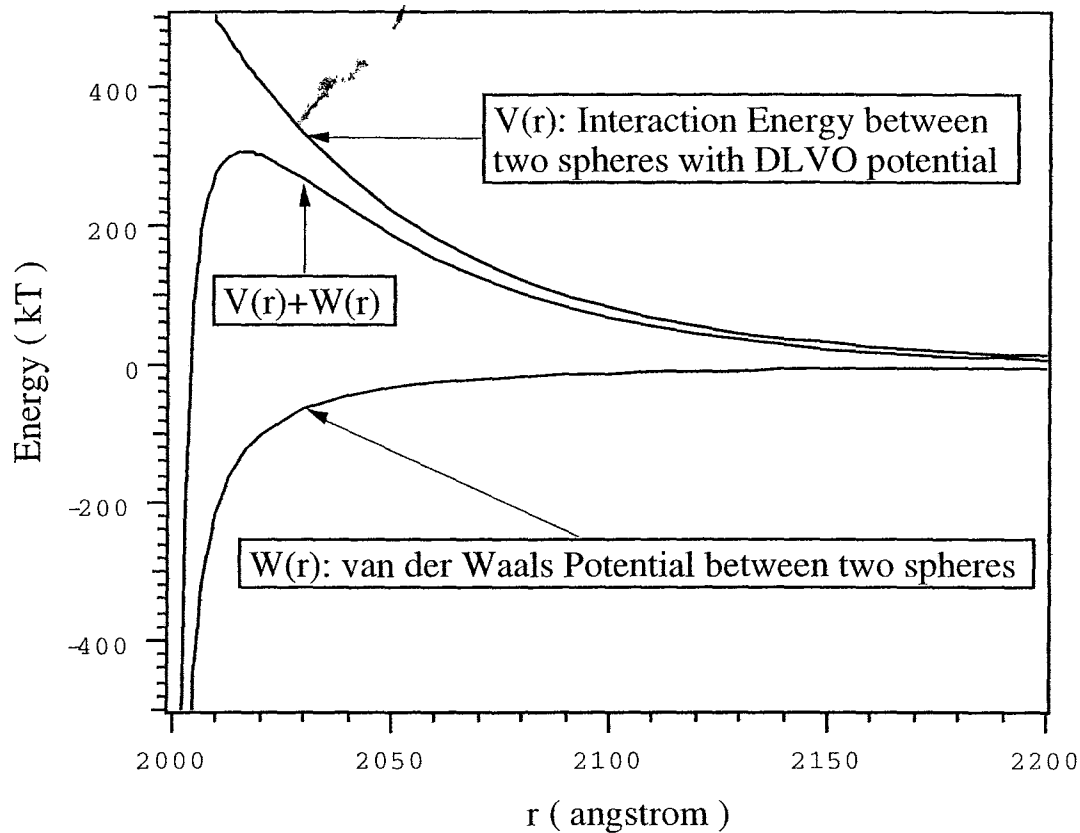


Figure 1.2: A example of the inter-particle potential in polystyrene sphere suspension: Here we plot potentials between two spheres in a 2000\AA -diameter polystyrene sphere suspension. $V(r)$ represents the interaction energy between two spheres using DLVO potential and $W(r)$ is the van der Waals potential between two spheres. The screen length is 50\AA . r is the distance between the centers of two spheres.

as a hard sphere system, we should control the concentration of the counter-ions in the range that provides short screening length while maintaining a high enough Coulomb barrier to avoid flocculation. In the experiments we will discuss later, the screening length of the polystyrene suspension is kept at about 50 Å and the barrier height is kept above $200k_B T$.

Depending on the volume fraction of the polystyrene spheres and the ion concentration in the suspension, the polystyrene spheres suspension exhibits some interesting phases. Such as colloidal crystal, fluid and glass phases [19, 20]. The interested reader should refer to the listed references at the end of this dissertation and the references therein for more details.

1.4 Brief Introduction of Nematic Liquid Crystal

Liquid crystals are materials with unusual optical properties. From the LCD display on the watch to the flat color panel on the expensive note-book computer, scientists and engineers control the way that photons propagate within the liquid crystal to display the information in a perceivable form. In general, the difference between crystal phases and liquid phases arises from the degree of order the material possesses. Liquid crystals, are not like ordinary crystals which possess three-dimensional positional order. Sometimes they possess no positional order, sometimes they possess one- or two-dimensional order. According to the order they possess, we can separate the liquid crystals into three categories

1. *nematic phase*: the material has no positional order but directional order; the system can be described as a bundle of sticks.
2. *smectic phase*: the material has one-dimensional order; the system can be viewed as a set of two-dimensional liquid layers stacked on each other with a well defined spacing.

3. *columnar phase*: the material has two-dimensional order; the system can be described as a two-dimension array of liquid tubes.

In general, as a liquid crystal is heated up above its critical temperature, it loses its directional order and enters its *isotropic phase*. The type of liquid crystals that may be observed depends on the structure of the constituent molecules or group of molecules. Nematics and smectics are usually composed of elongated objects while most columnar phases and some nematics are composed of disk-like objects. Typically, four types of molecules or groups of molecules can be the building block of the liquid crystal. They are:

1. rod-like or disk-like small organic molecules, for which an amphiphilic character may or may not be crucial. They are commonly characterized as *thermotropic*.
2. rods in a liquid substrate. The temperature effects are difficult to control due to the fact that these rods are easily destroyed by the increase of temperature. Usually, we can only adjust the concentration of the rods to induce the phase transition. Such systems are called *lyotropic*.
3. main-chain or side-chain polymers that are thermotropic mesogens. Besides the temperature, the molecular weight may also be used as a control parameter to induce the phase transition.
4. amphiphilic compounds. Typical examples of such structures are found in the soap-water system. These systems may be thermotropic or lyotropic, depending on either the mesomorphic behavior induced by temperature change in the pure phase or the presence of a selective solvent.

In the experiment which will be discussed in chapter 4, the liquid crystal used is nematic. Therefore, we will only discuss the properties of nematic liquid crystal. For other types of liquid crystal, the interested readers are encouraged to read some excellent books regarding this topic [40]. Fig. 1.3 is a schematic representation of the order of a nematic phase. As been mentioned above, there is no positional order in nematic phase. There is, however, some order in the direction of the molecules

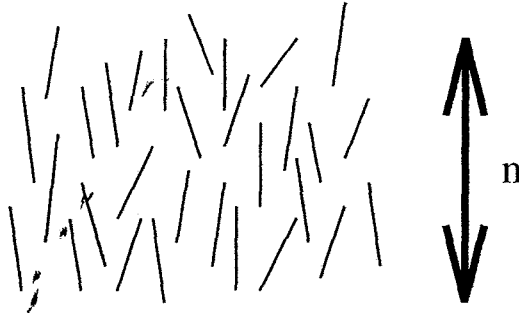


Figure 1.3: A model system of nematic liquid crystal: \mathbf{n} is the director which is along the average direction of all the molecules.

due to the tendency that each molecule has to lay parallel to other molecules. This phenomenon gives the system a preferred direction which is specified by an unit vector \mathbf{n} . We call \mathbf{n} the *director*. Macroscopically, this phenomenon is reflected in measurable quantities such as the dielectric tensor. The difference in the refractive indices measured with polarization parallel or normal to \mathbf{n} is usually quite large. For all known nematic systems, there appears to be complete rotational symmetry about the axis \mathbf{n} . Another important feature of the nematic system is that the state of director \mathbf{n} and $-\mathbf{n}$ are indistinguishable. This indistinguishability arises from the requirement to minimize the internal energy of the system. Furthermore, nematic phases only exist in those materials that do not distinguish between left and right. The material should either be composed of molecules that are identical to their own mirror image, or be a (1:1) mixture of the left- and right-handed species.

The directional order in nematics give rise the anisotropies in physical quantities, such as dielectric constant. In general, the speed of light in a nematic liquid crystal depends on the propagation direction as well as the polarization direction. These anisotropies decrease as temperature increases. Above the critical temperature, the directional order is total destroyed and the anisotropies disappear.

Chapter 2

Brownian Dynamics on Hydrodynamic Times Scales-A DWS Application

Diffusing-Wave Spectroscopy(DWS)[9, 10, 11] has proved to be a powerful technique in probing the dynamics of various systems. It has made possible the measurement of Brownian particle movements on length scales much shorter than the wavelength of light[7, 8, 13]. In this chapter, we will discuss the theoretical foundation of DWS as well as its experimental realization. We will also present a combination of DWS and Michelson Interferometry[12, 13], which enables experiments to probe Brownian dynamics on the time scales of order of the first random walk step. Our results reveal that memory effects in particle hydrodynamics are important at early times.

2.1 Multiple Light Scattering and Diffusing Wave Spectroscopy(DWS)

Light scattering problems have been investigated for over a century. The light scattering phenomenon basically results from inhomogeneities in the dielectric constant

of the media in which the light is propagating. In a suspension system, the inhomogeneity in the dielectric constant originates from the index mismatch between the suspended scatterer and its supporting fluid. The magnitude of the index mismatch determines how strong the scattering will be. Also, the ratio of the diameter of suspended scatterer and the wavelength of the incident light defines the angular dependence of the scattering as well as the scattering cross-section. For example, if the size of the scatterer is much smaller than the wavelength of the incident light, then the photon will be scattered nearly isotropically. On the other hand, if the size of the scatterer is comparable to the wavelength of the incident light, the photon will be scattered mainly in the forward direction.

When we illuminate a suspension sample with a coherent light source (like a laser) and project the scattered light onto a screen, we see a fast fluctuating bright-dark pattern which is called laser speckle. This speckle pattern will be static in time, if the scatterers in the sample are fixed in space. The speckle pattern will fluctuate, however, in a suspension where the scatterers move due to the thermal agitation. If we collect the intensity signal at a particular point in the fluctuating speckle pattern and measure its autocorrelation function, we find that the intensity temporal autocorrelation function decays in a characteristic time. This decay time is directly related to the motion of the scatterers, since the fluctuations originate from the movement of scatterers.

The technique utilizing the phenomenon outlined above has developed into a very powerful tool for the study of the dynamic behavior of a suspension of particles or macromolecules. It has traditionally been called *dynamic light scattering*(DLS) or *quasi-elastic light scattering*(QELS)[16]. The characteristic decay time of the correlation function is set by the wavelength used. Motion of the scatterers on this length scale leads to a change in the photon optical path length and results in a change in the phase of the detected light. DLS, however, is limited by the strict requirement of the single scattering limit. If photon is scattered even a second time,

the intermediate scattering vector is unknown, thus precluding a simple, meaningful interpretation of the measured decay time of the autocorrelation function of the scattered light.

In another limit, the photon may scatter many, many times before it exits the suspension, and the direction of the photon is totally randomized. In this case, the propagation of the photon and the dynamics of the studied medium may both be treated with statistical approximations. The technique that results is called *Diffusing-Wave Spectroscopy*(DWS). The decay of the temporal autocorrelation function of the multiply-scattering light fields, just as for DLS, results from time-dependent changes in the phase or a change in the pathlength of the scattered light fields. The change in the pathlength, however, is effected by all the scatterers in the path, and thus the length scale probed by DWS will be on the order of the wavelength divided by the square root of the number of scattering events. If the number of scattering events is very large, it is possible to push this length scale down to the sub-Å regime. The calculation of the phase change, and hence the temporal autocorrelation function, uses two fundamental approximations. One approximation is concerned with the description of photon propagation through the scattering medium. The other approximation is in the treatment of the dynamics of the scatterers and their effect on the fluctuation of the phase of the emerging light fields. In the limit of very high multiple scattering, each photon is scattered a huge number of times and its movement can be viewed as random walk. As is well known, random walk problems can be described by the diffusion equation in the limit of large step number[21]. This approximation neglects any interference effects of the photon as it propagates through the scattering medium and assumes the photon intensity or light energy density diffuses. To neglect the interference effects within the medium, we assume that the photon scattering is not so strong as to approach the localization limit of the photon due to random scattering. In virtually every instance of practical importance, this approximation is acceptable. The validity of using diffusion approximation enables

us to calculate the distribution of the lengths of the paths taken by the photons propagating through the medium.

A DWS experiment typically measures the temporal autocorrelation function of the intensity fluctuations of the scattered fields. To interpret the data obtained in the experiment, we must derive an expression for the electric field temporal autocorrelation function in terms of the physical quantities of the scattering medium and the light source. The prescription we will follow is quite straightforward. We will approximate the photon propagation through the highly scattering medium as a diffusive process. That is to say that we can describe the photon propagation by the so called *photon diffusion equation* which is given by

$$\frac{\partial U(\mathbf{r}, t)}{\partial t} = D_\gamma \nabla^2 U(\mathbf{r}, t), \quad (2.1)$$

where D_γ is the *photon diffusion coefficient* and $U(\mathbf{r}, t)$ is the light energy density at position \mathbf{r} and time t . This approximation enables us to determine probability distribution of paths through the medium. To determine the correlation function of fields along a particular path, we replace each individual scattering event by an “average scattering event”, and then sum over the scattering events. This will allow us to calculate the contribution of the individual paths to the correlation function. In the final step, the correlation function is determined by summing the contributions of all the individual photon paths weighted by the probability that a photon follows that path. This latter step utilizes solutions to eqn. 2.1 for the given source-detector configuration. The approach described above is not unique; there are more rigorous approaches based on a diagrammatic description of the photon transport which have the advantage in also being able to describe the behavior of photon localization and higher order correlation effects[25, 38].

To illustrate the mentioned approach in more detail, let’s look at a specific example. In Fig. 2.1, we show a typical set-up for a DWS experiment. This set-up is for the transmission geometry wherein the laser impinges as a focused beam on one side of the sample, and the scattered photons are collected from the other side.

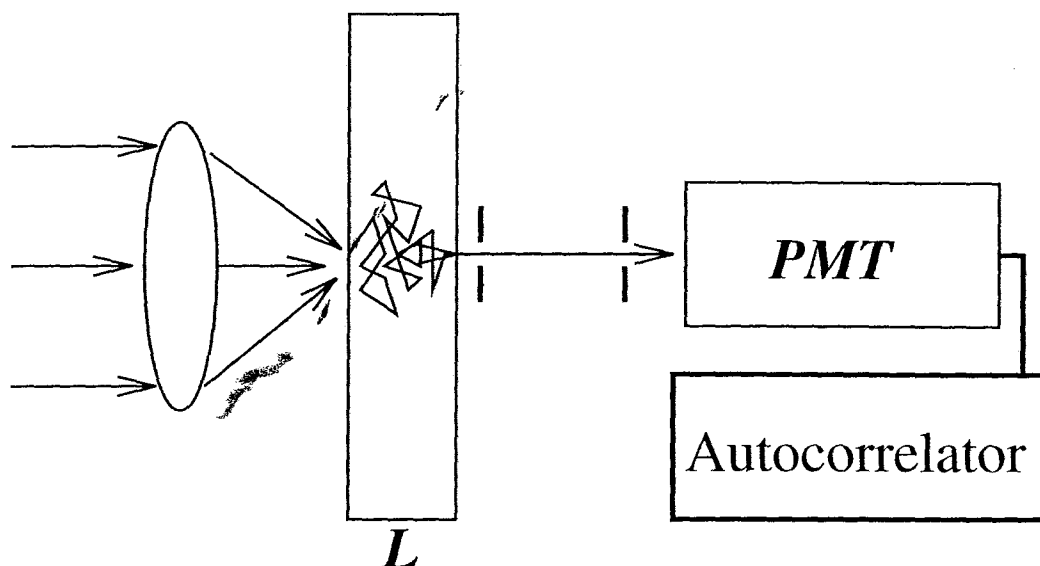


Figure 2.1: A simple DWS set-up for the transmission geometry: The Laser impinges as a focused beam on one side of the sample, and the scattered photons are collected from the other side. The signals from PMT is send to an electronic correlator.

The geometry of the sample is a slab with a thickness L and a lateral extent much greater than the thickness. The signal is collected from a single speckle spot defined by two pin holes as shown in Fig. 2.1. The fluctuating signal is analyzed with a digital photon correlator. For simplicity, we begin by considering a colloidal suspension with a high concentration of scattering particles to ensure that transmitted photons are multiply scattered. In this case, the photon propagation process can be viewed as a random walk process. In the continuum limit, we will use diffusion equation to determine the distribution of photon pathlengths.

If we consider only the temporal correlation function for light traveling along a particular path, we will find its decay rate is related to the average scattering event for this path. Statistically, the photon travels an average distance l before it is scattered. This average distance l is called the photon mean free path. When each scattering event is considered independent of others, the temporal correlation function for a specific path should have a temporal decay rate proportional to the ratio of the pathlength s to mean free path l (i.e. to $N = s/l$ =the number of scattering events

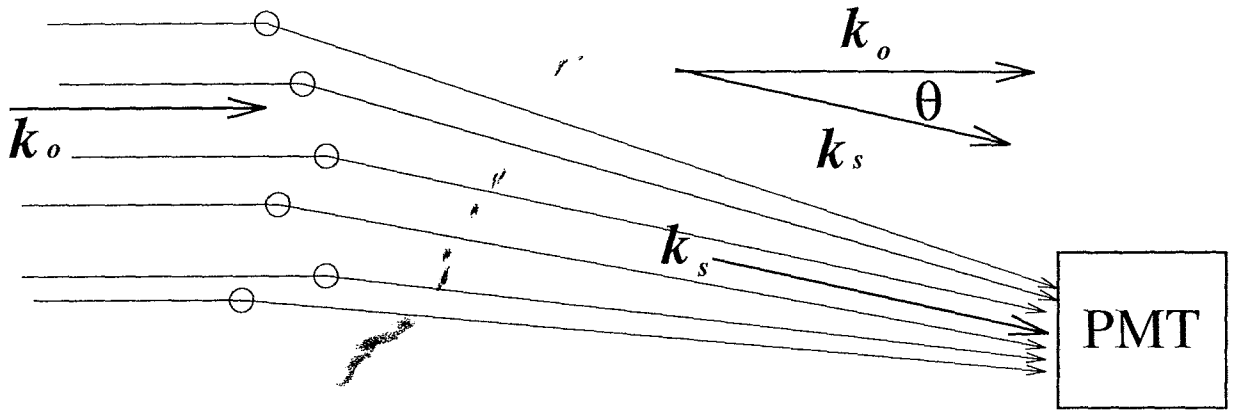


Figure 2.2: An example of single light scattering.

in the sequence). The total correlation function is then calculated by summing over the contributions of all paths weighted by the probability distribution of pathlengths $P(s)$ for the particular input/output/source/detector configuration. By solving the photon diffusion equation with proper boundaries conditions, one can obtain $P(s)$. In experiments, the timescales of measurement are set by the time it takes for the *average photon pathlength* to change by approximately one wavelength as a result of particle motion.

2.2 Formulation of Diffusing-Wave Spectroscopy

2.2.1 Single Scattering

Before we develop the mathematical formulation of diffusing-wave spectroscopy, let's review the simple case of conventional dynamic light scattering experiment as shown in Fig. 2.2.1. The sample system is a monodisperse suspension of non-interacting colloidal spheres which is illuminated by the laser light with an incident wave vector \mathbf{k}_o . The concentration of the suspension is low enough so that the photon is scattered no more than once before passing through the sample. The scattered photons with a wavevector \mathbf{k}_s are detected far from the sample. The detected field is a superposition

of the scattered fields from all N particles in the scattering volume, i.e.

$$E(\tau) = \sum_{i=1}^N E_o \exp[i\mathbf{q} \cdot \mathbf{r}_i(\tau)], \quad (2.2)$$

where \mathbf{q} is the scattering wavevector given by $\mathbf{q} = \mathbf{k}_s - \mathbf{k}_o$ and $\mathbf{r}_i(\tau)$ is the position of i th particle. The electric field autocorrelation function $g_1(\tau)$ is defined as

$$g_1(\tau) = \frac{\langle E(t)E^*(t+\tau) \rangle}{\langle |E(t)|^2 \rangle}, \quad (2.3)$$

where $\langle \dots \rangle$ indicates an average over measurement time t . Inserting eqn. (2.2) in eqn. (2.3), we have[16]

$$g_1(\tau) = \frac{\sum_{i,j}^N \langle \exp\{i\mathbf{q} \cdot [\mathbf{r}_i(0) - \mathbf{r}_j(\tau)]\} \rangle}{\sum_{i,j}^N \langle \exp\{i\mathbf{q} \cdot [\mathbf{r}_i(0) - \mathbf{r}_j(0)]\} \rangle}. \quad (2.4)$$

For the system with non-interacting(i.e. uncorrelated) particles, all the cross terms vanish and we have

$$g_1(\tau) = \langle \exp[-i\mathbf{q} \cdot \Delta\mathbf{r}(\tau)] \rangle, \quad (2.5)$$

where $\Delta\mathbf{r}(\tau) = \mathbf{r}(\tau) - \mathbf{r}(0)$ is the particle displacement in time τ . If $\Delta\mathbf{r}$ is a Gaussian random variable, then from central-limit theorem we have

$$g_1(\tau) = \exp[-q^2 \langle \Delta r^2(\tau) \rangle / 6]. \quad (2.6)$$

For the case of simple particle diffusion, we have $\langle \Delta r^2(\tau) \rangle = 6D\tau$, where D is the particle diffusion coefficient, and the above equation has a very simple form

$$g_1(\tau) = \exp[-q^2 D\tau]. \quad (2.7)$$

This equation suggests that we may probe the diffusive dynamics of the suspension system by measuring the decay rate of the scattered electric field temporal autocorrelation function. In practice, however, it is the intensity autocorrelation function that is usually measured. The intensity autocorrelation function is defined as

$$G_2(\tau) \equiv \frac{\langle I(t+\tau)I(t) \rangle}{\langle I(t) \rangle^2}, \quad (2.8)$$

where $\langle \dots \rangle$ indicates average over measurement time t . For a Gaussian light source, such as the sample we consider, $G_2(\tau)$ is related to $g_1(\tau)$ via Siegert relation, i.e.

$$G_2(\tau) = 1 + \beta |g_1(\tau)|^2, \quad (2.9)$$

where β is a constant determined primarily by the collection optics of the experiment.

2.2.2 Multiple Scattering

To discuss the multiple scattering phenomenon, we must have knowledge about the mean free path of the medium which is given by[22]

$$l = \frac{1}{\rho\sigma}, \quad (2.10)$$

where ρ is the number density of scatters and σ is the total scattering cross-section for a single scatterer in the medium. If the scattering is isotropic, we may model the multiple scattering process as a random walk process with a random walk step size l . When the step number is large, the random walk problem can be treated with the diffusion equation. It can be proved that l is related to the photon diffusion coefficient D_γ , i.e.

$$D_\gamma = \frac{vl}{3}, \quad (2.11)$$

where v is the speed of light in the medium[23]. In the case of anisotropic scattering medium, l should be replaced with the transport mean free path l^* and the photon diffusion coefficient becomes

$$D_\gamma = \frac{vl^*}{3}. \quad (2.12)$$

The transport mean free path represents the length scale over which the photon direction is randomized as it traverses the medium. It is related to l by the following equation

$$l^* = \frac{l}{\langle 1 - \cos \theta \rangle}, \quad (2.13)$$

where θ is the scattering angle for a single scattering event in the sequence and $\langle \dots \rangle$ indicates an ensemble average over all the scattering events of the sequence. Eqn.

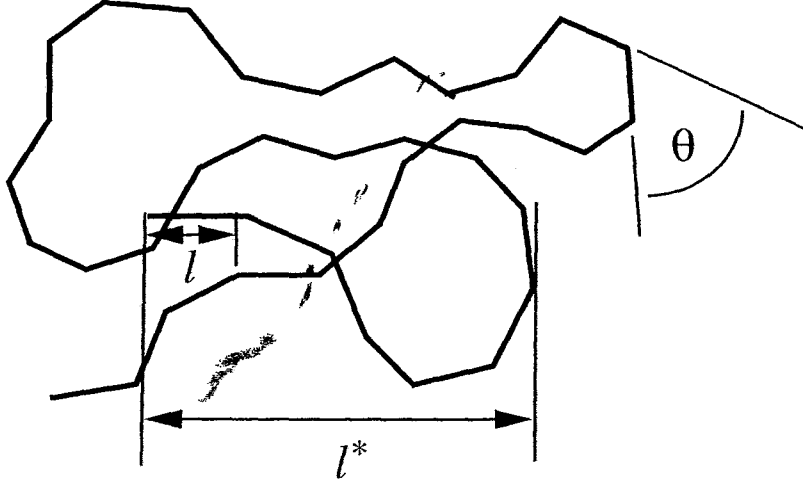


Figure 2.3: Persistence length in polymer: Each monomer of length l has a bond which makes an angle θ with its neighbor. l^* represents the the length scale over which the polymer bends significantly.

2.13 is a result of making diffusion approximation from electro-magnetic transport theory in random media[22]. We can motivate eqn 2.13 by analogy to polymers. In a polymer molecule, each monomer of length l has a bond which makes an angle θ with its neighbor. The persistence length l_p is similar in this case to the photon transport mean free path l^* and is given by the sum

$$l_p = l \sum_{n=0}^{\infty} \langle \cos \theta \rangle^n = \frac{l}{1 - \langle \cos \theta \rangle}. \quad (2.14)$$

Referring to Fig. 2.3 the persistence length relates the length scale over which the polymer bends significantly(i.e. by $\sim \pi$).

Now, we will derive the expression for the electric field temporal autocorrelation function $g_1(\tau)$ in the multiple scattering limit. Let's first consider the simple scattering process illustrated in Fig. 2.4. The light field passing along a particular path through the sample experiences N scattering events and emerges with a phase that depends on its total pathlength s which can be expressed as

$$s = \sum_{i=0}^N |\mathbf{r}_{i+1} - \mathbf{r}_i| = \sum_{i=0}^N \frac{\mathbf{k}_i}{|\mathbf{k}_i|} \cdot (\mathbf{r}_{i+1} - \mathbf{r}_i), \quad (2.15)$$

where \mathbf{k}_i is the wavevector of the photon after i scattering events, \mathbf{r}_i is the position

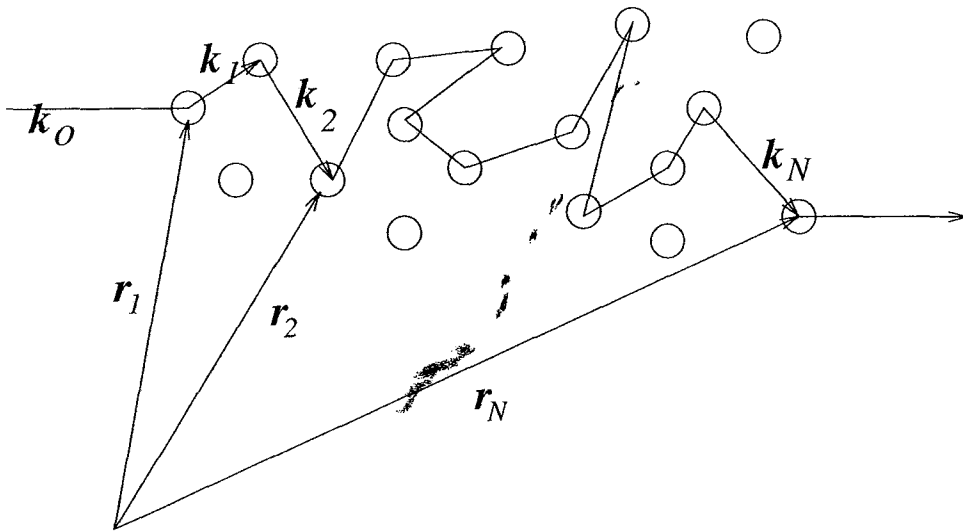


Figure 2.4: A photon experiences N scattering events: \mathbf{k}_i is the wavevector for the photon propagating from particle (i) at position \mathbf{r}_i to particle ($i+1$) at position \mathbf{r}_{i+1} .

of the i -th scatterer. The total phase of the field emerging from the sample at time t is

$$\phi(t) = k_0 s(t) = \sum_{i=0}^N \mathbf{k}_i(t) \cdot [\mathbf{r}_{i+1}(t) - \mathbf{r}_i(t)] \quad (2.16)$$

Here we have ignored the phase-shifts that accompany each scattering event since they will be constant at different time. The photons that arrive at the detector generally traverse different paths. The detected electric field is the superposition of the these fields. We write

$$E(t) = \sum_p E_p e^{i\phi_p(t)}, \quad (2.17)$$

where \sum_p represents a sum over all the paths p and E_p is the amplitude of the detected field from path p . We can insert this expression into the definition of the field autocorrelation function and obtain

$$g^{(i)}(\tau) = \left(\frac{\langle E(t) E^*(t+\tau) \rangle}{\langle |E(t)|^2 \rangle} \right) = \frac{1}{\langle I \rangle} \left\langle \left(\sum_p E_p e^{i\phi_p(t)} \right) \left(\sum_{p'} E_{p'}^* e^{i\phi_{p'}(t+\tau)} \right) \right\rangle, \quad (2.18)$$

where $\langle I \rangle$ is the total averaged scattering intensity. When the correlations between different paths can be neglected, we can drop those terms with $p \neq p'$ because their

average is zero, and we obtain

$$\begin{aligned} g_1(\tau) &= \left\langle \sum_p \frac{|E_p|^2}{\langle I \rangle} e^{i[\phi_p(t+\tau) - \phi_p(t)]} \right\rangle \\ &= \sum_p \frac{\langle I_p \rangle}{\langle I \rangle} \langle e^{i[\phi_p(t+\tau) - \phi_p(t)]} \rangle, \end{aligned} \quad (2.19)$$

where $\langle I_p \rangle$ is the average intensity from path p . Since only the correlation time τ is relevant to the measurement, we will set $t = 0$. From eqn. (2.16), we can obtain

$$\begin{aligned} \Delta\phi_p(\tau) &= \phi_p(\tau) - \phi_p(0) \\ &= \sum_{i=0}^N \mathbf{k}_i(\tau) \cdot [\mathbf{r}_{i+1}(\tau) - \mathbf{r}_i(\tau)] - \mathbf{k}_i(0) \cdot [\mathbf{r}_{i+1}(0) - \mathbf{r}_i(0)] \\ &= \sum_{i=0}^N (\mathbf{k}_{i+1}(0) - \mathbf{k}_i(0)) \cdot \Delta\mathbf{r}_i(\tau) + \sum_{i=0}^N (\mathbf{k}_i(\tau) - \mathbf{k}_i(0)) \cdot [\mathbf{r}_{i+1}(\tau) - \mathbf{r}_i(\tau)]. \end{aligned} \quad (2.20)$$

With the notations $\mathbf{q}_i \equiv \mathbf{k}_{i+1}(0) - \mathbf{k}_i(0)$ and $\Delta\mathbf{k}_i(\tau) \equiv \mathbf{k}_i(\tau) - \mathbf{k}_i(0)$, we further obtain

$$\Delta\phi_p(\tau) = \sum_{i=0}^N \mathbf{q}_i \cdot \Delta\mathbf{r}_i(\tau) + \sum_{i=0}^N \Delta\mathbf{k}_i(\tau) \cdot [\mathbf{r}_{i+1}(\tau) - \mathbf{r}_i(\tau)], \quad (2.21)$$

where $\Delta\mathbf{r}_i(\tau) \equiv \mathbf{r}_i(\tau) - \mathbf{r}_i(0)$. The magnitude of the wavevector is a constant in isotropic media, i.e.

$$d(k^2) = d(\mathbf{k} \cdot \mathbf{k}) = \mathbf{k} \cdot d\mathbf{k} = 0, \quad (2.22)$$

which indicates that $d\mathbf{k}$ is normal to \mathbf{k} . Recalling that \mathbf{k}_i is in the direction of $\mathbf{r}_{i,i+1} \equiv \mathbf{r}_{i+1} - \mathbf{r}_i$, $\Delta\mathbf{k}_i$ is almost normal to $\mathbf{r}_{i,i+1}$. Hence the second term in the above equation can be dropped also. We then have

$$\Delta\phi_p(\tau) = \sum_{i=0}^N \mathbf{q}_i \cdot \Delta\mathbf{r}_i(\tau), \quad (2.23)$$

where the amplitude of \mathbf{q}_i is related to the i -th scattering angle θ_i by

$$q_i = 2k_o \sin \frac{\theta_i}{2}. \quad (2.24)$$

Now we must calculate the quantity $\langle e^{-i\Delta\phi_p(\tau)} \rangle$. For large numbers of scattering events, $\Delta\phi_p$ is a random Gaussian variable. Utilizing the central limit theorem again, we obtain

$$\langle e^{-i\Delta\phi_p(\tau)} \rangle = e^{-\langle \Delta\phi_p^2(\tau) \rangle / 2}. \quad (2.25)$$

Using the expression for $\Delta\phi_p(\tau)$ in eqn. (2.21) and assuming the independence of successive phase factors $\mathbf{q}_i \cdot \Delta\mathbf{r}_i(\tau)$, we have

$$\begin{aligned}\langle \Delta\phi_p^2(\tau) \rangle &= \sum_{i=1}^N \sum_{j=1}^N \langle [\mathbf{q}_i \cdot \Delta\mathbf{r}_i(\tau)] [\mathbf{q}_j \cdot \Delta\mathbf{r}_j(\tau)] \rangle \\ &= \sum_{i=1}^N \langle [\mathbf{q}_i \cdot \Delta\mathbf{r}_i(\tau)]^2 \rangle.\end{aligned}\quad (2.26)$$

Furthermore, if each scattering event is independent, we have

$$\langle \Delta\phi_p^2(\tau) \rangle = N \langle [\mathbf{q}_i \cdot \Delta\mathbf{r}_i(\tau)]^2 \rangle = \frac{1}{3} N \langle q^2 \rangle \langle \Delta r^2(\tau) \rangle. \quad (2.27)$$

The quantity $\langle q^2 \rangle$ is given by

$$\langle q^2 \rangle \equiv \frac{\int F(q) q^2 d\mathbf{q}}{\int F(q) d\mathbf{q}}, \quad (2.28)$$

where $F(q)$ is the form factor for the single scattering. $\langle q^2 \rangle$ has a simple yet important relation to l^* as given in the the following expression

$$\langle q^2 \rangle = \langle [2k_o \sin(\theta/2)]^2 \rangle = 2k_o^2 \langle 1 - \cos\theta \rangle = 2k_o^2 \frac{l}{l^*}. \quad (2.29)$$

When the number of scattering events N is much larger than 1, the path length is $s = Nl$. Inserting eqn. (2.29) into eqn. (2.27), we obtain

$$\langle \Delta\phi_p^2(\tau) \rangle = \frac{2}{3} k_o^2 \frac{s}{l} \frac{l}{l^*} \langle \Delta r^2(\tau) \rangle = \frac{2}{3} k_o^2 \langle \Delta r^2(\tau) \rangle \frac{s}{l^*}. \quad (2.30)$$

We see that, for each path, only the path length s is relevant to the phase change. Therefore, we may classify all the paths by their pathlength s , and using pathlength distribution function $P(s)$, the summation $\sum_p \frac{\langle I_p \rangle}{I}$ is then replaced by $\sum_s P(s)$. When we sum over the contributions from different paths, we obtain the total electric-field autocorrelation function

$$g_1(\tau) = \sum_s P(s) \exp\left(\frac{1}{3} k_o^2 \langle \Delta r^2(\tau) \rangle \frac{s}{l^*}\right). \quad (2.31)$$

In the continuum limit, the summation is replaced by the integration so that

$$g_1(\tau) = \int_0^\infty P(s) \exp\left(\frac{1}{3} k_o^2 \langle \Delta r^2(\tau) \rangle \frac{s}{l^*}\right) ds. \quad (2.32)$$

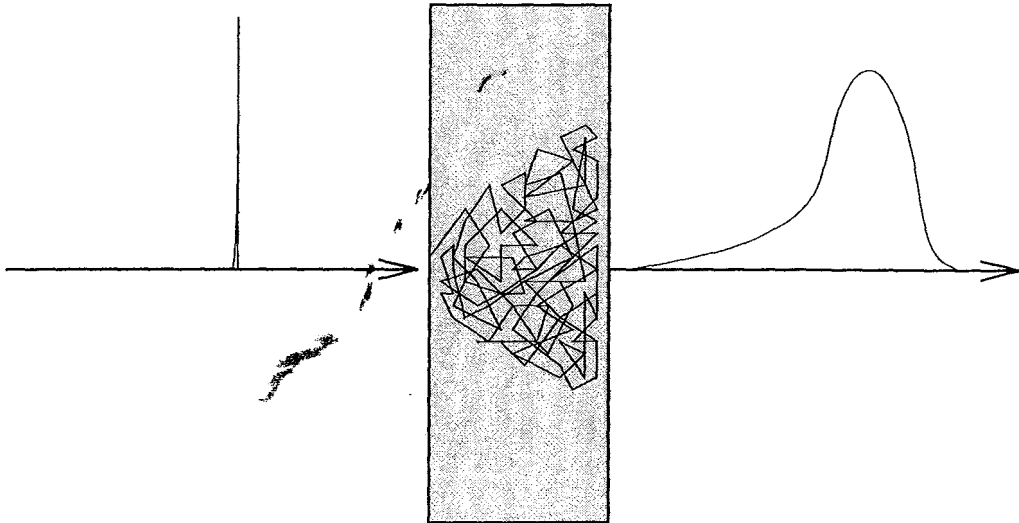


Figure 2.5: A very short laser pulse is incident from the left-hand side of the sample. The photons are scattered many times before they exit the sample. The output pulse is broadened in time as a result of the fact that photons arrive at different times. The shape of this pulse defines $P(t)$, the probability that a photon takes a time t to emerge from sample.

Eqn. (2.31) represents an *incoherent* sum over optical pathlengths[24, 25]. The decay of the electric field temporal autocorrelation function from each path is independent of all other paths. In fact, this is not always true, but in most cases of practical interest, the correlations between different paths can be neglected.

Eqn. (2.32) is one of the most important equations in DWS. However, $P(s)$, is often not directly measured. With the understanding of the fact that the travel length s is equal to the product of the speed of light in the medium v and the travel time t (i.e. $s = vt$), we may replace $P(s)$ by the travel time distribution function $P(t)$ which can be directly measured. In *isotropic* medium, to obtain $P(s)$ from $P(t)$ is simply a matter of scaling. The scaling of $s \rightarrow t$ is not trivial, however, in *anisotropic* medium, such as nematic liquid crystal. We will return to this point in Chapter 4. In this chapter, we discuss colloids which are isotropic and therefore eqn. (2.32) is still valid for our discussion.

To obtain the information about the dynamics of the studied system ($\langle \Delta r^2(t) \rangle$), we must determine $P(s)$. This is where the photon diffusion equation comes in. Let's

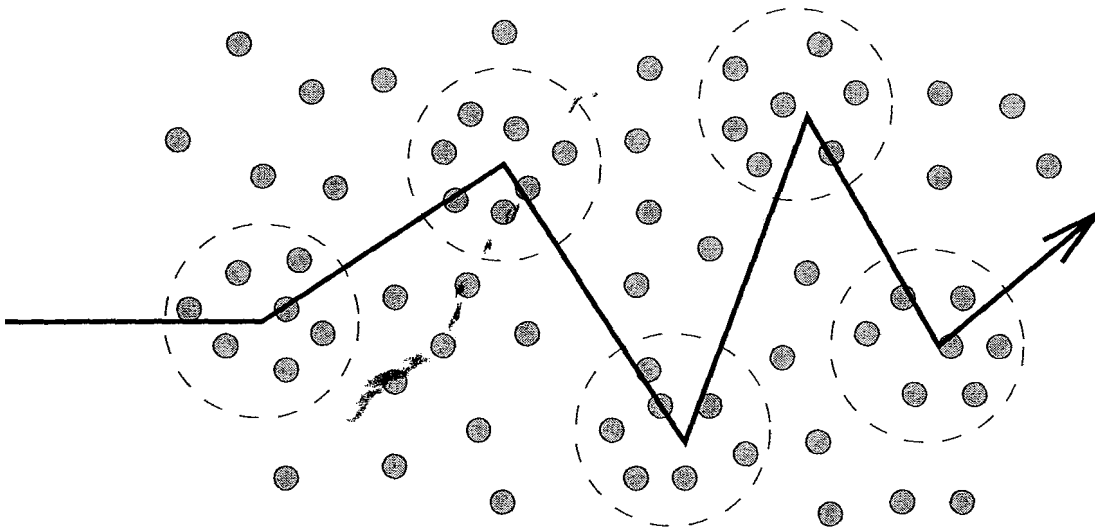


Figure 2.6: Multiple Scattering in a correlated system: The scattering is not determined solely by the scatterers themselves.

consider a simple thought experiment as shown in Fig. 2.5. Assuming a very short pulse of light is incident over some area of the sample. Photons in this pulse are scattered and execute random walks until they escape. As we collect the escaping photons at certain position outside the sample, we will find that these photons arrive at different time. Statistically, the probability distribution function for the arrival times of photon is $P(t)$ mentioned in previous paragraph. Since we can use the diffusion equation to solve the random walk problem, we can obtain $P(t)$ by solving the photon diffusion equation for an instantaneous pulse with appropriate boundary conditions. The typical boundary conditions used in practice assume the photon energy density drops to zero at certain extrapolation positions outside the sample. We will return to this point in Chapter 3.

As the inter-particle distance becomes smaller, interference effect due to nearby particles is an important factor in determining the differential cross-section and l^* . In this case, as shown in Fig. 2.6, the scattering is not determined solely by the scatterer itself. We have to add in the effects of the local structure factor $S(q)$ of

the system which is given by

$$S(\mathbf{q}) = \sum_{i=1}^N e^{i\mathbf{q}\cdot\mathbf{r}_i}. \quad (2.33)$$

This analysis has been done previously[37], and will not be reproduced here. The picture of a sequence of scattering events is still valid, but the quantity $\langle q^2 \rangle$ is modified and is given by

$$\langle q^2 \rangle = \frac{\int F(\mathbf{q})S(\mathbf{q})q^2 d\mathbf{q}}{\int F(\mathbf{q})S(\mathbf{q}) d\mathbf{q}}, \quad (2.34)$$

where $F(q)$ is the form factor for the single scattering and $S(q)$ is the structure factor of the sample. In general, the other physical quantities measured in DWS, such as the particle diffusion constant, are also modified[37]. These effective quantities are obtained from the averaging procedures outlined later, and in reference[37].

2.3 Brownian Motion in Hydrodynamic Time Scales

As far back as 1828, Robert Brown found that the dispersed pollen of plants in water have some kind of irregular “swarming” motion. Later, he also found this phenomenon exists generally in all kinds of organic substances. The origin of Brownian motion remained a mystery until Einstein pointed out that Brownian motion was a natural consequence of the thermal motion of the solvent molecules. In his series of papers, Einstein provided a sound theoretical analysis of the Brownian motion as “random walk problem”. He established the relationship between the irreversible nature of the Brownian motion and the mechanism of molecular fluctuations. To sketch out the fundamental theme of Einstein’s approach, let’s consider a simple one-dimensional random walk problem. Assuming the Brownian particle can only move in the x -axis with step size l . In every movement, the Brownian particle has the same probability in moving forward or backward. We want to know what is the probability that after n steps, we find that the Brownian particle has moved m steps more in the $+x$ direction than in the $-x$ direction. This probability is given

by the binomial expression

$$p_n(m) = \frac{1}{2^n} \frac{n!}{\left\{\frac{1}{2}(n+m)\right\}! \left\{\frac{1}{2}(n-m)\right\}!} \quad (2.35)$$

This probability distribution function yields the following relations

$$\overline{m} = 0, \quad (2.36)$$

$$\overline{m^2} = n. \quad (2.37)$$

If we use $x(t)$ to denote the position of the Brownian particle at time t , and τ^* to denote the average time between movements, we have

$$\overline{x(t)} = 0, \quad (2.38)$$

$$\overline{x^2(t)} = l^2 \frac{t}{\tau^*} \propto t \quad (2.39)$$

when $t \gg \tau^*$.

Besides Einstein's approach, Smoluchowski took another approach to the problem of Brownian motion. Smoluchowski introduced the probability function $p_n(x_o|x)$ which denotes the "probability that the Brownian particle moves from point x_o to point x in n steps". It is given by the so called *Smoluchowski equation*

$$p_n(x_o|x) = \sum_{z=-\infty}^{\infty} p_{n-1}(x_o|z)p_1(z|x) \quad (n \geq 1)$$

$$p_1(z|x) = \frac{1}{2}\delta_{z,x-1} + \frac{1}{2}\delta_{z,x+1} \quad (2.40)$$

$$p_o(z|x) = \delta_{z,x}. \quad (2.41)$$

Its solution is

$$\begin{aligned} p_n(x_o|x) &= \frac{1}{2^n} \frac{n!}{\left\{\frac{1}{2}(n+x-x_o)\right\}! \left\{\frac{1}{2}(n-x+x_o)\right\}!} \quad \text{for } |x-x_o| \leq n \\ &= 0 \quad \text{for } |x-x_o| > n. \end{aligned} \quad (2.42)$$

This result completely agrees with the result obtained via Einstein's approach. Using Stirling's formula, $n! \simeq (2\pi n)^{1/2}(n/e)^n$ and assuming $m \ll n$, we arrive at

$$p_n(m) \simeq \frac{2}{\sqrt{2\pi n}} \exp(-m^2/2n). \quad (2.43)$$

Now, let's take the position x as a continuous variable, then we can transform the above equation into the *Gaussian form*:

$$p(x)dx = \frac{dx}{\sqrt{4\pi Dt}} \exp\left(-\frac{x^2}{4Dt}\right), \quad (2.44)$$

where

$$D = \frac{1}{2} \frac{l^2}{\tau^*}. \quad (2.45)$$

If we consider the diffusion equation for an N -particle system in one-dimension, i.e.

$$D \frac{\partial^2}{\partial x^2} n(x, t) - \frac{\partial n(x, t)}{\partial t} = 0, \quad (2.46)$$

where $n(x, t)$ represents the particle number density and D is the particle diffusion constant, then the solution is

$$n(x, t) = \frac{N}{\sqrt{4\pi Dt}} \exp\left(-\frac{x^2}{4Dt}\right). \quad (2.47)$$

Comparing eqn.(2.47) with eqn.(2.44), we find the deep relationship between the random walk problem and the diffusion equation.

The ultimate source of the Brownian motion is the incessant, random impacts from the molecules of the fluid. Let's consider the simplest case of an isolated Brownian particle with mass M suspended in a fluid. The equation of motion of this particle is given by

$$M \frac{d\mathbf{v}}{dt} = \mathcal{F}(t). \quad (2.48)$$

Here, $\mathcal{F}(t)$ represents all forces exerted on the particle. Langevin suggested that $\mathcal{F}(t)$ may be composed of two parts : (i) an "averaged-out" force, which represents the viscous drag experienced by the particle and (ii) a "fast fluctuating" force $\mathbf{F}(t)$ which averages out to zero over long intervals of time. We then can rewrite the equation of motion in the following form

$$\frac{d\mathbf{v}}{dt} = -\frac{\mathbf{v}}{MB} + \frac{1}{M} \mathbf{F}(t), \quad (2.49)$$

where B is called the particle mobility and $\overline{\mathbf{F}(t)} = 0$. As we carry out the ensemble average, we obtain

$$\frac{d}{dt} \langle \mathbf{v} \rangle = -\frac{1}{MB} \langle \mathbf{v} \rangle. \quad (2.50)$$

The solution of this equation is obvious:

$$\langle \mathbf{v}(t) \rangle = \langle \mathbf{v}(0) \rangle \exp(-t/MB) \quad (2.51)$$

The solution implies the drift velocity of the particle decays with a relaxation time $\tau = MB$. An alternate formulation of eqn. 2.48 is given in terms of the particle mean-square displacements and velocities, i.e.

$$\frac{d^2}{dt^2} \langle r^2 \rangle + \frac{1}{\tau} \frac{d}{dt} \langle r^2 \rangle = 2 \langle v^2 \rangle, \quad (2.52)$$

where $\mathbf{r}(t=0) = (0, 0, 0)$. In thermal equilibrium, $\langle v^2 \rangle$ can be replaced by its equipartition value $3k_B T/M$ and the solution of $\langle r^2 \rangle$ then is given by

$$\langle r^2 \rangle = \frac{6k_B T \tau^2}{M} \left\{ \frac{t}{\tau} - (1 - e^{-t/\tau}) \right\}. \quad (2.53)$$

Note that $\langle r^2 \rangle \equiv \langle \Delta r^2 \rangle$ since $\langle \mathbf{r} \rangle = 0$. Let's look at two limiting cases of the solution.

When $t \ll \tau$, we have

$$\langle \Delta r^2 \rangle \simeq \frac{3k_B T}{M} t^2 = \langle v^2 \rangle t^2. \quad (2.54)$$

This result indicates that in the very early stage of Brownian motion, the particle moves ballistically. On the other hand, when $t \gg \tau$, we have

$$\langle \Delta r^2 \rangle \simeq \frac{6k_B T \tau}{M} t = 6(Bk_B T)t. \quad (2.55)$$

This result is essentially the same as the Einstein-Smoluchowski result and establishes a simple relation between the diffusion coefficient D and the mobility B . To further understand the influence caused by the fluctuating $\mathcal{F}(t)$, let us try to evaluate the quantity $\langle v^2(t) \rangle$. If we replace the variable t in eqn. 2.49 by u , multiply both sides of the equation by $\exp(u/\tau)$, rearrange and integrate over u from $u = 0$ to $u = t$, we will obtain

$$v(t) = v(0)e^{-t/\tau} + \frac{1}{M} e^{-t/\tau} \int_0^t e^{u/\tau} \mathcal{F}(u) du. \quad (2.56)$$

and

$$\begin{aligned} \langle v^2(t) \rangle &= v^2(0)e^{-2t/\tau} + \frac{2}{M}e^{-2t/\tau} \left[\mathbf{v}(0) \cdot \int_0^t e^{u/\tau} \langle \mathcal{F}(u) \rangle du \right] \\ &+ \frac{1}{M^2}e^{-2t/\tau} \int_0^t \int_0^t e^{(u_1+u_2)/\tau} \langle \mathcal{F}(u_1) \cdot \mathcal{F}(u_2) \rangle du_1 du_2. \end{aligned} \quad (2.57)$$

The second term should vanish because $\langle \mathcal{F}(u) \rangle = 0$. The third term is a measure of the correlation of fluctuations. It is a quantity of essential importance. As the correlation time of the fluctuating force is very short, with equipartition theorem, one can prove that

$$\langle v^2(t) \rangle = \langle v^2(0) \rangle \quad (2.58)$$

This equation looks trivial, but it indicates the important fact that statistical equilibrium, once attained, has a natural tendency to persist!

From eqn. 2.56, we can calculate the velocity correlation function $R(t)$, i.e.

$$R(t) \equiv \langle \mathbf{v}(t) \cdot \mathbf{v}(0) \rangle = R(0)e^{-t/\tau} + \frac{1}{3} \int_0^t dt' e^{-(t-t')/\tau} \langle \mathcal{F}(t') \cdot \mathbf{v}(0) \rangle. \quad (2.59)$$

Because of causality, the particle's velocity at $t = 0$ cannot be influenced by the random forces occurring at $t > 0$, and the term $\langle \mathcal{F}(t') \cdot \mathbf{v}(0) \rangle$ should vanish. Therefore, we obtain the velocity correlation function in an exponential form, i.e.

$$R(t) = \frac{k_B T}{M} e^{-t/\tau}. \quad (2.60)$$

In some numerical simulations of the molecular motions in liquids done by Rahman (1964)[3], Alder & Wainwright (1967)[4], they found a long-tailed decay in the velocity correlation function. Simple Langevin theory cannot predict this. This indicates a deficiency in the simple Langevin approach. Physically, the simple Langevin equation does not consider the hydrodynamic interactions coupled to the particle except for viscous drag. Alder & Wainwright (1970) numerically solved the Navier-Stokes equations for time-dependent flow outside a rigid sphere and were able to predict a $t^{-3/2}$ asymptotic decay in the velocity correlation function of the sphere[4]. Zwanzig & Bixon (1970) recalculated the velocity correlation function using the explicit generalization of the Stokes drag for transient motions with an arbitrary frequency and

repeated the $t^{-3/2}$ asymptotic decay[5]. Though the frequency-dependent friction corrected the velocity correlations, it also led to some difficulties with the Stoke-Einstein relation

$$D \neq k_B T / \xi, \quad (2.61)$$

where ξ is the inverse of the particle's mobility B .

Hinch proposed a correction to Langevin equation by applying the Langevin equation to the fluid as well as the particles[6]. This approach retains the simplicity of Langevin's approach while yielding the correct decay of the velocity correlation function. In the following discussion, we will give a brief review of Hinch's theory.

Let's start with a general system whose instantaneous configuration is described by the state vector \mathbf{x} . For a N -particle system, \mathbf{x} is a vector containing all the individual particle position vectors, i. e. $\mathbf{x} \equiv (\mathbf{x}_1, \mathbf{x}_2, \mathbf{x}_3, \dots, \mathbf{x}_N)$. The rate of change of the system then is denoted by $\dot{\mathbf{x}}$ and the scalar inner product of two state vectors is denoted by $\mathbf{x}_1 \cdot \mathbf{x}_2$. In fluid, \mathbf{x} belongs to an infinite-dimensional space which is a mathematical idealization of replacing the enormous number of small solvent molecules by a continuum. The state vector \mathbf{x} for a suspension system will be discussed later. We also use a second-rank tensor field $\mathbf{m}(\mathbf{x})$ to denote a generalized inertia of the system. Thus the kinetic energy of the changing system is given as $\frac{1}{2} \dot{\mathbf{x}} \cdot \mathbf{m} \cdot \dot{\mathbf{x}}$ while its generalized momentum is given as $\mathbf{m} \cdot \dot{\mathbf{x}}$. Furthermore, we assume the system is subject to a friction which is linear to the instantaneous velocity and is represented by a term $\boldsymbol{\xi} \cdot \dot{\mathbf{x}}$. The second-rank tensor field $\boldsymbol{\xi}$ as well as \mathbf{m} is symmetric. The Langevin equation to be studied becomes

$$\mathbf{m} \cdot \ddot{\mathbf{x}} + \boldsymbol{\xi} \cdot \dot{\mathbf{x}} = \mathcal{F}(t) \quad (2.62)$$

with the initial conditions

$$\mathbf{x}(0) = \dot{\mathbf{x}}(0) = 0. \quad (2.63)$$

The random force \mathcal{F} is considered as stationary white noise. A white-noise force has two characteristics: the force has no correlation with its value at different times

and the magnitude of the fluctuations does not change in time. Mathematically, it is expressed as

$$\langle \mathcal{F}(t)\mathcal{F}(t') \rangle = \delta(t' - t)\mathbf{F}, \quad (2.64)$$

where \mathbf{F} is a constant symmetric second-rank correlation tensor. In reality, the random force does have a very short but non-zero correlation time. Therefore, we restrict our attention to much longer macroscopic events which sense only the integral force correlation

$$\mathbf{F} = \int_{-\infty}^{\infty} \langle \mathcal{F}(t)\mathcal{F}(t + \tau) \rangle d\tau \quad (2.65)$$

Another assumption we have to make is that the system has a well-defined temperature. In another words, thermal equilibrium is reached and equipartition of energy is applicable to the system. If we can diagonalize the inertia tensor \mathbf{m} , by the above assumption, each possible mode of change of state is associated with a mean kinetic energy of $\frac{1}{2}k_B T$. It can be expressed in the following equation:

$$\lim_{t \rightarrow \infty} \langle \dot{\mathbf{x}}\dot{\mathbf{x}} \rangle = k_B T \mathbf{m}^{-1} \quad (2.66)$$

The solution of eqn.(2.62) with the initial conditions is given by

$$\dot{\mathbf{x}}(t) = \int_0^t dt' \exp[\mathbf{m}^{-1} \cdot \boldsymbol{\xi}(t' - t)] \cdot \mathbf{m}^{-1} \cdot \mathcal{F}(t') \quad (2.67)$$

Then the velocity correlation function then becomes

$$\langle \dot{\mathbf{x}}(t)\dot{\mathbf{x}}(t) \rangle = \int_0^t dt' \int_0^t dt'' \exp[\mathbf{m}^{-1} \cdot \boldsymbol{\xi}(t' - t)] \cdot \mathbf{m}^{-1} \cdot \langle \mathcal{F}(t)\mathcal{F}(t'') \rangle \cdot \mathbf{m}^{-1} \cdot \exp[\mathbf{m}^{-1} \cdot \boldsymbol{\xi}(t'' - t)] \quad (2.68)$$

Applying the white noise assumption, we obtain

$$\langle \dot{\mathbf{x}}(t)\dot{\mathbf{x}}(t) \rangle = \int_0^t dt' \exp[\mathbf{m}^{-1} \cdot \boldsymbol{\xi}(t' - t)] \cdot \mathbf{m}^{-1} \cdot \mathbf{F} \cdot \mathbf{m}^{-1} \cdot \exp[\mathbf{m}^{-1} \cdot \boldsymbol{\xi}(t' - t)] \quad (2.69)$$

Integrating by parts, we further obtain

$$\langle \dot{\mathbf{x}}(t)\dot{\mathbf{x}}(t) \rangle = \boldsymbol{\xi}^{-1} \cdot \mathbf{F} \cdot \mathbf{m}^{-1} - \exp[-\mathbf{m}^{-1} \cdot \boldsymbol{\xi}t] \cdot \boldsymbol{\xi}^{-1} \cdot \mathbf{F} \cdot \mathbf{m}^{-1} \cdot \exp[-\mathbf{m}^{-1} \cdot \boldsymbol{\xi}t] - \boldsymbol{\xi}^{-1} \cdot \mathbf{m} \cdot \langle \dot{\mathbf{x}}\dot{\mathbf{x}} \rangle \cdot \boldsymbol{\xi} \cdot \mathbf{m}^{-1} \quad (2.70)$$

Finally, the assumption of equipartition of energy yields

$$\mathbf{F} = 2k_B T \boldsymbol{\xi} \quad (2.71)$$

This result illustrates one important physical issue: fluctuation-dissipation theorem which relates the magnitudes of the random fluctuating force to the mean friction force. Now let's look at the velocity correlation function which is defined as

$$\mathbf{R}(\tau) = \lim_{t \rightarrow \infty} \langle \dot{\mathbf{x}}(t + \tau) \dot{\mathbf{x}}(t) \rangle. \quad (2.72)$$

Using the solution of the Langevin equation obtained above and white-noise assumption, we have

$$\mathbf{R}(\tau) = \exp[-\mathbf{m}^{-1} \cdot \boldsymbol{\xi} \cdot \tau] \cdot \mathbf{R}(0) = k_B T \mathbf{m}^{-1} \exp[-\mathbf{m}^{-1} \cdot \boldsymbol{\xi} \tau], \quad \tau \geq 0 \quad (2.73)$$

and

$$\mathbf{R}(\tau) = \mathbf{R}^T(-\tau) = k_B T \mathbf{m}^{-1} \exp[\boldsymbol{\xi} \cdot \mathbf{m}^{-1} \tau], \quad \tau \leq 0 \quad (2.74)$$

where the superscript T denotes the transpose of the tensor.

The diffusivity for the considered system is defined as

$$\mathbf{D} = \lim_{t \rightarrow \infty} \frac{1}{2} \frac{d \langle \mathbf{x}(t) \mathbf{x}(t) \rangle}{dt} \quad (2.75)$$

After a few manipulations, we can express it in the form of

$$\mathbf{D} = \frac{1}{2} \int_0^\infty [\mathbf{R}(\tau) + \mathbf{R}^T(\tau)] d\tau \quad (2.76)$$

So far, our discussion is quite general regarding the studied system. Now, let's specify that the studied system is a suspension of N rigid particles in an incompressible Newtonian fluid. We first define a few quantities: \mathbf{x}_n is the position of n th particle; $\boldsymbol{\theta}_n$ is the orientation of n th particle. \mathbf{u}_n and $\boldsymbol{\omega}_n$ are the translation velocity and angular velocity of n th particle respectively; M_n is the mass and \mathbf{I}_n is the moment of inertia of n th particle respectively. The velocity field of the fluid has form of

$$\mathbf{u}(\mathbf{x}) = \mathbf{u}_n + \boldsymbol{\omega}_n \times (\mathbf{x} - \mathbf{x}_n) \quad (2.77)$$

on the n th particle's surface. For simplicity, we restrict our attention to the fluid with solenoidal velocity field, constant density ρ and viscosity μ . Furthermore, we also neglect the nonlinear fluid inertia term, changes in the moment inertia tensor as the particles rotate, and changes in the shape of the fluid volume as the particles move. Then, we can write down the momentum equations for the components of the suspension as

$$\left. \begin{aligned} \nabla \cdot \mathbf{u} &= 0 \\ \rho \frac{\partial \mathbf{u}}{\partial t} &= -\nabla p + \mu \nabla^2 \mathbf{u} \\ M_n \frac{d\mathbf{u}_n}{dt} &= \oint \mathbf{I}_n \mathbf{n} \cdot \boldsymbol{\sigma} \\ \mathbf{I}_n \cdot \frac{d\boldsymbol{\omega}_n}{dt} &= \oint (\mathbf{x} - \mathbf{x}_n) \times \mathbf{n} \cdot \boldsymbol{\sigma} \\ \boldsymbol{\sigma} &= -p\mathbf{I} + \mu(\nabla \mathbf{u} + \nabla \mathbf{u}^T) \end{aligned} \right\} \quad (2.78)$$

where the integrals are taken around the surface of the particle and \mathbf{n} is the outward normal. The state vector of the system now composes of three components: the first one is the continuum of points i in the fluid, the second one is the position, and the third one is the orientation of the particles. We may denote it as

$$\mathbf{x} = (\mathbf{x}, \mathbf{x}_n, \boldsymbol{\theta}_n) \quad (2.79)$$

The state velocity vector is given by

$$\dot{\mathbf{x}} = (\mathbf{u}(\mathbf{x}), \mathbf{u}_n, \boldsymbol{\omega}_n) \quad (2.80)$$

The generalized momentum is then given by

$$\mathbf{m} \cdot \dot{\mathbf{x}} = (\rho \partial \mathbf{u}(\mathbf{x}) / \partial t, M_n d\mathbf{u}_n / dt, \mathbf{I}_n \cdot d\boldsymbol{\omega}_n / dt). \quad (2.81)$$

To obtain measurable physical quantities, such as $R(\tau)$ or D , we need to obtain \mathbf{m} and ξ in matrix form. Comparing eqn. 2.78 and eqn. 2.81, one can obtain \mathbf{m} as given by

$$\mathbf{m} = \begin{pmatrix} \rho \mathbf{I} \delta(\mathbf{x}' - \mathbf{x}) & 0 & 0 \\ 0 & M_n \mathbf{I} \delta_{n' n} & 0 \\ 0 & 0 & \mathbf{I}_n \delta_{n' n} \end{pmatrix} \quad (2.82)$$

To obtain the symmetric friction tensor is pretty complicated, but it can be proved to be of the following form:

$$\xi = \begin{pmatrix} \mu\delta(\mathbf{x}' - \mathbf{x})(\mathbf{I}\vec{\nabla} \cdot \vec{\nabla} + \vec{\nabla}\vec{\nabla}) & 0 & 0 \\ 0 & 0 & 0 \\ 0 & 0 & 0 \end{pmatrix}. \quad (2.83)$$

Our goal now is to obtain the expression of the velocity correlation function. The furthermore calculation will be omitted and only the result is given, which is

$$R(\tau) = \frac{k_B T}{2\pi a^3 \rho (5 - 8\rho'/\rho)^{\frac{1}{2}}} \left[\alpha_+ e^{\alpha_+^2 \tau} \operatorname{erfc}(\alpha_+ \sqrt{\tau}) - \alpha_- e^{\alpha_-^2 \tau} \operatorname{erfc}(\alpha_- \sqrt{\tau}) \right] \quad (2.84)$$

$$, \text{ where } \alpha_{\pm} = \frac{3}{2} \left[3 \pm \left(5 - 8\frac{\rho'}{\rho} \right)^{\frac{1}{2}} \right] / \left(1 + 2\frac{\rho'}{\rho} \right),$$

ρ' and a are the density and radius of the sphere respectively. This expression of the velocity correlation function has the $\tau^{-3/2}$ asymptotic decay as predicted by numerical simulations, i.e.

$$R(\tau) \sim \frac{k_B T}{12\pi^{3/2} a^3 \rho} \left(\frac{\tau_\nu}{\tau} \right)^{3/2}, \quad \text{for } \tau \gg \tau_\nu. \quad (2.85)$$

Here $\tau_\nu \equiv \rho a^2 / \eta$ is called hydrodynamic time. We also have

$$\langle \Delta r^2(\tau) \rangle = 6D_0 \tau_\nu \left\{ \tau - 2\sqrt{\frac{\tau}{\pi}} + \frac{2}{9} \left(4 - \frac{\rho'}{\rho} \right) + \frac{3}{\sqrt{5 - 8(\rho'/\rho)}} \right. \\ \left. \times \left[\frac{1}{\alpha_+^3} e^{\alpha_+^2 \tau} \operatorname{erfc}(\alpha_+ \sqrt{\tau}) - \frac{1}{\alpha_-^3} e^{\alpha_-^2 \tau} \operatorname{erfc}(\alpha_- \sqrt{\tau}) \right] \right\}, \quad (2.86)$$

This expression of $\langle \Delta r^2(\tau) \rangle$ has the same diffusive behavior predicted by simple Langevin's theory in the long time limit. In the short time limit ($\tau < \tau_\nu$), however, it predicts a significantly smaller displacement. In the experiment we will discuss later in this chapter, we measured the root-mean-square displacement of polystyrene spheres suspended in water as a function of time. We found in very dilute sample, Hinch's theory agrees with our experiment results.

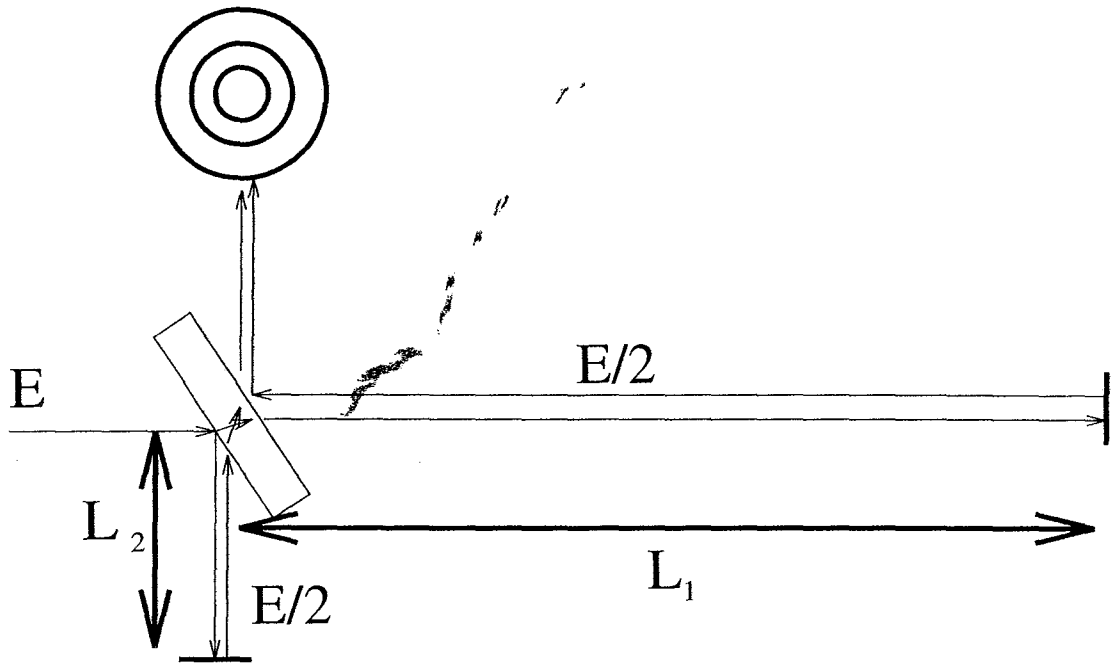


Figure 2.7: A simple Michelson Interferometer: The speckle field $E(t)$ is divided at the interferometer entrance, directed along two spatially separated paths of differing length, and then recombined.

2.4 Diffusing-Wave Interferometry(DWI)

Although DWS is a powerful technique in probing dynamics of suspension system, its time resolution is limited by the time resolution that the electronic autocorrelator can offer. Currently, the best time resolution that commercial electronic autocorrelator can offer is about 15 nsec. This resolution is not adequate to probe the Brownian dynamics on the earliest hydrodynamic time scales. To overcome this limitation, we replace the electronic autocorrelator in a traditional DWS set-up by an optical autocorrelator. In our experiment, we use a Michelson interferometer as the optical autocorrelator.

As shown in Fig. 2.7, the sample speckle field $E(t)$ is divided at the interferometer entrance, directed along two spatially separated paths of differing length, and then recombined on a light detector. In this case the time-averaged intensity we measure, $\langle I(\tau) \rangle$, depends on the temporal delay τ introduced between the recombined fields,

the optical carrier frequency ω , the average speckle intensity I_{ave} , and the temporal autocorrelation function $g_1(\tau) = |\langle E^*(t+\tau)E(t) \rangle| / \langle |E(t)|^2 \rangle$ of the sample speckle field, i.e.,

$$\langle I(\tau) \rangle = \frac{1}{2} I_{ave} [1 + g_1(\tau) \cos(\omega\tau)]. \quad (2.87)$$

This equation tells us that $\langle I(\tau) \rangle$ is an oscillatory function of τ with $g_1(\tau)$ as its envelope. In the optical frequencies, $\cos \omega\tau$ oscillates in the time scales of femto-second. If $g_1(\tau)$ decays in the time scales much longer than that, it is a good approximation to take $g_1(\tau)$ as a constant for several oscillation cycles. In this case, we have a simple formula to relate the field autocorrelation function to measured intensity:

$$g_1(\tau) = \frac{I(\tau)_{max} - I(\tau)_{min}}{I(\tau)_{max} + I(\tau)_{min}} \quad (2.88)$$

Thus the temporal visibility of the detected intensity directly yields $g_1(\tau)$. Typically, the hydrodynamic time scale of Brownian dynamics is nano-second and therefore we can use eqn. (2.88).

This optical correlator technique overcomes several limitations inherent in conventional photon correlation methodologies. The time resolution is at least 10 times better than the smallest commercially available correlator bin width, and can in principle be as short as a few femto-seconds; the minimum count rates can be lower than 1 kHz without degrading the signal-to-noise, and in contrast to DWS intensity correlation measurements [29], the information derived from the *electric field* correlation function is not affected when the laser coherence length becomes smaller than the typical photon path length through the medium.

2.5 Experiment Set-up

The goal of the first experiment we discuss in this dissertation is to probe the Brownian dynamics in the hydrodynamic time scales. Before we describe the experiment set-up, we will first describe the sample we studied and how we prepared it. The

studied sample in this experiment is the polystyrene sphere suspension. As described in Chapter 1, polystyrene spheres can be made very uniform in the size and thus we can treat them as monodisperse system. By adding HCl, we can also control the screening length to make them interact with each other like hard sphere. The density of the polystyrene sphere is only 1.05 g/cm³ and thus for most of the cases, we don't have to worry about the sedimentation during the measurement. In our experiment, we use different sphere sizes which range from 0.205 μm to 0.460 μm. For these sphere size, there is no observable sedimentation within several days. To calculate the transport mean free path l^* of the sample, we need to know its volume fraction. The procedure we used to measure the volume fraction is described in the following:

1. Measure the weight of a clean dried empty container W_b .
2. Pour the suspension into the container and measure the total weight W_t .
3. Dry the sample until all the water is gone.
4. Measure the weight of the dried sample W_p .
5. The volume fraction of the sample is then given by

$$\phi = \frac{(W_p - W_b)/d_{polystyrene}}{(W_p - W_b)/d_{polystyrene} + (W_t - W_p)/d_{water}}. \quad (2.89)$$

With a balance with accuracy up to 0.1mg, the above procedure provides a simple yet accurate measurement of volume fraction. With the know volume fraction and sphere size, we can calculate l^* . The actual calculation was carried out by a computer program.

In Fig. 2.8, we show the set-up of the experiment that we have carried out for probing the Brownian dynamics in the hydrodynamic time scales. The polystyrene sphere suspension is stored in a cylindrical cell. The diameter of the cell is 5 cm. To obtain desired decay in $g_1(\tau)$ for a particular sample, the thickness of the cell, depends on the volume fraction of the sphere, is selected from 1-cm, 2-cm, 3-cm, 4-cm, or 5-cm. The whole sample cell was immersed in the water. The purpose of this is two-fold. First, it reduces the reflection at the boundaries caused by

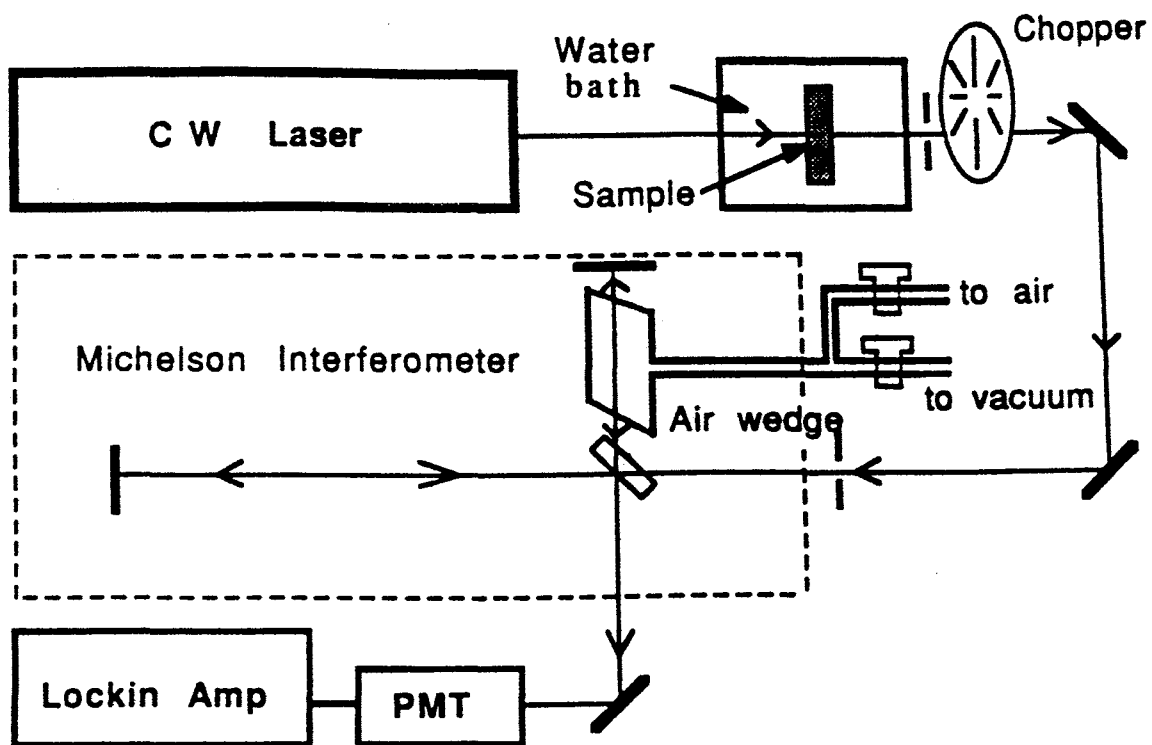


Figure 2.8: Experiment set-up for probing Brownian Motion in hydrodynamic time scales

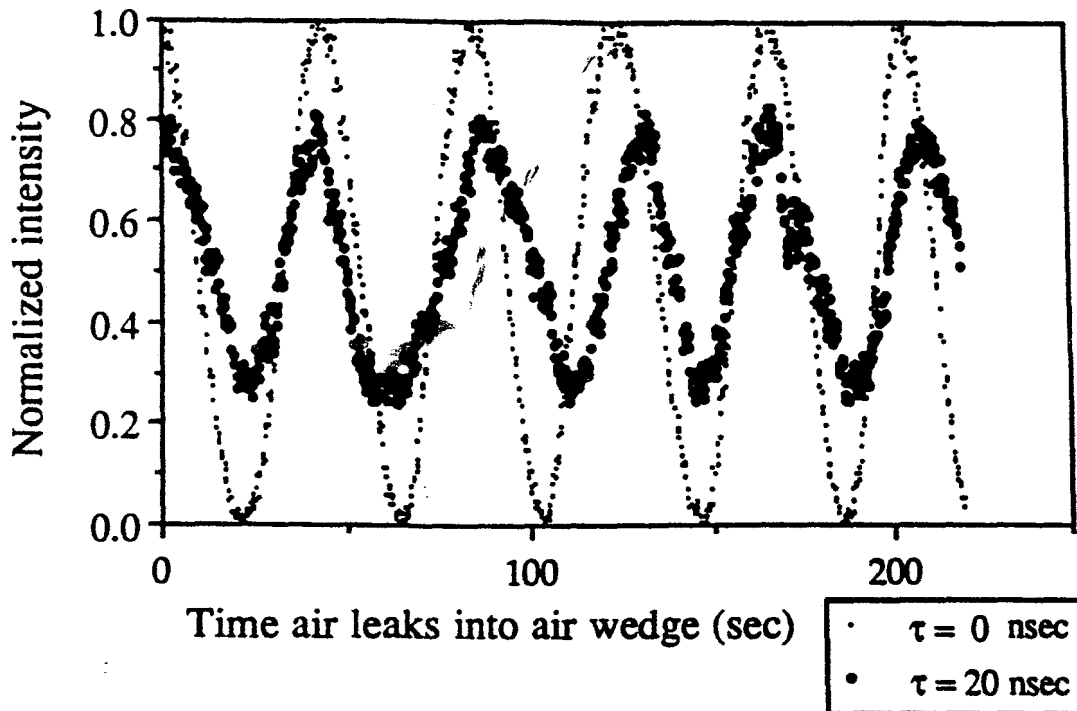


Figure 2.9: Examples of intensity scan as a function of time

the index mismatch. We have more detailed discuss about this point in the next chapter. Second, the water serves as heat bath to minimize the temperature change of the sample. This is important since the sample is illuminated by a laser beam with power up to 7W. In our experiment, we used the green light from an Ar^+ laser ($\lambda = 514.5nm$) to impinge on the center of the cylindrical cell. We used a pin-hole to select the photons emerged from the center of the other end surface. These photons were directed into a Michelson interferometer which offers up to 20-nsec optical delay. The photons were separated into two beams by a (50/50) beam splitter. These two beams recombined with the delay τ set by the length difference of the two arms of the Michelson interferometer. The recombined light then was sent into the PMT. The signal from the PMT was send to a computer controlled locking amplifier. In the fixed arm of the Michaelson interferometer, we inserted an air wedge in which the air density was controlled. The purpose of this air wedge is to change to optical

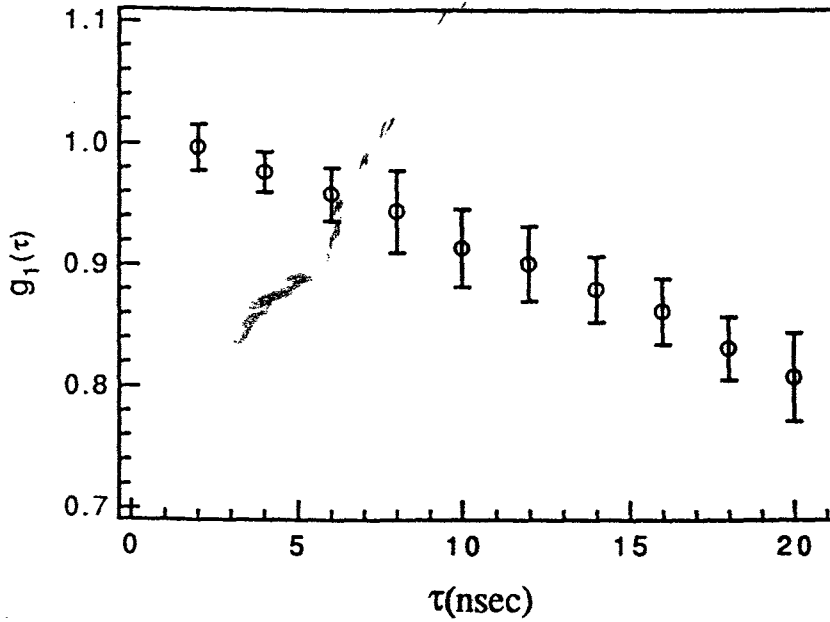


Figure 2.10: Measurement result of $g_I(\tau)$

delay in the time scale of femto-seconds. During the process of measurement, we first manually moved the mirror in the adjustable arm to the desired delay for the field autocorrelation function. Then we pumped out the air in the air wedge and let the air leak in again very slowly. Since the change in the air density changes the index of refraction and thus the travel time for the photon to pass through the air wedge, we were able to obtain an extra time delay in the time scale of femto-seconds. The intensity of collected photons was plotted as a function of time as shown in Fig. 2.9. As we discussed in the previous section, ideally, the visibility of the signal should give us the value of the field autocorrelation function at that delay.

Unfortunately, the laser has a finite coherence length, which results in an extra decay in the measured signals. We can correct this problem by normalizing our data with the data obtained from a reference sample. The reference sample was also a polystyrene suspension but with volume fraction so low (0.2%) that the decay of the

field autocorrelation function caused by the positional fluctuations of the spheres is negligible in the time scales we were measuring. In Fig. 2.10, we show a typical result of the measurement of normalized $g_1(\tau)$.

2.6 Results and Conclusions

In Fig. 2.9 we show two normalized visibility curves taken at delays of $\tau = 0$ and 20 nsec. The amplitude decay of these oscillations results from the motions of the particles. We determined these amplitudes in one nanosecond intervals by the coarse movement of one arm in the interferometer. The decay of visibility, i.e. $g_1(\tau)$, during one experimental run was determined for samples of 0.205-, 0.299-, and 0.460- μm -diameter polystyrene spheres in water for volume fractions, ϕ , ranging from 0.02 to 0.24. By adding an appropriate amount of HCl to the suspension, the particle screening length was kept below 50 Å thereby ensuring that the direct interactions were essentially hard-sphere. The sample cells were immersed in water in order to maintain the sample temperatures at 24°C, and minimize reflections at the sample walls.

Including the effect of absorption, DWS theory gives [9]

$$g_1(\tau) = \int_0^\infty P(s) e^{-\frac{1}{3}k_0^2 \langle \Delta r^2(\tau) \rangle s/l^*} e^{-s/l_a} ds, \quad (2.90)$$

Here k_0 is the wavevector of light in the medium, l^* is the photon random walk steplength [9], l_a is the light absorption length in the medium, and $P(s)$ represents the probability that a photon travels a distance s through the medium before emerging at the detection point. The experiment required very thick sample cells (1 to 5 cm), and thus we had to systematically account for the effects of absorption and geometry in these samples. We independently determined l^* for each of our samples by static transmission and by long-time diffusion measurements using conventional DWS on millimeter-thick samples. The DWS measurements were typically within 5% of our calculations of l^* from Mie theory, but were exceedingly accurate ($\sim 1\%$

variation) and were prone to fewer systematic errors than either the static transmission measurements or the theoretical estimates which require accurate knowledge of sample material properties. We computed $P(s)$ analytically for our cylindrical cells [30] and included the effects of light loss through the cell walls as well as the exact illumination and detection geometries. Finally we performed absolute transmission measurements as a function of cell thickness, which, along with our measured l^* and calculated $P(s)$, enabled us to deduce l_a (1-5 m). Using this information and our measured $g_1(\tau)$, we determined $\langle \Delta r^2(\tau) \rangle$ by inverting eqn. 2.90.

For volume fractions of a few percent and lower, $\langle \Delta r^2(\tau) \rangle$ is accurately obtained from the measured $g_1(\tau)$ using eqn. 2.90. At higher concentrations however, interactions become important and the measured $g_1(\tau)$ can also contain contributions from density fluctuations involving more than one particle, particularly if the mean interparticle distance is less than the wavelength of light. In this case, the quantity $\langle \Delta r^2(\tau) \rangle$ in eqn. 2.90 must be replaced by

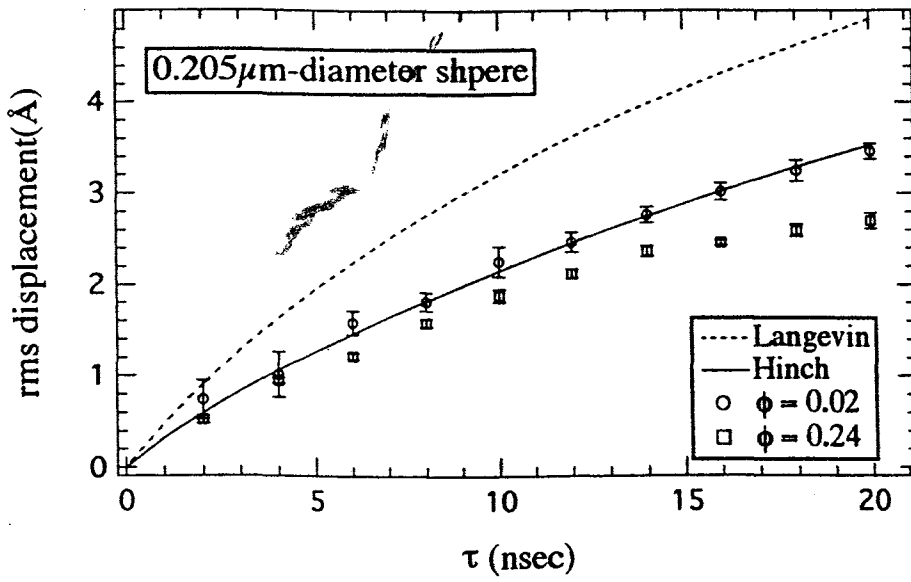
$$\left\{ \langle \Delta r^2(\tau) \rangle + [A(q, \tau)] \right\} / [S(q)], \quad (2.91)$$

where $A(q, \tau) = \frac{1}{N} \sum_{i \neq j}^N \langle \Delta \mathbf{r}_i(\tau) \cdot \Delta \mathbf{r}_j(\tau) e^{i\mathbf{q} \cdot (\mathbf{r}_i(0) - \mathbf{r}_j(0))} \rangle$ is a time and q -dependent factor which accounts for the correlated motions and scattering of different particles, and $S(q)$ is the structure factor of the suspension[37]. The square brackets denote the q -average, $[X] = \int_0^{2k_0 a} X(q) F(q) q^3 dq / \int_0^{2k_0 a} F(q) q^3 dq$, where $F(q)$ is the particle form factor. The structural correction $[S(q)]$, is easily computed within the Percus-Yevick [33] approximation, and works very well for hard spheres at these volume fractions. The quantity $[A(q, \tau)]$ has been calculated for hard spheres at long times when the particles are moving diffusively [34]. In the long time limit, $[A(q, \tau)]$ is ~ 6 times smaller than $\langle \Delta r^2(\tau) \rangle$ for our most concentrated sample of 0.205- μm -diam. spheres. The correction factor rapidly diminishes with both increasing particle size and decreasing volume fraction. $[A(q, \tau)]$ has not been calculated at short times, but must vanish as τ approaches zero. Our data span both dilute and concentrated regimes.

In our analysis we have assumed $[A(q, \tau)]$ is zero, but we have included the structural correction. In Fig. 2.11(a), we show the time-dependent rms displacement, $\sqrt{\langle \Delta r^2(\tau) \rangle}$ of 0.205- μm -diameter particles at two different concentrations. Data from the lowest concentration sample, $\phi = 0.02$, is in excellent agreement with the isolated-particle theory [6]. We emphasize that there are no adjustable or calculated experimental parameters in making this comparison. These results confirm the validity of the hydrodynamic theory down to times much less than the characteristic hydrodynamic time τ_ν^o (12.5 nsec for this sample). At higher concentrations, the data exhibits systematic departures from the isolated-particle theory. At a given delay time τ , the rms displacement of a particle decreases with increasing volume fraction consistent with the expectation that hydrodynamic interactions with neighboring particles effectively impede particle motion. We have observed these effects in all our concentrated samples on time scales significantly less than the time it takes the fluid momentum to diffuse the *mean* distance between nearest neighbor particle surfaces. The measurements suggest that *average particle motion* is still modified by hydrodynamic interactions, but that these interactions arise only occasionally between particles whose distance of closest approach is substantially smaller than the mean particle separation.

Recent experiments [8] and simulations [28] suggest that the time evolution of Brownian particles in concentrated suspensions obeys a remarkable scaling with respect to the isolated-particle theory. Briefly, the isolated-particle theory predicts $\langle \Delta r^2(\tau) \rangle = 6D_o\tau_\nu^o f(\tau/\tau_\nu^o)$, where $D_o = kT/6\pi a\eta$ is the Stokes-Einstein diffusion coefficient, and $f(\tau/\tau_\nu^o)$ is an algebraic function [6]. Scaling is accomplished by replacing D_o and τ_ν^o with the ϕ -dependent functions $D(\phi)$ and $\tau_\nu(\phi)$. In Fig. 2.12 we investigate three different scaling schemes. In each graph we plot a scaled rms displacement, $\{\langle \Delta r^2(\tau) \rangle / 6D(\phi)\tau_\nu(\phi)\}^{1/2}$, as a function of a scaled time, $\tau/\tau_\nu(\phi)$. The first scheme, originally proposed by Zhu et al [8] to explain volume fraction dependent measurements on time scales greater than τ_ν^o , sets $D(\phi) = D_s(\phi) = D_o(1 - 1.83\phi)$

(a)



(b)

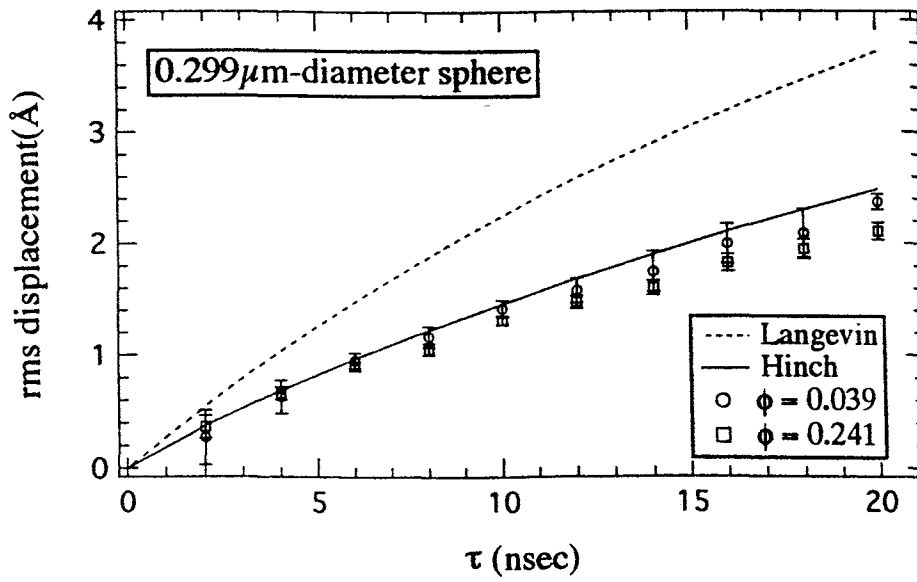


Figure 2.11: rms displacement as a function of time

and $\tau_\nu(\phi) = \rho a^2 / \eta_{\text{HF}}(\phi)$, where $\eta_{\text{HF}}(\phi)$ is the high frequency viscosity of the suspension calculated by Beenakker [36]; in the second scheme, $D(\phi) = D_s(\phi)$ again, but we scale time according to $\tau_\nu(\phi) = \tau_\nu^\circ(1 - 1.83\phi)$; in the third scheme we modify only the viscosity, i.e. $D(\phi) = kT/6\pi a\eta_{\text{HF}}(\phi)$ and $\tau_\nu(\phi) = \rho a^2 / \eta_{\text{HF}}(\phi)$. It is apparent from the figure that all scaling schemes adequately describe the data over the full range of concentrations explored for each sample. Moreover, each of the scaling analyses provides a significantly better description of the data than does the unscaled isolated-particle theory of Hinch. A particularly interesting scenario is provided by the first scaling analysis. Zhu et al interpreted the scaling as evidence that a Brownian particle moves in an effective medium which has the viscosity of the bulk suspension.

Our analysis enlarges the range of viable scaling schemes, and suggests that although the scaling of Zhu et al appears valid for $\tau > \tau_\nu^\circ$, another scaling may underlie the behavior when $\tau < \tau_\nu^\circ$. Further work is needed to clarify this issue.

Finally, we return to reconsider our earlier assumption that the factor $[A(q, \tau)]$ can be neglected in comparison to $\langle \Delta r^2(\tau) \rangle$ in eqn. 2.91. If $[A(q, \tau)] \ll \langle \Delta r^2(\tau) \rangle$, then all the data we present are properly interpreted as the mean square displacement of a tracer particle. This hypothesis is supported by the observation that all of our results are well-described by the scaling analysis, with the possible exception of our longest-time data for our smallest spheres. By contrast, it is possible that some of the measured deviation of the data from the isolated-particle theory arises as a result of non-negligible correlated scattering from different particles. In this case, the *time*-dependence of the deviation implies that the motion of *different* particles is correlated for $\tau < \tau_\nu^\circ$ and that these correlations are *changing* over these same time scales as a result of time-dependent hydrodynamic interactions. Thus, regardless of our assumption about $[A(q, \tau)]$, the data clearly imply that there are significant time-dependent hydrodynamic interactions between different particles which affect particle motion on time scales less than τ_ν° . This surprising result presents a challenge

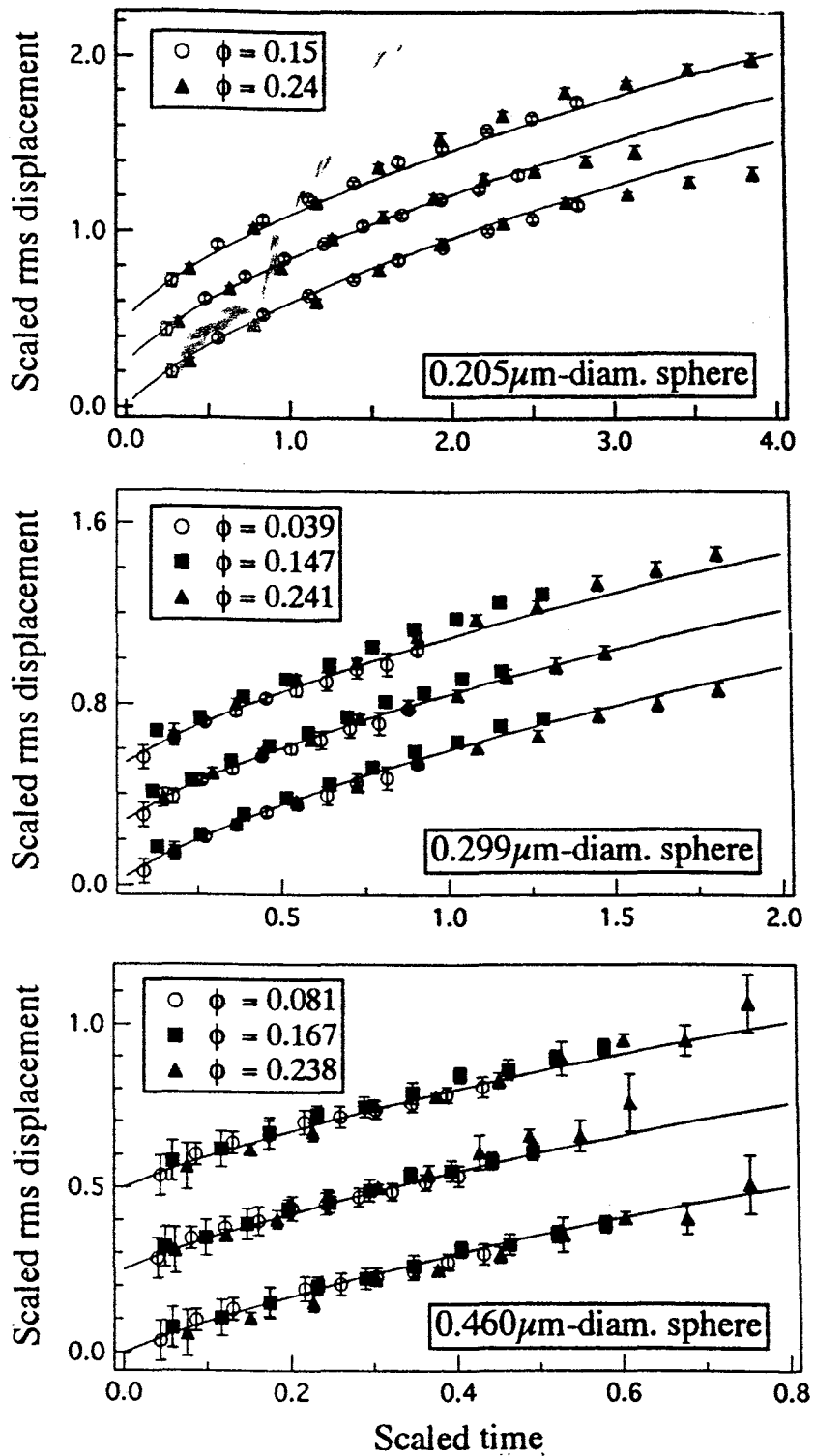


Figure 2.12: Scaled rms displacements

to our current theoretical understanding of many-body hydrodynamic interactions between Brownian particles. In the future, lattice-Boltzmann computer simulations, and q -dependent DWS experiments may provide new insight into these issues.



Chapter 3

Breakdown of DWS

The applicability of DWS depends on the size of the studied system. The photon diffusion approximation, on which DWS is based requires unpolarized light and a sample whose size is much bigger than the transport mean free path l^* . To extend DWS to some practical systems whose sizes may only be several l^* , such as human tissue, one should be careful about the validity of the photon diffusion approximation and thus DWS. In this chapter, we discuss several practical issues concerning the design of DWS experiments in the region where DWS may fail.

3.1 Photon Diffusion Approximation

In principle, all the classical electro-magnetic phenomenon should be able to be explained by solving Maxwell's equations. In only very few cases, however, can one obtain analytical solutions. In the limit of strong multiple scattering in random media, the photon energy density propagates like heat. Therefore, we may guess that the diffusion equation should be useful for problems in multiple light scattering.

The diffusion equation is characterized by the photon diffusion coefficient D_γ . Single scattering, on the other hand, is characterized by a single scattering cross-section σ or photon mean free path l . In the following discussion, we will give a brief

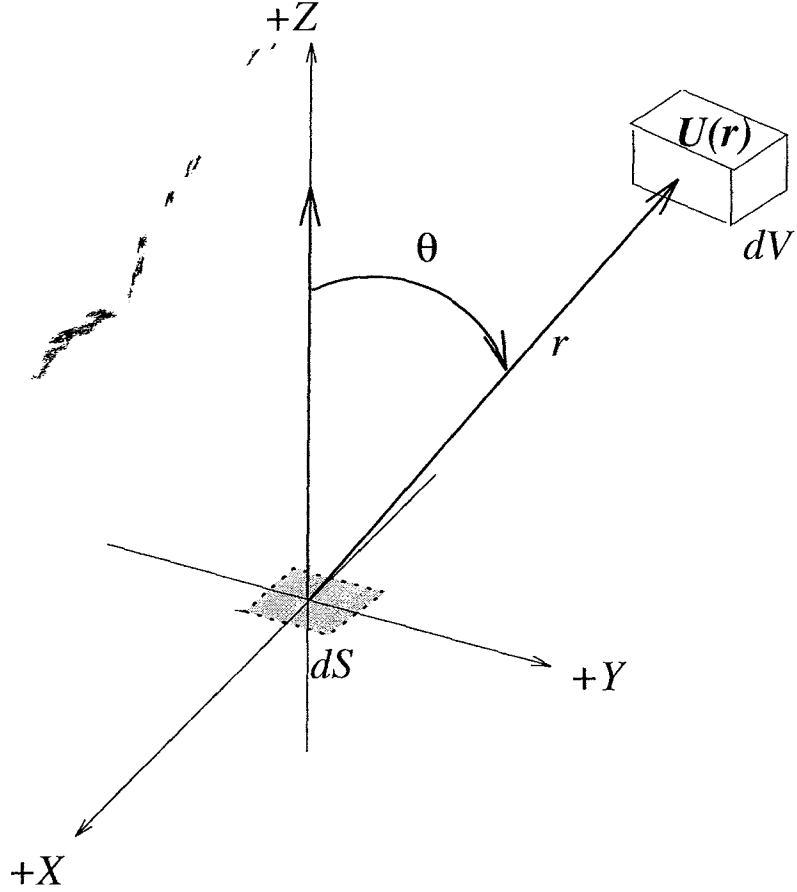


Figure 3.1: Scattering in isotropic medium: $d\mathbf{S}$ is a surface element located at the origin and with its normal vector in the direction of $+Z$. dV is a volume element located at position \mathbf{r} . $U(\mathbf{r})$ is the photon energy density at position \mathbf{r} . θ is the angle between \mathbf{r} and the normal vector of $d\mathbf{S}$.

review about how to link D and l . In a medium consisting of isotropic scatterers, the possibility for a photon to propagate a distance r without being scattered is given by $\exp(-r/l)$ which yields $\langle r \rangle = l$. As shown in Fig. 3.1, the number of photons which are scattered per unit time from a volume element dV in the $+z$ half-plane and reach the area element dS (with its normal vector in the $+z$ direction) without being scattering is given by:

$$\frac{v}{l} \left(\frac{dS \cos \theta}{4\pi r^2} \right) U(\mathbf{r}) e^{-r/l}, \quad (3.1)$$

where r is the distance between the volume element dV and surface element dS , θ

is the angle between \mathbf{r} and the normal vector of dS , $U(\mathbf{r})$ is the photon density at position \mathbf{r} , and v is the speed of light in the medium. First we assume that the variation in U over a distance l is small and then we can approximate U by a Taylor expansion to linear order:

$$U(\mathbf{r}) \approx U(\mathbf{r}_o) + (\mathbf{r} - \mathbf{r}_o) \cdot (\nabla U)_o. \quad (3.2)$$

To obtain the flux of photons into dS (in the $-z$ direction), we integrate the above equation over all available volume in the half-plane $z > z_o$. In the case that \mathbf{r}_o is far from the boundaries and the size of the medium is much larger than l , the integration can be carried out by integrating over all the half-plane $z > z_o$ due to the fact that the contributions from the remote positions are diminished by the factor $\exp(-r/l)$. The photon flux in the $-z$ direction, J_- , then is given by

$$J_-(z) = \frac{Uv}{4} + \frac{vl}{6} \frac{\partial U}{\partial z}. \quad (3.3)$$

Similarly, the photon flux in the $+z$ direction, J_+ , is given by integrating over the half-plane $z < z_o$

$$J_+(z) = \frac{Uv}{4} - \frac{vl}{6} \frac{\partial U}{\partial z}. \quad (3.4)$$

The net flux $J \equiv J_+ - J_-$ then is given by

$$J(z) = -\frac{vl}{3} \frac{\partial U}{\partial z}. \quad (3.5)$$

From the relation between the flux and the energy gradient,

$$\mathbf{J} = -D\nabla U, \quad (3.6)$$

it is now obvious that the diffusion coefficient D_γ is related to l as

$$D_\gamma = vl/3. \quad (3.7)$$

For anisotropic scatters, the mean free path l should be replaced by the transport mean free path l^* which is the length scale over which the photon can be considered diffusing. It can be proved that[22]

$$D_\gamma = vl^*/3, \quad (3.8)$$

and we have the photon diffusion equation

$$\frac{\partial U}{\partial t} = \frac{v l^*}{3} \nabla^2 U \quad (3.9)$$

Note that eqn. (3.9) is only valid over volumes of at least several l^* . When we want to apply the diffusion equation to a practical problem, we also need the boundary conditions. The typical boundary conditions used with the photon diffusion equation assume there exists an extrapolation length z_e outside the sample where the energy density drops to zero. Typically, z_e is in the order of l^* . When the size of the sample is much larger than l^* , z_e has no significant effect. For a planar boundary condition, assuming that the scattering medium is in the $z < 0$ region, there is no flux from the $z > 0$ region and flow in the $-z$ direction. In another words,

$$J_-(z = 0) = 0. \quad (3.10)$$

This gives

$$U + \frac{2l^*}{3} \left(\frac{\partial U}{\partial z} \right)_{z=0} = 0, \quad (3.11)$$

and we then have $z_e = 2l^*/3$. As we send a laser beam into the scattering medium, it will not be diffusive right at the incident boundary. Phenomenologically, we may assume that the light begins to diffuse at the location αl^* away from the boundary. α usually is taken to be 1. To be more rigorous, one also can distribute the source exponentially along the incident direction[35].

To further understand the diffusion behavior of photons, it worths solving the diffusion equation for a slab geometry. As shown in Fig. 3.2, the scattering medium is bounded in the region $0 < z < L$. The diffusion equation can now be reduced to a one-dimensional problem whose solution is given by

$$U = U_o \begin{cases} \left(1 + \frac{z}{2l^*/3} \right) & \text{for } z < \alpha l^* \\ \frac{1+\alpha/(2/3)}{L+(2/3-\alpha)l^*} (L + \frac{2}{3}l^* - z) & \text{for } z > \alpha l^* \end{cases} \quad (3.12)$$

One schematic of the solution is given in Fig. 3.2. Eqn. (3.12) gives the expression

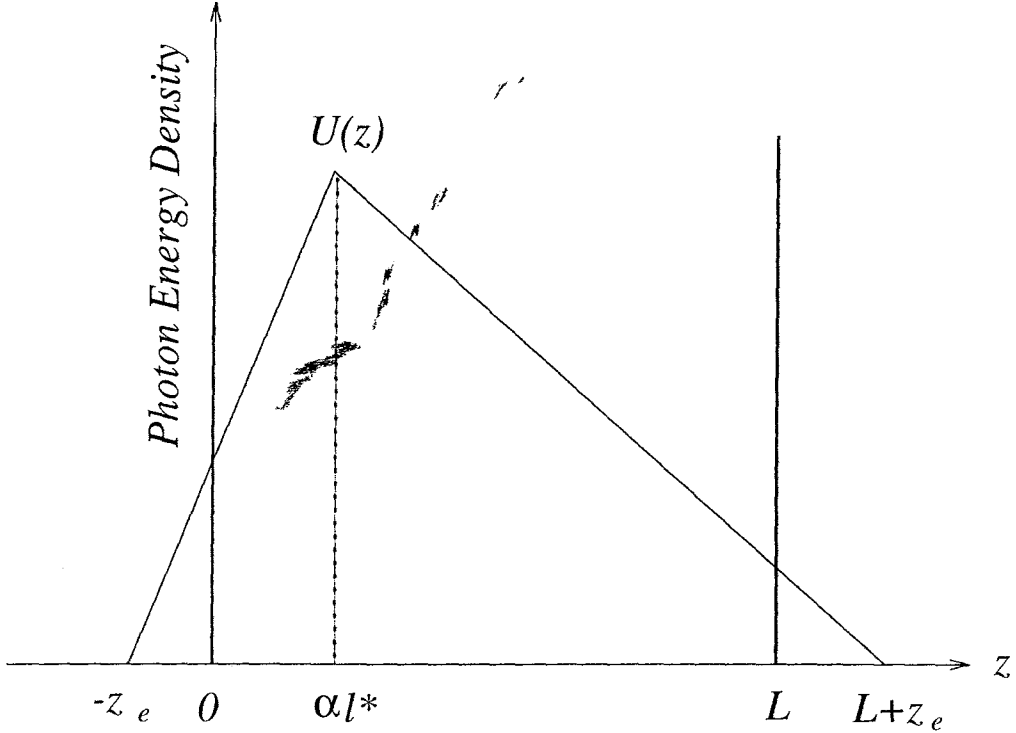


Figure 3.2: Photon diffusion in one-dimension

of the total transmission T as the following

$$T = \frac{5l^*}{3L} \left(1 + \frac{4l^*}{3L}\right)^{-1}. \quad (3.13)$$

When L is much bigger than l^* , the total transmission depends linearly on l^* and is inversely proportional to L . This also offers a rule of thumb to judge whether the scattering is diffusive or not.

Now, let's turn to the calculation of $g_1(\tau)$. Since in most cases, the timescale that DWS is used as a probe is in the diffusive limit, we will use the approximation $\Delta r^2(\tau) \sim 6D\tau$ in the following discussion. From eqn. (2.32) we know that we have to calculate $P(s)$, which is the probability distribution for a photon to travel a length s through the medium. $P(s)$ is proportional to the time spectrum of the photon current at the collection position \mathbf{r}_{out} for an input δ -function pulse in time, i.e.

$$P(s) \propto |J_{out}(\mathbf{r}, t)|_{\mathbf{r}_{out}} = |D_\gamma \nabla U \cdot \hat{\mathbf{n}}|_{\mathbf{r}_{out}} = \frac{vU}{2}|_{\mathbf{r}_{out}}. \quad (3.14)$$

In experiment, $P(s)$ can be measured by applying the nonlinear optical gating technique on sub-nanosecond and nanosecond time scales[31]. In general, the photon diffusion equation is proved valid. Now, let's take the slab we just discussed. We first calculate $g_1(\tau)$ in the transmission case for a plane wave incident beam. Assuming that the δ pulse is located at z_o , and one can prove that[11]

$$g_1(\tau) = \frac{\frac{L/l^*+4/3}{z_o/l^*+2/3} \left\{ \sinh \left[\frac{z_o}{l^*} \sqrt{\frac{6\tau}{\tau_o}} \right] + \frac{2}{3} \sqrt{\frac{6\tau}{\tau_o}} \cosh \left[\frac{z_o}{l^*} \sqrt{\frac{6\tau}{\tau_o}} \right] \right\}}{\left(1 + \frac{8\tau}{3\tau_o} \right) \sinh \left[\frac{L}{l^*} \sqrt{\frac{6\tau}{\tau_o}} \right] + \frac{4}{3} \sqrt{\frac{6\tau}{\tau_o}} \cosh \left[\frac{L}{l^*} \sqrt{\frac{6\tau}{\tau_o}} \right]}, \quad (3.15)$$

where $\tau_o \equiv (Dk_o^2)^{-1}$. As $\tau \ll \tau_o$, we have a simpler expression :

$$g_1(\tau) \approx \frac{\left(\frac{L}{l^*} + \frac{4}{3} \right) \sqrt{\frac{6\tau}{\tau_o}}}{\left(1 + \frac{8\tau}{3\tau_o} \right) \sinh \left[\frac{L}{l^*} \sqrt{\frac{6\tau}{\tau_o}} \right] + \frac{4}{3} \sqrt{\frac{6\tau}{\tau_o}} \cosh \left[\frac{L}{l^*} \sqrt{\frac{6\tau}{\tau_o}} \right]}. \quad (3.16)$$

In some cases, particularly when large light powers are needed, a point source geometry should be considered. One can obtain in this case

$$g_1(\tau) = C \int_{(L/l^*)\sqrt{6\tau/\tau_o}}^{\infty} J_o \left(\frac{R}{L} \sqrt{\xi^2 - \left(\frac{L}{l^*} \right)^2 \frac{6\tau}{\tau_o}} \right) B(\xi, \epsilon, \zeta) \xi e^{-(1-\zeta)\xi} d\xi, \quad (3.17)$$

where $\epsilon \equiv l^*/(3L)$, $\zeta \equiv z_o/L$, C is a normalization constant, and $J_o(\dots)$ is the zero-th order Bessel function. The function $B(\xi, \epsilon, \zeta)$ is given by

$$B(\xi, \epsilon, \zeta) = \frac{2\epsilon \left[(1 + \epsilon\xi) - (1 - \epsilon\xi)e^{-2\zeta\xi} \right]}{(1 + \epsilon\xi)^2 - (1 - \epsilon\xi)^2 e^{-2\zeta\xi}}. \quad (3.18)$$

The point source geometry, however, has the disadvantage that it may cause significant local heating. In this case, a incident beam with finite diameter is most desirable. Since the output profile of a laser beam is often Gaussian, an expression of $g_1(\tau)$ for a Gaussian incident beam is useful. We can use eqn. (3.17) as the starting point. Assuming an instantaneous Gaussian source with width d , i.e.

$$U(x, y, z, t) = U_o e^{-4(x^2+y^2)/d^2} \delta(z - z_o, t), \quad (3.19)$$

one can prove that

$$g_1(\tau) = C' \int_{(L/l^*)\sqrt{6\tau/\tau_o}}^{\infty} e^{-(\xi^2 - (\frac{L}{l^*})^2 \frac{6\tau}{\tau_o})(\Delta/4)^2} B(\xi, \epsilon, \zeta) \xi e^{-(1-\zeta)\xi} d\xi, \quad (3.20)$$

where $\Delta \equiv d/L$ and C' is a normalization factor. Another geometry commonly used in DWS experiments is the backscattering geometry. In some situations, it is not convenient nor possible to perform a transmission experiment, the backscattering geometry provides great advantage. One also can obtain $g_1(\tau)$ in this case for an instantaneous planar source at $z = z_o$ as

$$g_1(\tau) = \frac{\sinh \left[\sqrt{\frac{6\tau}{\tau_o}} \left(\frac{L}{l^*} - \frac{z_o}{l^*} \right) \right] + \frac{2}{3} \sqrt{\frac{6\tau}{\tau_o}} \cosh \left[\sqrt{\frac{6\tau}{\tau_o}} \left(\frac{L}{l^*} - \frac{z_o}{l^*} \right) \right]}{\left(1 + \frac{8\tau}{3\tau_o} \right) \sinh \left(\sqrt{\frac{6\tau}{\tau_o}} \frac{L}{l^*} \right) + \frac{4}{3} \sqrt{\frac{6\tau}{\tau_o}} \cosh \left(\sqrt{\frac{6\tau}{\tau_o}} \frac{L}{l^*} \right)}. \quad (3.21)$$

For a sample with infinite thickness, the above expression reduces to

$$g_1(\tau) = \frac{\exp \left[-\frac{z_o}{l^*} \sqrt{\frac{6\tau}{\tau_o}} \right]}{1 + \frac{2}{3} \sqrt{\frac{6\tau}{\tau_o}}}. \quad (3.22)$$

If $\tau \ll \tau_o$, we also have a very simple form

$$g_1(\tau) \sim e^{-\left(\frac{z_o}{l^*} + \frac{2}{3}\right) \sqrt{\frac{6\tau}{\tau_o}}}. \quad (3.23)$$

In practice, though it was found that the backscattering data can be well fitted by

$$g_1(\tau) = e^{\gamma \sqrt{\frac{6\tau}{\tau_o}}}. \quad (3.24)$$

The value of γ does not always agree with $\frac{z_o}{l^*} + \frac{2}{3}$ and also depends on the polarization of collected photons[26, 27]. This discrepancy originates in part from the fact that a significant part of the collected photons in the backscattering geometry are not diffusive photons.

3.2 Practical Considerations in Applying DWS

In most cases, the scattering medium is stored in a container whose refractive index may be different from that of the medium. The index mismatch causes reflections at the boundaries. The reflected flux of photons modifies the local energy densities near the boundaries. More specifically, it reduces the gradient of the energy density. The reflected flux effectively increases the extrapolation length. Zhu, Pine and

Weitz calculated the average diffusive reflectivity R for a planar boundary[37]. They obtained

$$R = \frac{3C_2 + 2C_1}{3C_2 - 2C_1 + 2}, \quad C_n = \int_0^{\pi/2} R(\theta) \cos^n \theta \sin \theta d\theta, \quad (3.25)$$

where θ is the incident angle of photon and $R(\theta)$ is the angular dependent reflectivity. Again, let's assume the scattering medium is in the $z < 0$ region; now we have

$$J_-(z \leq 0) = RJ_+(z \leq 0). \quad (3.26)$$

Inserting the expression of J_+ and J_- in eqns. (3.4) and (3.5), we have

$$U + \left(\frac{1+R}{1-R} \right) \frac{2l^*}{3} \left(\frac{\partial U}{\partial z} \right)_{z=0} = 0. \quad (3.27)$$

In this case, we can see that the extrapolation length is modified by a factor of $(1+R)/(1-R)$.

To further evaluate the diffusive reflectivity, let's consider the light propagation problem sketched in Fig. 3.2. Region 1 with refractive index n_1 is the scattering medium, region 2 with refractive index n_2 is a cylindrical optical window with diameter D and thickness d , and region 3 with index n_3 is the surrounding medium. We also use the R_{ij} and T_{ij} to denote the polarization-averaged Fresnel reflection and transmission coefficients for light propagates from medium i into medium j , respectively. R_{ij} and T_{ij} are given by

$$T_{ij} = \frac{1}{2} \left\{ \left(\frac{2n_i \cos \theta_i}{n_i \cos \theta_i + \sqrt{n_j^2 - n_i^2 \sin^2 \theta_i}} \right)^2 + \left(\frac{2n_i n_j \cos \theta_i}{n_j^2 \cos \theta_i + n_i \sqrt{n_j^2 - n_i^2 \sin^2 \theta_i}} \right)^2 \right\},$$

$$R_{ij} = 1 - T_{ij}. \quad (3.28)$$

Here θ_i is the angle between the light direction and the normal vector of the interface. In addition to the diffusive reflection coefficient between a multiple-scattering sample and a nonscattering external medium $R_{12}(\theta_1)$, we consider light that propagates to the second boundary and is reflected back into the sample, increasing the reflectivity by $T_{12}(\theta_1)R_{23}(\theta_2)T_{12}(\theta_2)$. We use Snell's law to calculate $\theta_2(\theta_1)$. Due to the finite size of the container, only a limited number of multiple reflections should

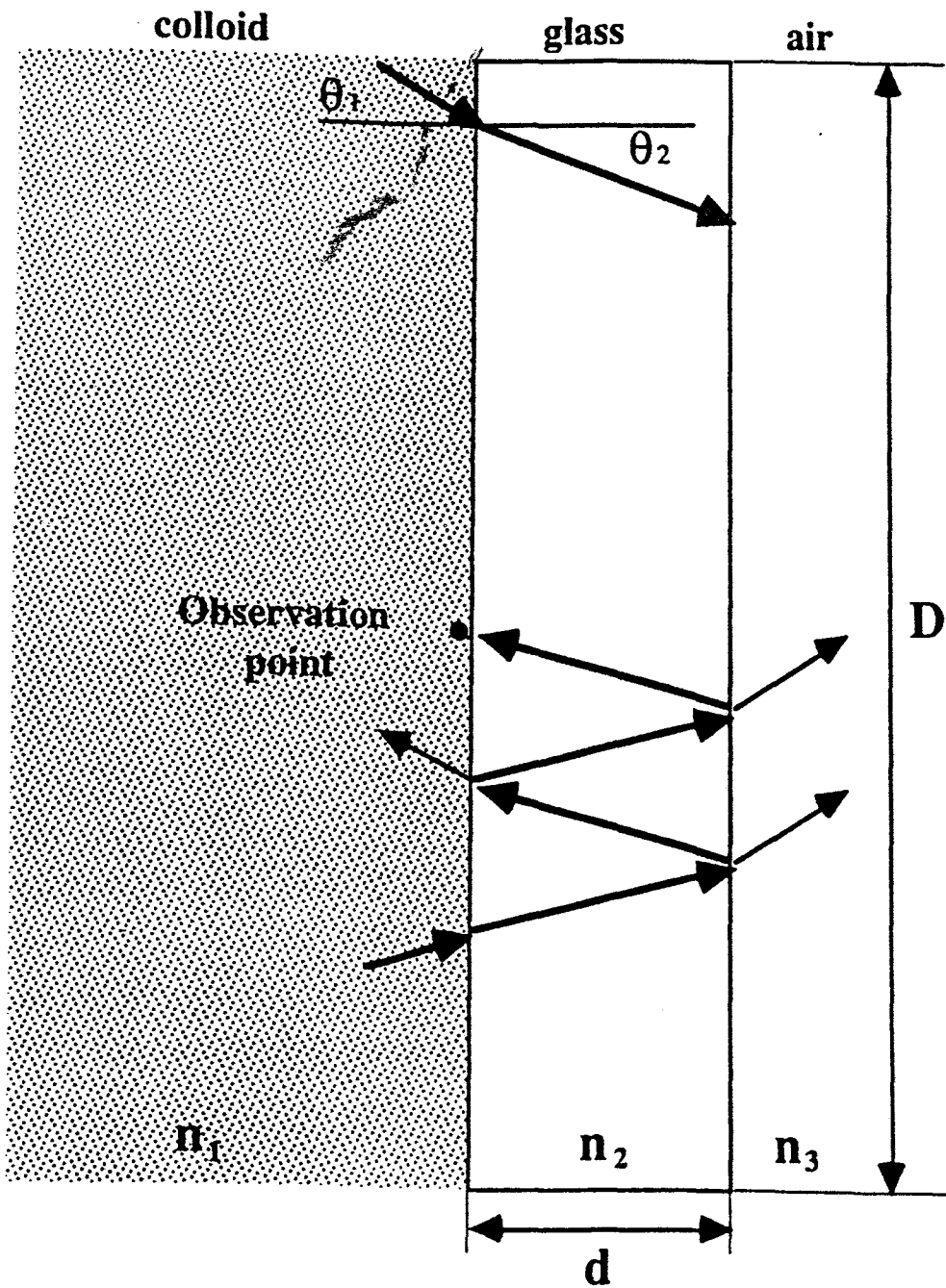


Figure 3.3: Reflection at boundaries

be considered. At each reflection, a photon propagates a distance $2d \tan(\theta_2)$ along the sample's surface. We choose to ignore multiple reflections that require that the photon be translated by more than half of the cell diameter D . That is to say, the number of reflections N_m included in the calculation is the biggest integer less than $D/4d \tan(\theta_2)$. The total angular-dependent reflection coefficient is then given by

$$\begin{aligned}
 R(\theta_1) &= R_{12}(\theta_1) + T_{12}(\theta_1)R_{23}(\theta_2)T_{21}(\theta_2) \times \sum_{j=0}^{j=N_m(\theta_2)} [R_{21}(\theta_1)R_{23}(\theta_2)]^j \\
 &= R_{12}(\theta_1) + T_{12}(\theta_1)R_{23}(\theta_2)T_{21}(\theta_2) \times \frac{1 - [R_{21}(\theta_1)R_{23}(\theta_2)]^{N_m(\theta_2)}}{1 - R_{21}(\theta_1)R_{23}(\theta_2)}. \quad (3.29)
 \end{aligned}$$

Inserting $R(\theta)$ into eqn. 3.25, we can obtain the diffusive reflectivity and use it to calculate effective extrapolation length. The value of N_m can be important when D/d is not big. For a colloid-glass-air system, the diffusive reflectivity is about 40% for $D/d = \infty$ when it is only about 10% for $D/d \sim 10$. It is interesting that the constraint of finite sample size can decrease the influence of the reflections that occur at the boundaries.

As we know, Maxwell's equations are vector equations while the diffusion equation is a scalar equation. The validity of using the photon diffusion equation also requires an unpolarized light. To obtain powerful, single-frequency light source, we have to use a laser, which is usually polarized. As the photon scatters in the medium, not only is its direction of propagation randomized, but also the direction of polarization is randomized. This suggests that the thickness required to observe a unpolarized emerging flux may be related to the thickness required for DWS to be valid.

In the experiment we are going to discuss in the next section, we would like to answer the following questions:

1. How big the beam size is needed to use plane-wave solution accurately?
2. How thick must the sample be to make DWS valid for a slab geometry?
3. How big is the effect of index mismatch?
4. How important is the polarization effect?

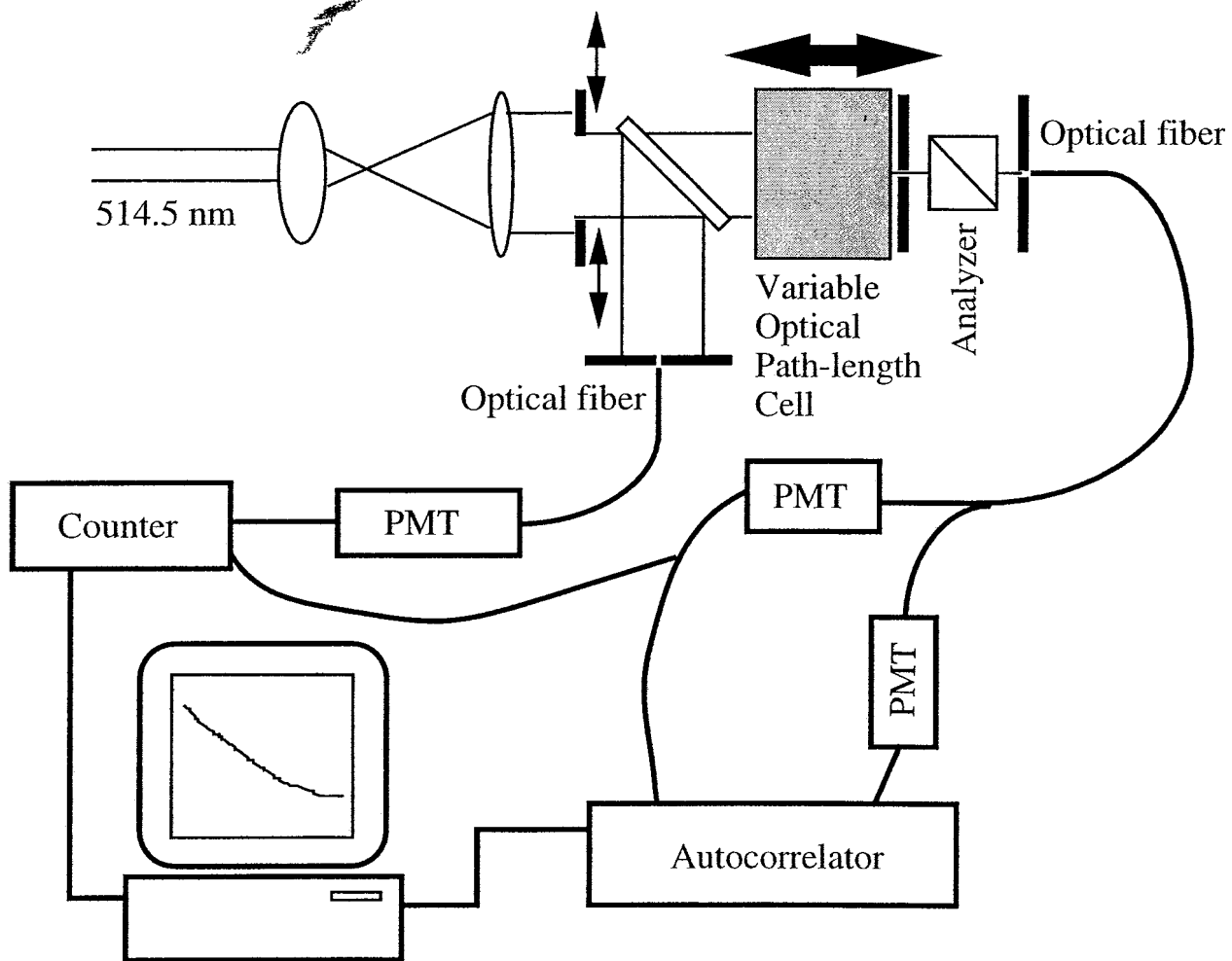
With these questions answered, scientists and engineers can have a rule of thumb in designing DWS experiments or equipment based on DWS.

3.3 Experiment Set-up

Our DWS measurement apparatus is shown in Fig. 3.4, which is a typical DWS set-up except that a variable thickness cell is used. The apparatus consists of an Argon ion laser operating at a wavelength of 514.5 nm, a spatial filter, and collimating optics that produced a Gaussian beam with a FWHM of 2 cm; the central 2 cm of the beam is allowed to illuminate the sample. A single speckle of transmitted light was selected by two pinholes. The polarization direction of the transmitted light can also be selected by an analyzer. The ratio of transmitted light to reflected intensities was measured and compared with a standard sample for calibration. In the dynamic measurements, two PMTs were used to minimize the effects of after-pulsing in the PMT, i.e. cross-correlation technique was used.

Conventionally, the volume fraction is used to adjust the ratio of l^* to the cell thickness L . This, in fact, is prone to systematic effects. In order to minimize the systematic effects that might arise in sample preparation, we used a variable thickness cylindrical cell whose thickness can range from $50\mu\text{m}$ to 5mm and whose diameter is 2cm . This cell was constructed of stainless steel with Teflon seals and quartz windows. The partially reflecting steel boundary is not important because the thickness of the sample is much less than the diameter of the sample. The cell's path length was calibrated against a fixed thickness cuvette in spectrophotometer by the use of a green dye (McCormick's food coloring) with two absorption peaks. From this calibration, the accuracy in the thickness reading was within $5\mu\text{m}$. Samples were prepared with polystyrene spheres with diameters of 137, 205, 299, 460, 825, 2000, and 3400 nm. The volume fraction for each sample was chosen to make $l^* \sim 130\mu\text{m}$, which was about 0.017. This volume fraction was low enough that the inter-particle

Figure 3.4: Experiment set-up in probing the limitation of DWS



hydrodynamic interaction can be neglected. The value of l^* also made the variable thickness cell provide sample thickness up to $30l^*$ where the validity of DWS is well recognized. For the static transmission measurement, the data is analyzed using the following procedures:

1. We assume the data point at large thickness ($\sim 4mm$) is accurately described by the photon diffusion equation. The measured transmission intensity at that thickness is referred to as T_{ref} , the reference transmission.

2. From eqn. (3.5), we have

$$\frac{T}{T_{ref}} = \frac{L_{ref} + (4/3)l^*}{L + (4/3)l^*}. \quad (3.30)$$

We scale all transmission data points with T_{ref} .

3. From eqn. (3.30), we calculate l^* as a function of thickness L for every data point, i.e.

$$l^*(L) = \left(\frac{3}{4}\right) \frac{L_{ref} - \left(\frac{T}{T_{ref}}\right) L}{\left(\frac{T}{T_{ref}}\right) - 1}. \quad (3.31)$$

This equation, however, can not give l^* at $L = L_{ref}$. Since l^* is an intrinsic property of the studied sample, the derived $l^*(L)$ should be a constant in the region where DWS is valid. For the thickness where $l^*(L)$ begins to deviate from this constant value, DWS is not valid anymore.

In the dynamic measurements, the measured intensity autocorrelation function was converted into the field autocorrelation function $g_1(\tau)$ by using the Siegert relation. Assuming the knowledge of the dynamics of the system which is well understood in these time and volume fraction regimes, $g_1(\tau)$ was then fitted with eqn. 3.15 to derive l^* for various L . We investigated how the values of these derived l^* s depend on the sample thickness L and we determined at what thickness DWS fails.

To determine how big the beam diameter has to be for using the plane-wave/slab geometry, we performed dynamics measurements for a 4.4% 0.460 μ m-diam. system with cell thickness $L = 750\mu$ m. The diameter of incident beam is controlled by an

iris to vary from 1 mm to 20mm. To check the influence of the reflections that occur at the boundary, we not only carried out measurements with a sample in air, but also with sample immersed in water.

3.4 Results and Conclusions

To test the breakdown of DWS, we first performed the static transmission measurements for various cell thicknesses. We also used an analyzer to select different output polarization during the experiment, which enabled us to test the validity of scalar photon diffusion approximation. In Fig. 3.5, we plotted the measured static transmission data vs. the ratio of cell thickness to transport mean free path, L/l^* , for three polarization channels. In the following discussions, the parallel(perpendicular) channel means the polarization direction of the detected light is parallel(perpendicular) to the polarization direction of the incident beam. As shown in Fig. 3.5, when we decrease the ratio L/l^* , the static transmission data for different polarization channels begin to deviate from one another at $L \sim 9l^*$. When we decrease the ratio L/l^* from 9 to 5, the measured static transmission for the parallel polarization channel increases more than fifteen times while the perpendicular channel increases less than two times. This indicates a significant number of non-diffusive photons in the parallel polarization channel.

For the convenience of discussion, we name the thickness at which the two polarization channels deviate from each other by about 10% as the depolarization thickness L_{dp} . Phenomenologically, L_{dp} indicates a thickness required for a polarized incident light to become unpolarized in the transmission measurement. Here we emphasize that the introduction of L_{dp} is for practical reasons and thus lacks of rigorous theoretical foundation. In Fig. 3.4, we show the experimental results for a $0.205\mu\text{m}$ -diameter polystyrene sphere suspension with volume fraction $\phi = 0.0163$. The inverted l^* is normalized by l_{Mie}^* which is the l^* calculated using Mie theory

Particle diameter $d=0.205\mu\text{m}$

$l^*_{\text{Mie}}=130\mu\text{m}$ $\phi=0.0163$

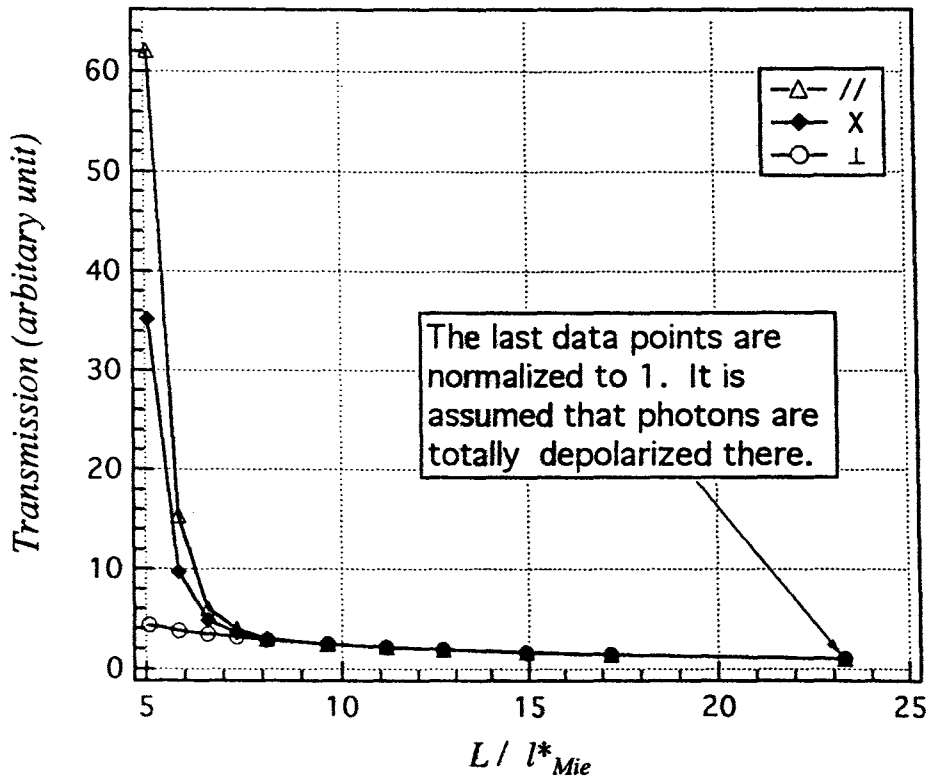


Figure 3.5: In this graph, we show static transmission as a function of cell thickness for different polarization channels. The triangle symbols represent the data obtained with the output polarization parallel to the input polarization. The solid diamond symbols represent the data obtained with the output polarization 45° off the input polarization. The circle symbols represent the data obtained with the output polarization perpendicular to the input polarization.

and eqn. 2.34. The cell thickness L is also normalized by l_{Mie}^* for easy comparison. From the graphs, we can see that L_{dp} is about $9 l^*$ for both static transmission measurement and dynamic measurement.

We also see that, both in the static transmission and the dynamic measurement, the inverted l^* for the *perpendicular* channel is better described by DWS and by the scalar photon diffusion approximation than for the *parallel* channel. One simple reason for this is that the photons in the perpendicular channel typical scatter more times in order to get their polarization direction to change by 90° .

The deviation of two polarization channels, of course, indicates that scalar photon diffusion is not valid for the sample with thickness smaller than L_{dp} for a polarized incident light source. If we can provide an unpolarized light source or if we select only the perpendicular channel, the valid region for scalar photon diffusion equation apparently can be pushed toward to smaller thicknesses.

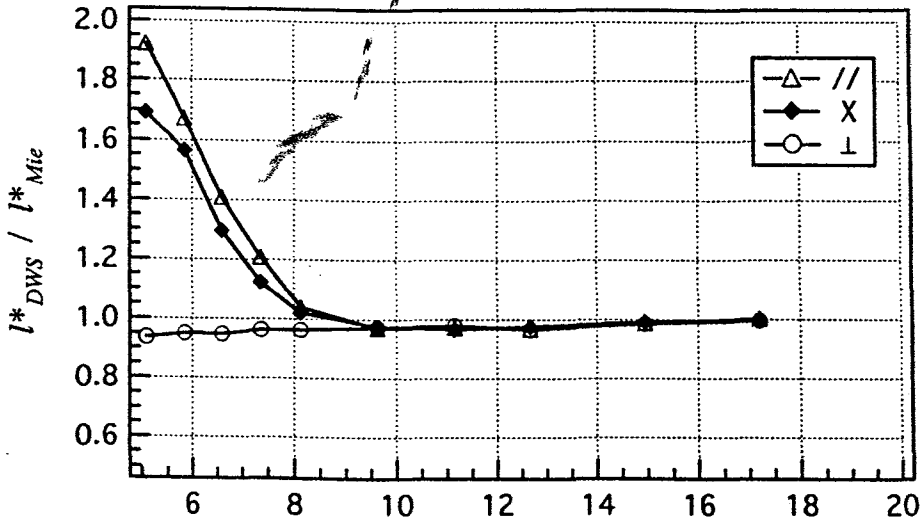
For practical reasons, it is useful to understand how the depolarization thickness depends on the size of the particle. We performed a series of measurements with the green line ($\lambda = 514.5\text{nm}$) of an Ar-Ion laser to determine L_{dp} in systems with sphere diameter ranging from $0.14\mu\text{m}$ to $3.4\mu\text{m}$. In Fig. 3.7, we plot L_{dp} as a function of sphere diameter. For the sphere diameter bigger than $1.0\mu\text{m}$, our result suggests L_{dp} reach a asymptotic value about $6l^*$. On the other hand, L_{dp} can be as big as $12l^*$ for sphere diameter smaller than $0.14\mu\text{m}$. This dependence on the particle size is interesting. Qualitatively, it may be explained by the following argument: For the same value of l^* , from Mie theory, a photon has to scatter many more times to get its direction randomized in the big particle suspension than in the small particle suspension. Therefore, there are less non-diffusive photons in the parallel channel for the big particle suspension. Though theoretical treatment regarding polarization dependence of diffusive light has been proposed[38], it is very difficult to apply the theory to the finite geometry of our experiments.

In Fig. 3.8, we plotted the inverted l^* obtained by fitting measured $g_1(\tau)$ with

Particle diameter $d=0.205\mu\text{m}$

$$l^*_{Mie}=130\mu\text{m} \quad \phi=0.0163$$

Dynamic measurement



Static Transmission measurement

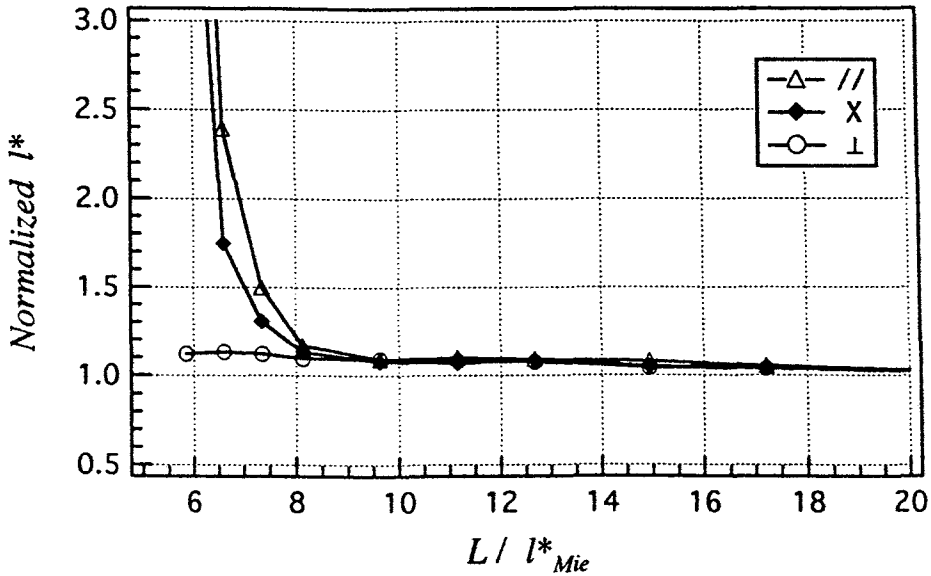


Figure 3.6: Results obtained from static and dynamic measurements: l^*_{DWS} is the inverted l^* obtained by fitting the measured $g_1(\tau)$ with eqn. 3.14. l^*_{Mie} is the l^* calculated by using Mie theory and eqn. 2.34. In the static transmission graph, Y-axis is the ratio of the l^* obtained by the procedure described in Section 3.3 to l^*_{Mie} . L is the cell thickness. The meanings of the symbols are the same as in the previous figure

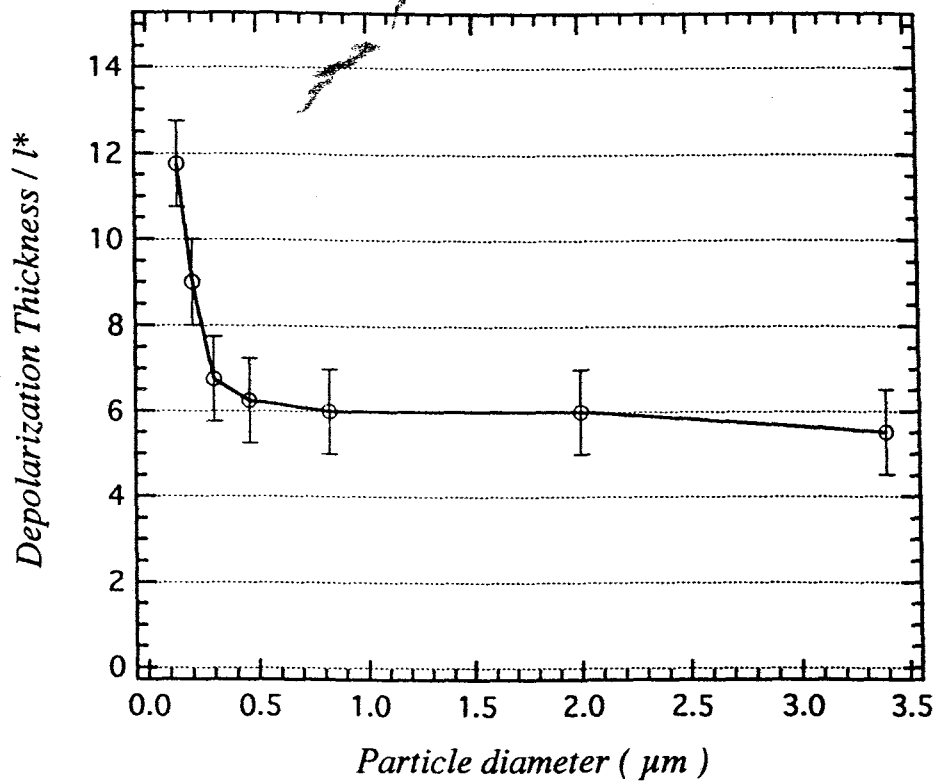


Figure 3.7: Depolarization thickness as a function of particle diameter: All the samples are prepared with l^* about $140\mu\text{m}$.

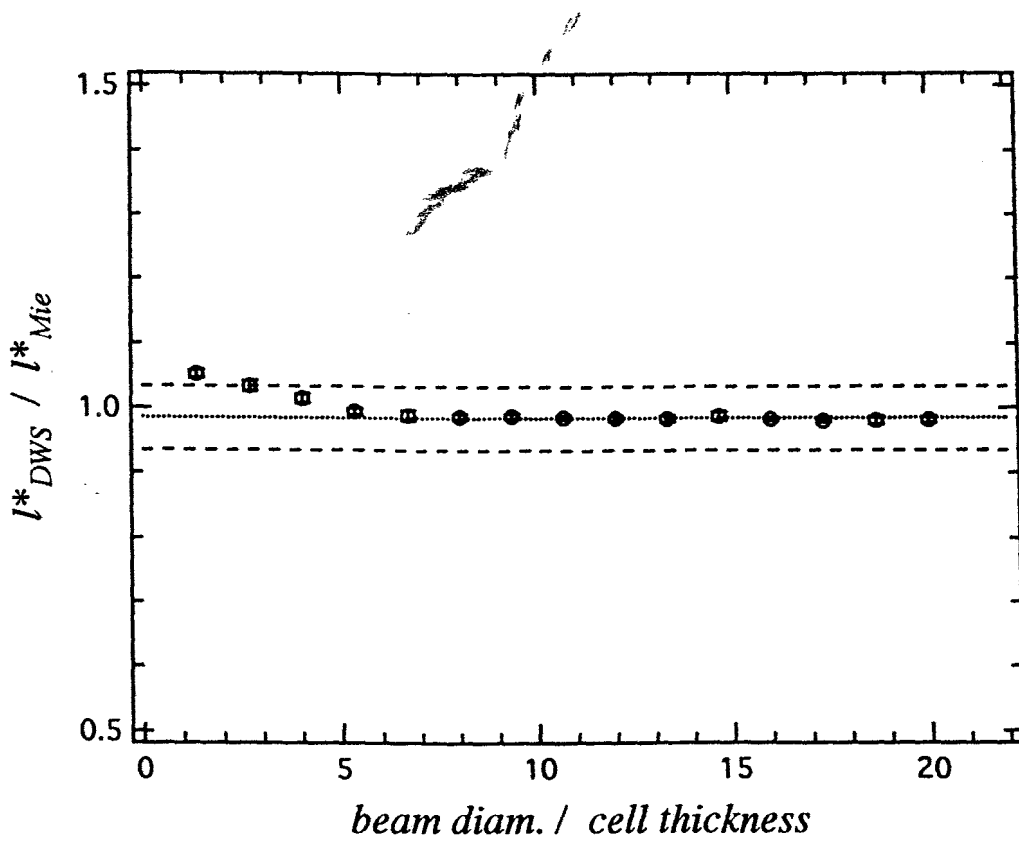


Figure 3.8: When can use the plane-wave/slab solution in DWS? The studied sample was a 4.4%, $0.460\mu\text{m}$ -diam. polystyrene spheres suspension with cell thickness $L = 750\mu\text{m}$. The beam diameter was controlled by a variable iris whose diameter ranged from 1 mm to 20 mm

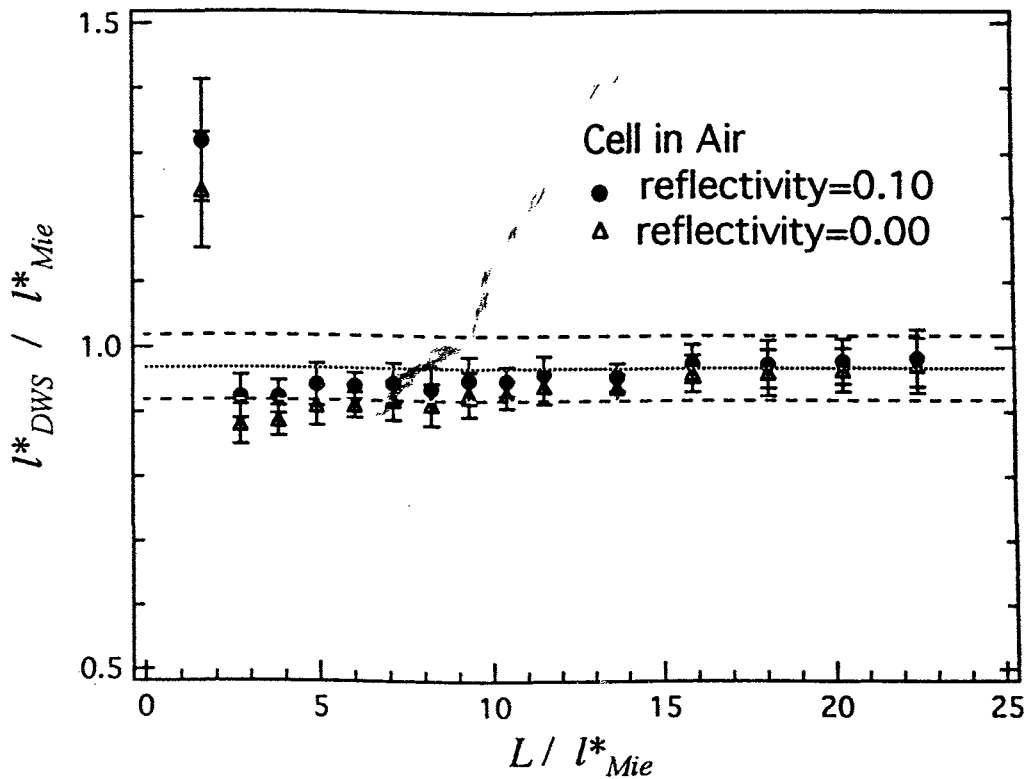


Figure 3.9: Effect of reflection at boundaries: Dynamical measurement was performed for a 1.6%, $0.460\mu\text{m}$ -diam. polystyrene spheres suspension for various cell thickness. The sample cell was not immersed in water. The inverted l_{DWS}^* was calculated with and without considering the diffusive reflectivity.

the plane-wave/slab solution, eqn. 3.15, as a function of D_b/L which is the ratio of the beam diameter to the cell thickness. We see that, as D_b/L is larger than 7, the inverted l^* keeps at a constant value. This indicates the regime for which the plane-wave/slab geometry solution for photon diffusion equation can be used accurately in the analysis of DWS data. This result provides a simple rule of the thumb in designing DWS experiment.

To test the effect of diffusive reflections at the boundaries, in Fig. 3.9, we plotted the measurement result for the sample without being immersed in water. The effective diffusive reflectivity was estimated to be about 10% by using eqns. 3.29 and 3.25. The data were analyzed both with and without reflection correction. As we

can see, the difference between two data sets is more significant in the small values of thickness.

In conclusion, this experiment provides useful information in designing DWS experiment. Especially, as DWS has been widely applied in biological systems where l^* can be comparable to the size of the sample itself, our experimental result, at least, provides a coarse judgment of the validity of the data obtained by DWS measurement. We suggest that one should use the perpendicular channel if polarized light source is used. To use plane-wave/slab geometry, the diameter of the laser beam should be bigger than $7l^*$.

Chapter 4

Multiple Light Scattering in Nematic Liquid Crystals

Diffusing-Wave Spectroscopy has been successfully applied in many systems. So far, however, the studied systems are limited to isotropic turbid media. As a result, one is certainly tempted to extend its application to anisotropic media. In this chapter, we choose nematic liquid crystals as a model system of an anisotropic turbid medium, and we study the validity of DWS in this system.

4.1 Director Fluctuations in Nematic Liquid Crystals

In a conventional crystal, the constituent molecules or atoms are located periodically in space. In liquids, this kind of periodicity does not exist, although local positional correlations are present. Typically, when a crystal is heated to certain temperature, the periodicity is destroyed and the material turns into liquid. Interestingly, in the organic materials we study here, simple transitions from solid to liquid do not occur, but rather a cascade of transitions involving new phases occur. These new phases are intermediate between those of a liquid and those of a crystal. The materials we study

are called *liquid crystals*. A more proper name for these systems is ‘mesomorphic phase’ (*mesomorphic*: intermediate form). The study of liquid crystals is so vast and so rich that we cannot possibly cover all aspects of it. In this chapter, we will only discuss those topics relevant to the experiments we performed, which is the light scattering problem applied to turbid samples of nematic liquid crystal.

To understand the nature of the order and symmetries of matter, we usually define quantities which can properly describe them. Let’s assume $\rho(\mathbf{r})$ is the density distribution function of the matter we are studying. We may define the density-density correlation function as

$$F(\mathbf{r} - \mathbf{r}') = \langle \rho(\mathbf{r})\rho(\mathbf{r}') \rangle, \quad (4.1)$$

where $\langle \dots \rangle$ means average over all space. Physically, $F(\mathbf{r} - \mathbf{r}')$ describes the probability that a constituent molecule is at \mathbf{r}' when another molecule is at \mathbf{r} . For a crystal, $F(\mathbf{r} - \mathbf{r}')$ is a periodic function. In an isotropic liquid, however, $F(\mathbf{r} - \mathbf{r}')$ is a function which decays to the square of the average number density $\bar{\rho}^2$ and is characterized by a length scale ξ . Typically, ξ is called correlation length. Liquid crystals, typically have no positional order, or positional order in one or two, rather than in three dimensions. For the case of no positional order, it is quite like a liquid. $F(\mathbf{r} - \mathbf{r}')$ is anisotropic, however, and there are at least two coherence lengths corresponding to two different directions over which correlations decay. This kind of liquid crystal is called *nematic liquid crystal*. Fig. 4.1 shows a schematic sketch of a nematic system. For the case with one-dimensional order in three dimensions, the system can be viewed as a set of two-dimensional liquid layers stacked on each other with a well defined spacing. This kind of liquid crystal is called *smectic liquid crystal*. For the case with two-dimensional order in three dimensions, the system can be viewed as a two-dimensional array of liquid columns. This kind of liquid crystal is called *columnar liquid crystal*. In the following discussions, we focus on nematic liquid crystals only, since it is the system studied in our experiment.

Besides the positional order, for non-spherical molecules, their degrees of freedom

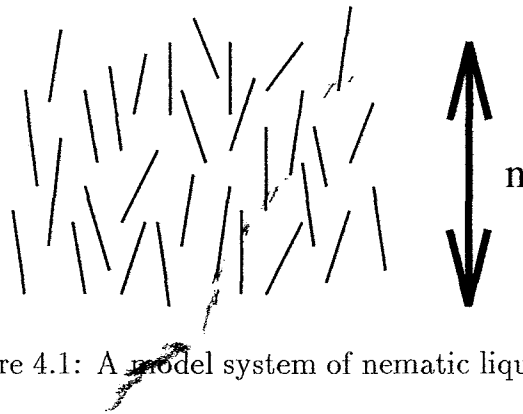


Figure 4.1: A model system of nematic liquid crystal

in orientation exhibit some interesting effects. If there is no directional order, the system is isotropic. Water is an example of this kind of system. For nematic liquid crystals, their constituent molecules are aligned preferentially along one direction. The correlations along this preferred direction typically are different from those in the perpendicular plane. In general, a nematic liquid crystal possesses the following features:

1. There is no *long-range order* with regard to the centers of gravity of the molecules. The correlations in position are similar to that of the conventional liquid except that the coherence length is not an isotropic quantity. As a matter of fact, nematic liquids do flow like liquids.

2. There is order in the direction of the molecules; these molecules tend to align along one preferred direction. The unit vector \mathbf{n} in this preferred direction is called the *director*. This directional order also effects to the optical properties of this system. In general, a nematic liquid crystal is a uniaxial medium with one major optical axis along \mathbf{n} .

3. We can not distinguish the state of director \mathbf{n} from the state of director $-\mathbf{n}$. This indistinguishability arises from the requirement of the stability of the system. For example, if the individual molecules carry a permanent electric dipole, to stabilize the whole system, the number of 'up' dipoles must equal the number of 'down' dipoles.

4. Nematic phases can only occur with materials which do not distinguish between left and right. Either the constituent molecule has to be identical to its mirror image or the material has to be composed of equal amounts of left- and right-handed species.

When a nematic crystal changes from the isotropic phase to the nematic phase, it decreases its symmetry and becomes more ordered. Quantitatively, we can define an order parameter that is ~~not~~ zero in the nematic phase but vanishes in the isotropic phase. The following arguments will lead to the selection of the order parameter for describing the nematic phase.

Let's first think about rigid rods. The rigid rod system is the simplest model system that gives rise to a nematic phase. In this model system, the distribution function of rod alignment is given by $f(\theta, \phi)$. The direction of the nematic axis \mathbf{n} is defined as the average direction of alignment of the rods and is taken as the z-axis of the (x, y, z) laboratory frame. The alignment distribution function has the following properties:

1. $f(\theta, \phi)$ is independent of ϕ . In other words, the phase has complete cylindrical symmetry about \mathbf{n} . In the following discussion, it will be simply noted as $f(\theta)$.

2. From the requirement of indistinguishability of \mathbf{n} and $-\mathbf{n}$, $f(\theta) = f(\pi - \theta)$.

Assuming that the axis of each rod is labeled by a unit vector \mathbf{a} where

$$\mathbf{a} \equiv (\sin \theta \cos \phi, \sin \theta \sin \phi, \cos \theta), \quad (4.2)$$

and each rod has complete cylindrical symmetry about \mathbf{a} . The first idea to characterize the alignment is the dipole term in the following sense,

$$\langle \cos \theta \rangle = \langle \mathbf{a} \cdot \mathbf{n} \rangle = \int f(\theta) \cos \theta d\Omega, \quad (4.3)$$

where the integration is over the whole solid angle. But this term vanishes as a result of property 2 mentioned above. We therefore must resort to higher order term for

the order parameter. The next multipole giving a non-trivial result is the quadrupole which is defined as

$$S = \frac{1}{2} \langle 3 \cos^2 \theta - 1 \rangle = \int f(\theta) \frac{1}{2} (3 \cos^2 \theta - 1) d\Omega. \quad (4.4)$$

Now, let's look at the following three instances:

1. If $f(\theta)$ is a δ function peaked at $\theta = 0$ or $\theta = \pi$, then $S = 1$.
2. If $f(\theta)$ is isotropic, then $S = 0$.
3. If $f(\theta)$ is a δ function peaked at $\theta = \pi/2$, then $S = -\frac{1}{2}$.

Typically, the quantity S can be extracted from NMR measurements by measuring the resonance line splitting which is proportional to S [40]. From the point of view of the experiment, the directional order is related to the measurement of all macroscopic tensor properties. For example, the relation between the applied magnetic field \mathbf{H} and the magnetic moment \mathbf{M} has the following form:

$$M_\alpha = \chi_{\alpha\beta} H_\beta \quad (4.5)$$

where $\alpha, \beta = x, y, z$. For a static field \mathbf{H} , $\chi_{\alpha\beta}$ is symmetric. In uniaxial nematic phase, $\chi_{\alpha\beta}$ can be diagonalized as

$$\chi_{\alpha\beta} = \begin{pmatrix} \chi_\perp & 0 & 0 \\ 0 & \chi_\perp & 0 \\ 0 & 0 & \chi_\parallel \end{pmatrix}. \quad (4.6)$$

If we define $Q_{\alpha\beta}$ as the anisotropic part of the magnetic susceptibility $\chi_{\alpha\beta}$, we find

$$Q_{\alpha\beta} = G \left(\chi_{\alpha\beta} - \frac{1}{3} \delta_{\alpha\beta} \sum_\gamma \chi_{\gamma\gamma} \right), \quad (4.7)$$

where G is a normalization constant which is usually chosen by setting $Q_{zz} = 1$ in a totally oriented system. $Q_{\alpha\beta}$ is called *tensor order parameter* and has the properties of being real, symmetric, and zero-trace. One remark to be made here is that choosing magnetic response as the starting point is just a matter of convention; we can use electric polarizability or the dielectric constant as well. The relation

between the dielectric constant and molecular properties, however, is much more obscure than that between magnetic susceptibility and molecular properties.

In general, for most situations of interest, the tensor order parameter of an ideal nematic liquid crystal with director \mathbf{n} has the following form

$$Q_{\alpha\beta} = \frac{1}{2} Q(T) (n_\alpha n_\beta - \frac{1}{3} \delta_{\alpha\beta}). \quad (4.8)$$

In most practical cases, due to the constraints imposed by the limiting boundaries and external fields, there will be some deformations of the director alignment. The director \mathbf{n} should be a function of \mathbf{r} and so is $Q_{\alpha\beta}$. While the length scale we are interested in is much larger than the molecular size, we can describe the deformations by a continuum theory which disregards the details of the structure of the molecules.

To study the distortion of the director field $\mathbf{n}(\mathbf{r})$, let's first try to construct the free energy associated with the distortion. There are several physical conditions we have to follow in constructing the distortion free energy. They are:

1. The distortion free energy F_d must be even in \mathbf{n} since \mathbf{n} cannot be distinguished from $-\mathbf{n}$.
2. The distortion free energy should be composed of terms of type of $\partial n_\beta / \partial x_\alpha$ (hereafter we will abbreviate it as $\partial_\alpha n_\beta$) which represents a general expression for the spatial variance in the director field.

According to these conditions, the simplest form of F_d should be a quadratic function of $\partial_\alpha n_\beta$. Here we will not go into the details of the derivation of F_d . The reader is encouraged to refer to de Gennes's book[40]. The final form of the distortion energy is given by

$$F_d = \frac{1}{2} K_1 (\nabla \cdot \mathbf{n})^2 + \frac{1}{2} K_2 (\mathbf{n} \cdot \nabla \times \mathbf{n})^2 + \frac{1}{2} K_3 (\mathbf{n} \times \nabla \times \mathbf{n})^2 \quad (4.9)$$

The constants K_i ($i = 1, 2, 3$) introduced in the above equation are associated with three basic types of deformations respectively. K_1 is for splay deformation, K_2 is for twist deformation, and K_3 is for bend deformation. These constants are of order 10^{-6} dyne. Fig. 4.2 gives a graphical representation of these deformations.

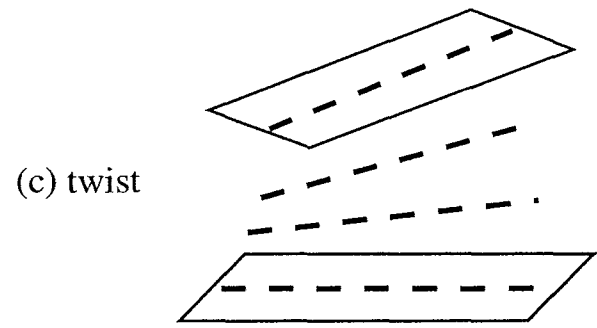
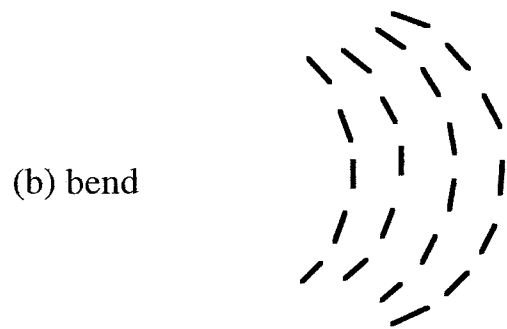
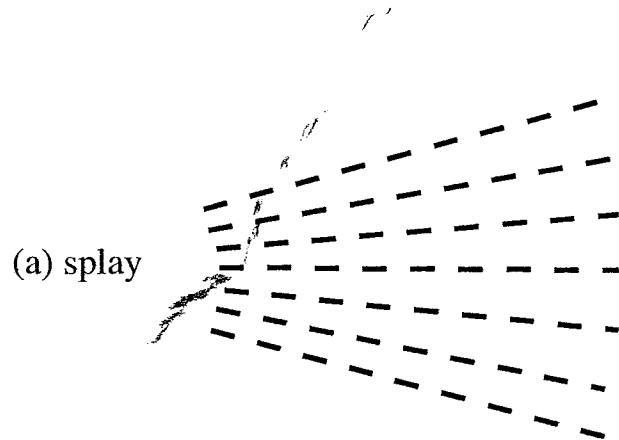


Figure 4.2: Three fundamental types of deformation

In thermal equilibrium, the total distortion energy $\mathcal{F}_d = \int F_d d\mathbf{r}$ should be a minimum with respect to all variations of the direction field $\mathbf{n}(\mathbf{r})$. In the language of variation principle, we have

$$\delta\mathcal{F}_d = \int \left\{ \frac{\partial F_d}{\partial n_\beta} \delta n_\beta + \frac{\partial F_d}{\partial \partial_\alpha n_\beta} \partial_\alpha (\delta n_\beta) \right\} d\mathbf{r} \quad (4.10)$$

After integrating the second term by parts and neglecting the surface terms, we arrive

$$\delta\mathcal{F}_d = \int \left\{ \frac{\partial F_d}{\partial n_\beta} - \partial_\alpha \left(\frac{\partial F_d}{\partial \partial_\alpha n_\beta} \right) \right\} (\delta n_\beta) d\mathbf{r} \quad (4.11)$$

We then can define the molecular field \mathbf{h} as

$$h_\beta \equiv -\frac{\partial F_d}{\partial n_\beta} + \partial_\alpha \left(\frac{\partial F_d}{\partial \partial_\alpha n_\beta} \right). \quad (4.12)$$

After inserting the expression for F_d we obtained above, we arrive at a rather complicated form for the molecular field which can be decomposed into three terms as

$$\begin{aligned} \mathbf{h}_S &= K_1 \nabla(\nabla \cdot \mathbf{n}) \\ \mathbf{h}_T &= -K_2 [(\mathbf{n} \cdot \nabla \times \mathbf{n}) \nabla \times \mathbf{n} + \nabla \times (\mathbf{n} \cdot \nabla \times \mathbf{n}) \mathbf{n}] \\ \mathbf{h}_B &= K_3 [(\mathbf{n} \times \nabla \times \mathbf{n}) \times \nabla \times \mathbf{n} + \nabla \times (\mathbf{n} \times \mathbf{n} \times \nabla \times \mathbf{n})] \end{aligned} \quad (4.13)$$

Since \mathbf{n} is an unit vector, it requires

$$\mathbf{n} \cdot \delta \mathbf{n} = 0. \quad (4.14)$$

This requirement leads to the conclusion that the molecular field \mathbf{h} should be in the direction of \mathbf{n} in equilibrium.

The fluctuations of the director field is the origin of the light scattering in nematic liquid crystals. We will discuss this point in next section.

4.2 Light Scattering in Nematic Liquid Crystal

By Comparison to the conventional isotropic liquids, the nematic liquid crystals scatter visible light $\sim 10^6$ more strongly, and are thus turbid in appearance when

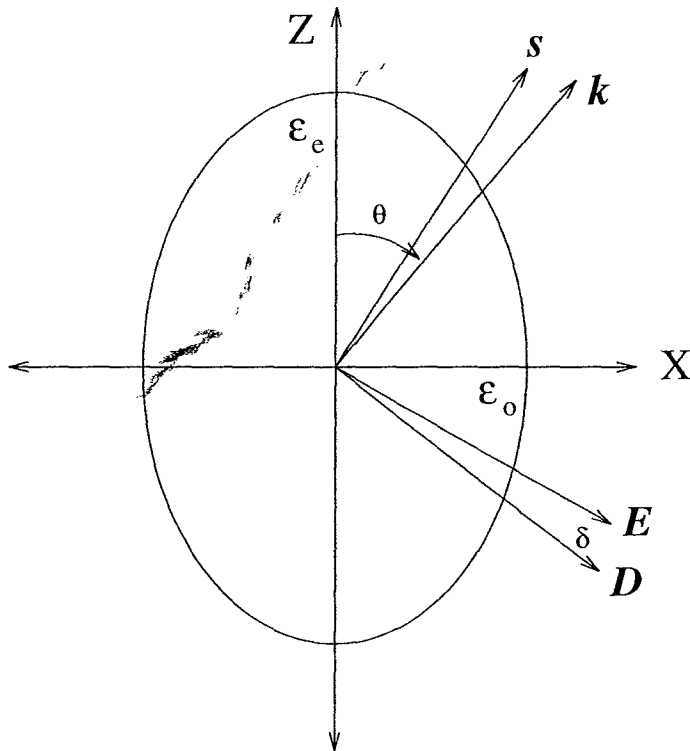


Figure 4.3: Light propagation in uniaxial medium: Light propagates with an angular dependent speed. Z-axis is the axis for the extraordinary refractive index

samples are of order a few mm thick. In the early years, this high scattering power of nematics made some scientists think that they were made of a suspension of small crystallites in a fluid phase with crystallite dimensions comparable to the wavelength of the visible light. In fact, the high scattering power of nematics is an intrinsic property of nematic phases. P. Chatelain[41] carried out the first detailed experimental studies in this field and gave us a very direct probe of the *spontaneous fluctuations of the alignment in a nematic liquid crystal*. One important optical property of nematic liquid crystals is that they are uniaxial crystals. Depending on its polarization, the incident light will propagate with the ‘ordinary’ refractive index n_o or ‘extraordinary’ index n_e . In the following, we will only briefly discuss this point. For further details, the readers are encouraged to refer to the papers written by Val’kov and Romanov[42]. Referring to Fig. 4.3, the extraordinary axis

(with refractive index n_e) is set to be the z-axis while the ordinary axis is set to be the x-axis (with refractive index n_o). An incident beam is characterized by a unit wave vector $\hat{\mathbf{k}} \equiv (\sin \theta \cos \phi, \sin \theta \sin \phi, \cos \theta)$ and polarization vector \mathbf{i} . If the polarization of this incident beam is perpendicular to the z-axis, the light propagates with the 'ordinary' refractive index n_o for all directions. On the other hand, if the polarization vector of this incident beam is in the plane composing of $\hat{\mathbf{k}}$ and $\hat{\mathbf{z}}$, the refractive index the light propagates with will have the following form:

$$\frac{1}{n_e(\theta)} = \sqrt{\frac{\cos^2 \theta}{n_o^2} + \frac{\sin^2 \theta}{n_e^2}}, \quad (4.15)$$

and the electric field \mathbf{E} will deviate from the electric displacement \mathbf{D} with an angle δ which is given by

$$\delta = \theta + \pi/2 - \tan^{-1} \left(\frac{\epsilon_e}{\epsilon_o} \tan(\theta + \pi/2) \right). \quad (4.16)$$

As a result, the Poynting vector \mathbf{S} deviates from the wave vector \mathbf{k} with the same angle δ given above. This polarization dependence of the refractive indices makes the scattering problem much more complicated, especially in the multiple scattering case.

Now, let's consider a nematic sample with its averaged director \mathbf{n}_0 parallel to z-axis. The fluctuations of director at point \mathbf{r} are described by small, non-zero components $\delta n_x(\mathbf{r})$ and $\delta n_y(\mathbf{r})$. Up to second order in δn_x and δn_y , the distortion energy becomes

$$\mathcal{F}_d = \frac{1}{2} \int \left\{ K_1 \left(\frac{\partial \delta n_x}{\partial x} + \frac{\partial \delta n_y}{\partial y} \right)^2 + K_2 \left(\frac{\partial \delta n_x}{\partial y} - \frac{\partial \delta n_y}{\partial x} \right)^2 + K_3 \left[\left(\frac{\partial \delta n_x}{\partial z} \right)^2 + \left(\frac{\partial \delta n_y}{\partial z} \right)^2 \right] \right\} d\mathbf{r} \quad (4.17)$$

For experimental consideration, we apply a magnetic field $H\hat{\mathbf{z}}$ and add the following term

$$\mathcal{F}_{mag} = \frac{1}{2} \int \chi_a H^2 (\delta n_x^2 + \delta n_y^2) d\mathbf{r} + \text{const.} \quad (4.18)$$

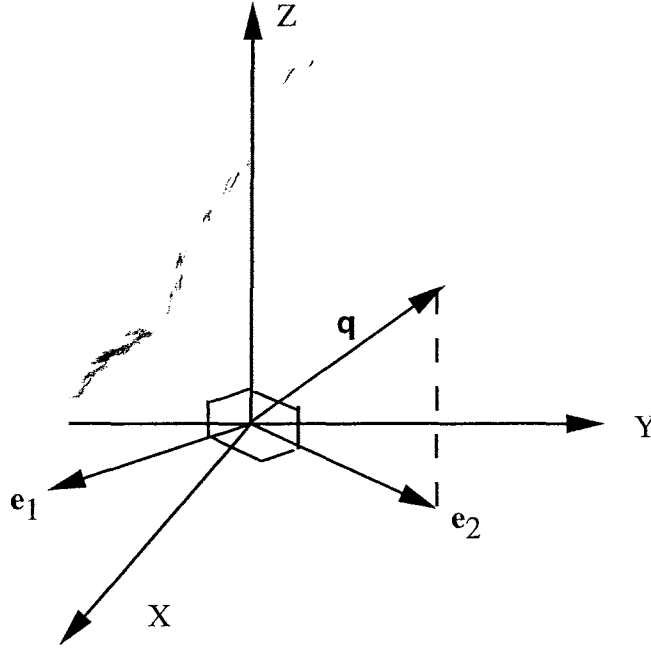


Figure 4.4: A new \mathbf{q} -dependent coordinates system: \mathbf{e}_1 is perpendicular to both $\hat{\mathbf{z}}$ and \mathbf{q} and \mathbf{e}_2 is perpendicular to both $\hat{\mathbf{z}}$ and \mathbf{e}_1 .

to the free energy. To link this problem to light scattering, however, we should Fourier transform $\delta n_x(\mathbf{r})$ and $\delta n_y(\mathbf{r})$ which are defined by

$$\delta n_j(\mathbf{q}) = \int \delta n_j(\mathbf{r}) e^{i\mathbf{q}\cdot\mathbf{r}} d\mathbf{r} \quad (j = x, y). \quad (4.19)$$

The free energy then becomes

$$\mathcal{F} = \mathcal{F}_o + \frac{1}{2}\Omega^{-1} \sum_q \left\{ K_1 |\delta n_x(\mathbf{q})q_x + \delta n_y(\mathbf{q})q_y|^2 + K_2 |\delta n_x(\mathbf{q})q_y - \delta n_y(\mathbf{q})q_x|^2 + (K_3 q_z^2 + \chi_a H^2) (|\delta n_x(\mathbf{q})|^2 + |\delta n_y(\mathbf{q})|^2) \right\}, \quad (4.20)$$

where \mathcal{F}_o represents some internal free energy and Ω is the sample volume. We may simplify the above expression by choosing a new coordinate system. As shown in Fig. 4.4, \mathbf{e}_1 and \mathbf{e}_2 are unit vectors in (xy) plane: \mathbf{e}_2 is normal to \mathbf{q} while \mathbf{e}_1 is normal to \mathbf{e}_2 . $\delta n_\alpha(\mathbf{q})$ describes the component of $\delta n_\alpha(\mathbf{q})$ along \mathbf{e}_α ($\alpha = 1, 2$).

Physically, $\delta n_1(\mathbf{q})$ describes a periodic distortion combining splay and bend while

$\delta n_2(\mathbf{q})$ describes a periodic distortion combining twist and bend. In this new coordinates system, the free energy takes a simple form, i.e.

$$\mathcal{F} = \mathcal{F}_o + \frac{1}{2}\Omega^{-1} \sum_q \sum_{\alpha=1,2'} |\delta n_\alpha(\mathbf{q})|^2 (K_3 q_{\parallel}^2 + K_\alpha q_{\perp}^2 + \chi_\alpha H^2). \quad (4.21)$$

Here $q_{\parallel} = q_z$ is the component of the wavevector parallel to the optical axis, while $\mathbf{q}_{\perp} = \mathbf{q} \cdot \mathbf{e}_1$ is the normal component. At thermal equilibrium for a classical system, we may apply the equipartition theorem to the free energy quadratic in the fluctuation amplitudes $\delta n_\alpha(\mathbf{q})$, i.e.

$$\left\langle \frac{1}{2}\Omega^{-1} |\delta n_\alpha(\mathbf{q})|^2 (K_3 q_{\parallel}^2 + K_\alpha q_{\perp}^2 + \chi_\alpha H^2) \right\rangle = \frac{1}{2} k_B T \quad (4.22)$$

or

$$\langle |\delta n_\alpha(\mathbf{q})|^2 \rangle = (\Omega k_B T) / (K_3 q_{\parallel}^2 + K_\alpha q_{\perp}^2 + \chi_\alpha H^2), \quad (4.23)$$

where the bracket $\langle \dots \rangle$ denotes a thermal average. As a general practice in investigating fluctuation phenomenon, we would like to know the correlations of the director \mathbf{n} at two different positions \mathbf{r}_1 and \mathbf{r}_2 . From the theorem of Fourier transform, we have

$$\langle \delta n_x(\mathbf{r}_1) \delta n_x(\mathbf{r}_2) \rangle = \Omega^{-2} \sum_{\mathbf{q}, \mathbf{q}'} \langle \delta n_x(\mathbf{q}) \delta n_x(-\mathbf{q}') \rangle e^{-i(\mathbf{q} \cdot \mathbf{r}_1 - \mathbf{q}' \cdot \mathbf{r}_2)}. \quad (4.24)$$

When $\mathbf{q} \neq \mathbf{q}'$, the Fourier components of $\mathbf{n}(\mathbf{q})$ and $\mathbf{n}(\mathbf{q}')$ are uncorrelated. Therefore we have

$$\langle \delta n_x(\mathbf{r}_1) \delta n_x(\mathbf{r}_2) \rangle = \Omega^{-2} \sum_{\mathbf{q}} \langle |\delta n_x(\mathbf{q})|^2 \rangle e^{-i\mathbf{q} \cdot \mathbf{R}}, \quad (4.25)$$

where $\mathbf{R} = \mathbf{r}_2 - \mathbf{r}_1$. As we transform $\delta n_x(\mathbf{q})$ to $\delta n_\alpha(\mathbf{q})$ and use the equipartition formula we obtained above, we obtain a general result which relates measurable physical quantities, such as temperature and magnetic field to eqn. 4.25. The calculation, however is very tedious and will not be presented here. Instead, let's look at a simple case where all the elastic constant K 's are equal. Then we have, after some calculations,

$$\langle \delta n_x(\mathbf{r}_1) \delta n_x(\mathbf{r}_2) \rangle = \langle \delta n_y(\mathbf{r}_1) \delta n_y(\mathbf{r}_2) \rangle = \frac{k_B T}{4\pi K R} e^{-R/\xi}, \quad (4.26)$$

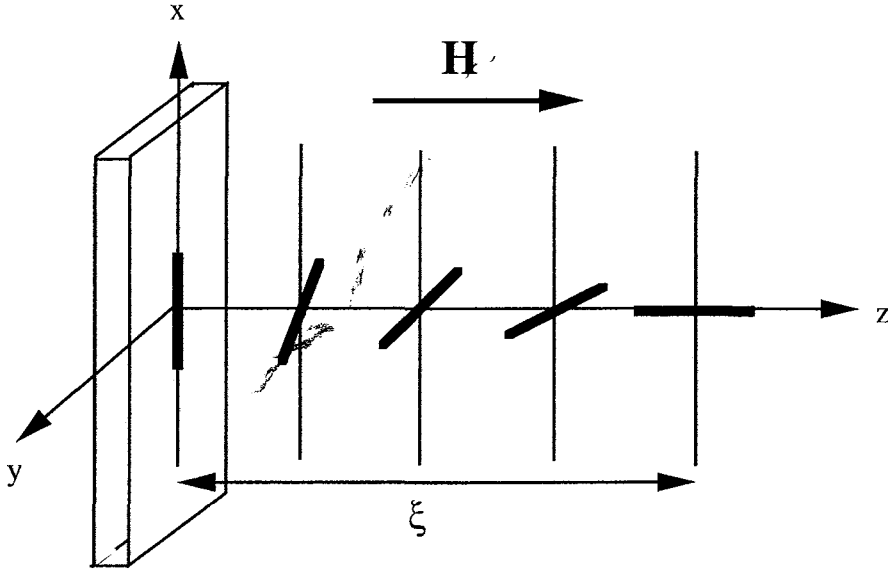


Figure 4.5: Magnetic coherence length

where

$$\xi = \sqrt{\frac{K}{\chi_a}} \frac{1}{H} \quad (4.27)$$

is called the *magnetic coherence length*. The magnetic coherence length ξ characterizes the length scale over which a fluctuation in director will remain correlated. On the other hand, as sketched in Fig. 4.5, one can prove that the magnetic coherence length ξ also represents the length scale of the transition region to turn the local director field into the direction of magnetic field. This equivalence arises from the fundamental relation between fluctuation and dissipation.

Next, let's discuss the light scattering caused by the orientational fluctuations of the director. The fluctuations of ϵ comes from two sources. One is the fluctuations in the magnitude of ϵ_{\parallel} and ϵ_{\perp} . This could be due to the changes in the density, temperature, etc. The other is the fluctuation in the orientation of the director \mathbf{n} . In the case of nematic liquid crystals in thermal equilibrium, the latter effect is the dominant. In the following discussion, we will derive a formula for the scattering cross-section in the nematic liquid crystal. In principle, the scattering can be treated as radiation from an induced dipole. Assuming we have a dipole $\mathbf{P}(\mathbf{r})e^{-i\omega t}$ located at

position \mathbf{r} , in the far-field approximation, at a remote position \mathbf{r}' , we should detect the electric field

$$\mathbf{E}(\mathbf{r}') = (\omega^2/c^2 R) \mathbf{P}_R(\mathbf{r}) e^{i(kR - \omega t)} \quad (4.28)$$

where $\mathbf{R} = \mathbf{r}' - \mathbf{r}$, $\mathbf{P}_R(\mathbf{r})$ is the component of \mathbf{P} normal to \mathbf{R} , and $k = n\omega/c$. If the incoming radiation field is $\mathbf{E}_{in}(\mathbf{r}) = E_o \mathbf{i} \exp(i\mathbf{k}_o \cdot \mathbf{r})$ where \mathbf{i} is the unit vector in the polarization direction, then the explicit form of the induced dipole is

$$\mathbf{P}(\mathbf{r}) = \frac{E_o}{4\pi} (\epsilon(\mathbf{r}) - 1) \mathbf{i} \exp(i\mathbf{k}_o \cdot \mathbf{r}). \quad (4.29)$$

When the sample has a finite volume, we have to sum over all the contributions of the sample to obtain the outgoing field $\mathbf{E}_{out}(\mathbf{r}')$. In the continuum limit, the summation is replaced by the integral given below:

$$\mathbf{E}_{out}(\mathbf{r}') = \frac{E_o \omega^2}{4\pi c^2 R} \int_{\Omega} (\epsilon(\mathbf{r}) - 1) \cdot \mathbf{i} e^{i\mathbf{q} \cdot \mathbf{r}} d\mathbf{r}, \quad (4.30)$$

where $\mathbf{q} = \mathbf{k} - \mathbf{k}_o$ is the scattering vector and \mathbf{k} is the wavevector of the outgoing radiation field. Note that for $\mathbf{q} \neq \mathbf{0}$, the unit tensor term $\mathbf{1}$ contributes nothing to the integral for a sample with dimension much larger than the wavelength of radiation field. We can then rewrite \mathbf{E}_{out} as

$$\mathbf{E}_{out}(\mathbf{r}') = \frac{E_o \omega^2}{4\pi c^2 R} e^{i\mathbf{k} \cdot \mathbf{r}'} \epsilon(\mathbf{q}) \cdot \mathbf{i}, \quad (4.31)$$

where

$$\epsilon(\mathbf{q}) = \int \epsilon(\mathbf{r}) e^{i\mathbf{q} \cdot \mathbf{r}} d\mathbf{r}. \quad (4.32)$$

Experimentally, we must specify a final polarization direction for detection. Then, it is necessary to consider the projection of \mathbf{E}_{out} in the selected final polarization direction \mathbf{f} . We arrive at

$$\mathbf{f} \cdot \mathbf{E}_{out}(\mathbf{r}') = \frac{E_o \omega^2}{4\pi c^2 R} e^{i\mathbf{k} \cdot \mathbf{r}'} \mathbf{f} \cdot \epsilon(\mathbf{q}) \cdot \mathbf{i}. \quad (4.33)$$

Here we define the scattering amplitude

$$\alpha = \left(\frac{\omega^2}{4\pi c^2} \right) \mathbf{f} \cdot \epsilon(\mathbf{q}) \cdot \mathbf{i}. \quad (4.34)$$

The differential cross-section is then

$$\frac{d\sigma}{d\Omega} = \langle |\alpha|^2 \rangle, \quad (4.35)$$

where $\langle \dots \rangle$ represents a thermal average. Now, let's consider the case when there are fluctuations in ϵ , caused by the orientationa fluctuations of the director \mathbf{n} by an amount $\delta\mathbf{n} = (\delta n_x, \delta n_y, 0)$. We first write down the expression for the dielectric tensor as

$$\epsilon_{\alpha\beta} = \epsilon_{\perp} \delta_{\alpha\beta} + \epsilon_a n_{\alpha} n_{\beta}, \quad (4.36)$$

where $\epsilon_a \equiv (\epsilon_{\parallel} - \epsilon_{\perp})$. Note that n_{α} in the above expression is the component of the director itself. To the first order in $\delta\mathbf{n}$, we get

$$\mathbf{f} \cdot \epsilon \cdot \mathbf{i} = \mathbf{f} \cdot \langle \epsilon \rangle + \epsilon_a [(\mathbf{f} \cdot \delta\mathbf{n})(\mathbf{n}_o \cdot \mathbf{i}) + (\mathbf{f} \cdot \mathbf{n}_o)(\delta\mathbf{n} \cdot \mathbf{i})], \quad (4.37)$$

where \mathbf{n}_o is the unit vector of the averaged director and is usually chosen parallel to \hat{z} . Recalling the Fourier transform of the orientation distribution of director in previous discussion,

$$\delta\mathbf{n}(\mathbf{q}) = \mathbf{e}_1 \delta n_1(\mathbf{q}) + \mathbf{e}_2 \delta n_2(\mathbf{q}), \quad (4.38)$$

we can then replace $\epsilon(\mathbf{q})$ by $n_{\alpha}(\mathbf{q})$ in the expression of $d\sigma/d\Omega$ and arrive at

$$\frac{d\sigma}{d\Omega} = (\epsilon_a \omega^2 / 4\pi c^2)^2 \sum_{\alpha=1,2} \langle |\delta n_{\alpha}(\mathbf{q})|^2 \rangle (i_{\alpha} f_z + i_z f_{\alpha})^2, \quad (4.39)$$

where $i_{\alpha} = \mathbf{e}_{\alpha} \cdot \mathbf{i}$ and $i_z = \hat{z} \cdot \mathbf{i}$, etc. Furthermore, equipartition theorem enables us to derive the final formula for the differential cross-section as the following

$$\frac{d\sigma}{d\Omega} = (\epsilon_a \omega^2 / 4\pi c^2)^2 \sum_{\alpha=1,2} \frac{k_B T (i_{\alpha} f_z + i_z f_{\alpha})^2}{K_3 q_{\parallel}^2 + K_{\alpha} q_{\perp}^2 + \chi_a H^2}. \quad (4.40)$$

From the above equation, we see that it is impossible for an incoming 'ordinary' mode photon ($i_z = 0$) to scatter into the 'ordinary' mode ($f_z = 0$). On the other hand, as $H = 0$, there is very large cross-section around the incident direction. Eqn. 4.40, however, is not precisely correct since it does not take the propagation mode into consideration. In a more detailed treatment[42, 43], it is proved that

$$\frac{d\sigma}{d\Omega} = (\epsilon_a \omega^2 / 4\pi c^2)^2 \frac{n_f}{n_i \cos \delta_i} \sum_{\alpha=1,2} \frac{k_B T (i_{\alpha} f_z + i_z f_{\alpha})^2}{K_3 q_{\parallel}^2 + K_{\alpha} q_{\perp}^2 + \chi_a H^2}. \quad (4.41)$$

Depending on the magnitude of the external magnetic field, the scattering may be highly forward peaked. Fig. 4.6 shows the differential cross sections of three scattering configurations for 5CB (also known as K15) nematic liquid with $\xi = 10\mu m$.

4.3 Dynamics of the Director Field

The fluctuations in the director are not static. The dynamical character of the director fluctuation was first observed by Friedel, Grandjean, and Mauguin as “flicker effects”. Under thermal equilibrium, we can imagine, a director \mathbf{n} will relax towards its average orientation \mathbf{n}_o in a certain time. The change in the alignment, in many instances, can induce a flow in nematic. The coupling between orientation and flow is a very complicated and delicate problem. It has been analyzed essentially by two groups who used very different approaches. Ericksen, Leslie, and Parodi used a macroscopic approach based on classical mechanics (ELP approach)[44, 45, 46] while the Harvard group took a microscopic approach based on the study of correlation functions[47]. The ELP approach first assumes that in a nematic liquid crystal, a dynamical state must be specified by two vector fields which are:

1. a velocity field $\mathbf{v}(\mathbf{r})$ giving the flow of matter, and
2. a unit vector $\mathbf{n}(\mathbf{r})$ (the director) describing the local alignment.

Due to the friction processes in the fluid, we have to derive a formula giving the dissipation or the entropy source. For simplicity, we shall restrict our discussion to isothermal processes which only involve two dissipative losses. One type of the loss is caused by the conventional viscosity effects. The other one is the loss associated with a rotation of the director with respect to the background fluid. Following the approach of de Groot and Mazur, we have the dissipation $T\dot{S}$ equal to the change in the stored free energy

$$T\dot{S} = -\frac{d}{dt} \int \left\{ \frac{1}{2} \rho v^2 + F_o + F_d + F_m \right\} d^3\mathbf{r}. \quad (4.42)$$

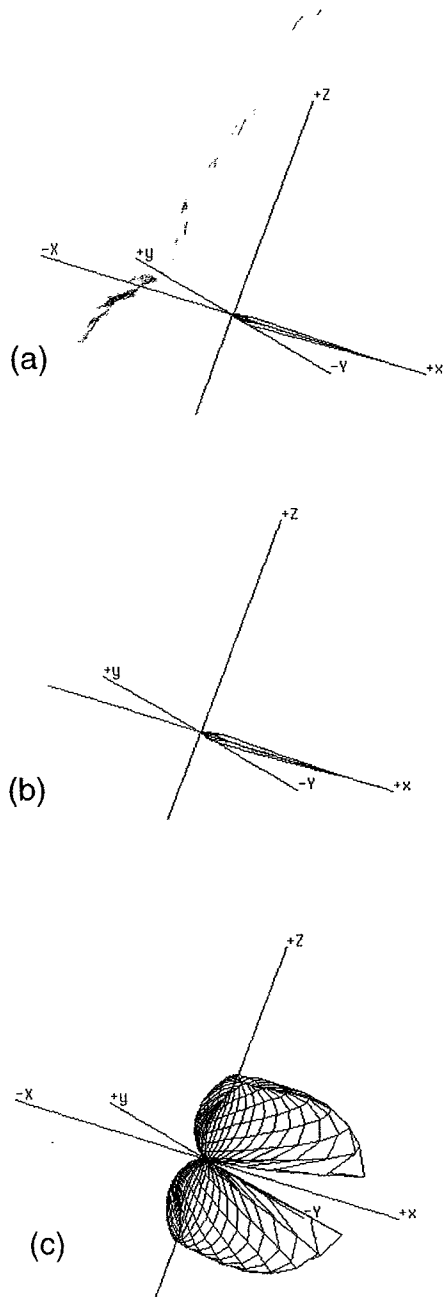


Figure 4.6: Differential cross-sections for K15 nematic liquid with $\xi = 10\mu m$: The incident direction(+ x -axis) is perpendicular to the direction direction(z -axis). (a) ordinary mode photon scattered into extraordinary mode photon. (b) extraordinary mode photon scattered into ordinary mode photon. (c) extraordinary mode photon scattered into extraordinary mode photon.

The first term in the integral is the kinetic energy with ρ representing density. F_o is the internal free energy which depends on the density. F_d is the distortion free energy. F_m is the free energy of the coupling between the external magnetic field and the director. From the equation of motion

$$\rho \frac{d}{dt} v_\beta = \partial_\alpha \sigma_{\alpha\beta}, \quad (4.43)$$

where $\sigma_{\alpha\beta}$ is the stress tensor. The change in the kinetic energy can be expressed as

$$-\frac{d}{dt} \int \left(\frac{1}{2} \rho v^2 \right) d^3 \mathbf{r} = \int \sigma_{\alpha\beta} \partial_\alpha v_\beta d^3 \mathbf{r} + \text{surface terms.} \quad (4.44)$$

The contribution from $F_o + F_d + F_m$ can be proved to be

$$\frac{d}{dt} \int \{F_o + F_d + F_m\} d^3 \mathbf{r} = \int (\sigma_{\alpha\beta}^e \partial_\alpha v_\beta + \mathbf{h} \cdot \dot{\mathbf{n}}) d^3 \mathbf{r} + \text{surface terms.} \quad (4.45)$$

$\sigma_{\alpha\beta}^e$ in the above expression is called *Ericksen stress* which is defined as

$$\sigma_{\alpha\beta}^e = -\frac{\delta F_d}{\delta(\partial_\beta n_\gamma)} \partial_\alpha n_\gamma + (F_d + F_m + F_g) \delta_{\alpha\beta}. \quad (4.46)$$

Adding up all the contributions, we have

$$T\dot{S} = \int \{(\sigma_{\alpha\beta} - \sigma_{\alpha\beta}^e) \partial_\alpha v_\beta + \mathbf{h} \cdot \dot{\mathbf{n}}\} d^3 \mathbf{r} + \text{surface terms.} \quad (4.47)$$

The difference between the actual stress and Ericksen stress is called the *viscous stress*

$$\sigma'_{\alpha\beta} = \sigma_{\alpha\beta} - \sigma_{\alpha\beta}^e. \quad (4.48)$$

Generally, $\sigma'_{\alpha\beta}$ is not symmetric. It can be proved that $T\dot{S}$ can be written as the sum of a symmetric part and an asymmetric part. Namely,

$$T\dot{S} = \int \{\mathbf{A} : \boldsymbol{\sigma}^s + \mathbf{h} \cdot \mathbf{N}\} d^3 \mathbf{r}, \quad (4.49)$$

where

$$\begin{aligned} A_{\alpha\beta} &= \frac{1}{2} (\partial_\alpha v_\beta + \partial_\beta v_\alpha), \\ \boldsymbol{\omega} &= \frac{1}{2} \nabla \times \mathbf{v}, \\ \mathbf{N} &= \dot{\mathbf{n}} - \boldsymbol{\omega} \times \mathbf{n}, \end{aligned} \quad (4.50)$$

and σ^s is the symmetric part of σ .

For an incompressible nematic liquid crystal, the trace of \mathbf{A} vanishes. We have

$$\begin{aligned} \sigma'_{\alpha\beta} = & \alpha_1 n_\alpha n_\beta n_\mu n_\rho A_{\mu\rho} + \alpha_4 A_{\alpha\beta} + \alpha_5 n_\alpha \mu A_{\mu\beta} \\ & + \alpha_6 n_\beta \mu A_{\mu\alpha} + \alpha_2 n_\alpha N_\beta + \alpha_3 n_\beta N_\alpha, \end{aligned} \quad (4.51)$$

and

$$h_\mu = \gamma_1 N_\mu + \gamma_2 n_\alpha A_{\alpha\mu}, \quad (4.52)$$

where

$$\begin{aligned} \gamma_1 &= \alpha_3 - \alpha_2, \\ \gamma_2 &= \alpha_2 + \alpha_3 = \alpha_6 - \alpha_5. \end{aligned} \quad (4.53)$$

These coefficients α_i are called *Leslie coefficients*. Now let's consider the laminar flow under the magnetic fields. As shown in Fig. 4.7, there are three fundamental geometries for viscosity measurements in a well aligned nematic, which are (a) director perpendicular to both flow velocity and gradient of flow velocity, (b) director parallel to flow velocity but perpendicular gradient of flow velocity, and (c) director parallel to gradient of flow velocity but perpendicular to flow velocity. Miesowicz has measured the corresponding viscosities η_a, η_b , and η_c . There are relations that exist between the Miesowicz viscosity coefficients and Leslie viscosity coefficients. It can be proved that

$$\begin{aligned} \eta_a &= \frac{1}{2}\alpha_4 \\ \eta_b &= \frac{1}{2}(\alpha_2 + \alpha_4 + \alpha_6) \\ \eta_c &= \frac{1}{2}(-\alpha_2 + \alpha_4 + \alpha_5). \end{aligned} \quad (4.54)$$

With the understanding of the viscous losses discussed above, now we can discuss the fluctuation relaxation in a more quantitative way. A fluctuation $\delta n_\alpha(\mathbf{q})$ will experience a restoring 'force' which is given by

$$f_\alpha = -(K_\alpha q_\perp^2 + K_3 q_z^2 + \chi_a H^2) \delta n_\alpha = -K_\alpha(\mathbf{q}) \delta n_\alpha \quad (\alpha = 1, 2). \quad (4.55)$$

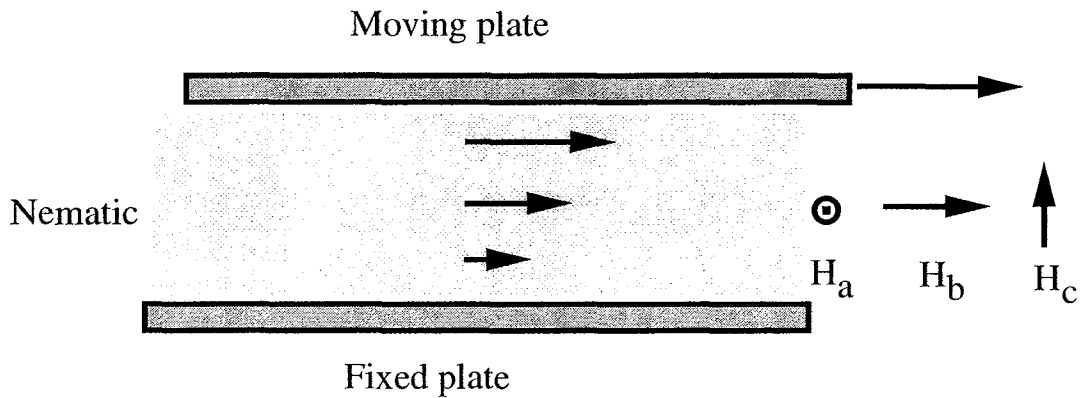
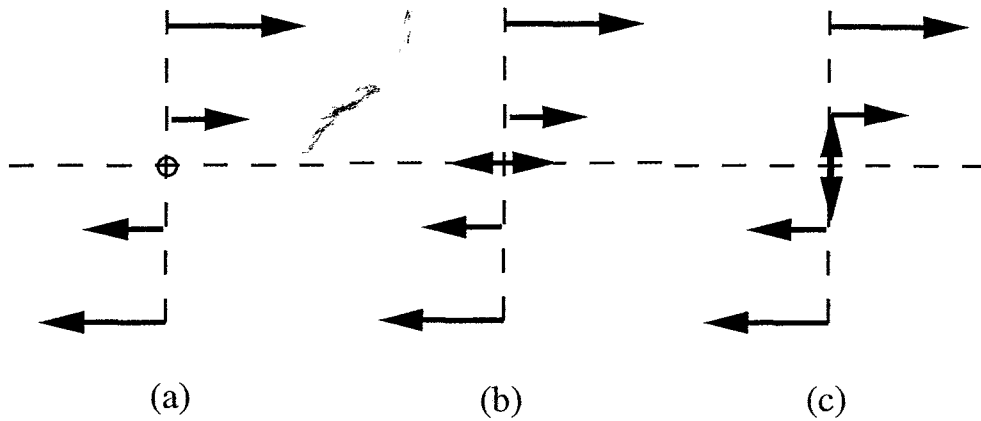


Figure 4.7: Three fundamental geometries for viscosity measurements: (a) director perpendicular to both flow velocity and gradient of flow velocity, (b) director parallel to flow velocity but perpendicular gradient of flow velocity, and (c) director parallel to gradient of flow velocity but perpendicular to flow velocity.

We can write down the relaxation equation for the fluctuation $\delta n_\alpha(\mathbf{q})$ as

$$\frac{\partial}{\partial t} \delta n_\alpha(\mathbf{q}) = -\frac{1}{\tau_\alpha(\mathbf{q})} \delta n_\alpha(\mathbf{q}), \quad (4.56)$$

where

$$\frac{1}{\tau_\alpha(\mathbf{q})} = \frac{K_\alpha(\mathbf{q})}{\eta_\alpha(\mathbf{q})}. \quad (4.57)$$

The viscosity $\eta_\alpha(\mathbf{q})$ is given explicitly by

$$\eta_1(\mathbf{q}) = \gamma_1 - \frac{(q_\perp^2 \alpha_3 - q_z^2 \alpha_2)^2}{q_\perp^4 \eta_b + q_\perp^2 q_z^2 (\alpha_1 + \alpha_3 + \alpha_4 + \alpha_5) + q_z^4 \eta_c}, \quad (4.58)$$

$$\eta_2(\mathbf{q}) = \gamma_1 - \frac{\alpha_2^2 q_z^2}{q_\perp^2 \eta_\alpha + q_z^2 \eta_c}. \quad (4.59)$$

$K_\alpha(\mathbf{q})$ is given by

$$K_\alpha(\mathbf{q}) = K_3 q_{\parallel}^2 + K_\alpha q_\perp^2 + \chi_\alpha H^2. \quad (4.60)$$

Now, let's consider the quantity $\langle g_1(\mathbf{q}, \tau) \rangle$. First, we write down the expression of $E(\mathbf{q}, \tau = 0)E^*(\mathbf{q}, \tau)$ as

$$E(\mathbf{q}, \tau = 0)E^*(\mathbf{q}, \tau) \propto \sum_{\alpha=1,2} \frac{k_B T (i_\alpha f_z + i_z f_\alpha)^2}{K_\alpha(\mathbf{q})} \exp\left(-\frac{K_\alpha(\mathbf{q})}{\eta_\alpha(\mathbf{q})} \tau\right). \quad (4.61)$$

In the limit where $\frac{K_\alpha(\mathbf{q})}{\eta_\alpha(\mathbf{q})} \tau$ is much smaller than 1, we may rewrite the above equation as

$$\langle E(\mathbf{q}, \tau = 0)E^*(\mathbf{q}, \tau) \rangle \propto \left\langle \sum_{\alpha=1,2} \frac{k_B T (i_\alpha f_z + i_z f_\alpha)^2}{K_\alpha(\mathbf{q})} \left(1 - \frac{K_\alpha(\mathbf{q})}{\eta_\alpha(\mathbf{q})} \tau\right) \right\rangle. \quad (4.62)$$

Expanding the right-hand side of the above equation and take τ out of the average, we obtain

$$\langle E(\mathbf{q}, \tau = 0)E^*(\mathbf{q}, \tau) \rangle \propto \left\langle \sum_{\alpha=1,2} \frac{k_B T (i_\alpha f_z + i_z f_\alpha)^2}{K_\alpha(\mathbf{q})} \right\rangle - \left\langle \sum_{\alpha=1,2} \frac{k_B T (i_\alpha f_z + i_z f_\alpha)^2}{\eta_\alpha(\mathbf{q})} \right\rangle \tau. \quad (4.63)$$

We can furthermore write the above equation as

$$\langle E(\mathbf{q}, \tau = 0)E^*(\mathbf{q}, \tau) \rangle \propto \frac{1}{K'} \left(1 - \frac{K'}{\eta'} \tau\right), \quad (4.64)$$

where

$$\begin{aligned}\frac{1}{\eta'} &= \left\langle \sum_{\alpha=1,2} \frac{(i_{\alpha} f_z + i_z f_{\alpha})^2}{\eta_{\alpha}(\mathbf{q})} \right\rangle \\ \frac{1}{K'} &= \left\langle \sum_{\alpha=1,2} \frac{(i_{\alpha} f_z + i_z f_{\alpha})^2}{K_{\alpha}(\mathbf{q})} \right\rangle.\end{aligned}\quad (4.65)$$

Here the average has to be carried out is integration over $\Omega_{\mathbf{k}}$ and $\Omega_{\mathbf{k}'}$ and summing over all polarization eigenmodes since $\langle E(\mathbf{q}, \tau = 0)E^*(\mathbf{q}, \tau) \rangle$ already carries the weighting factor. Again, we can use the approximation $e^{-x} \sim 1 - x$, and obtain

$$\langle E(\mathbf{q}, \tau = 0)E^*(\mathbf{q}, \tau) \rangle \propto \frac{1}{K'} \exp\left(-\frac{K'}{\eta'}\tau\right), \quad (4.66)$$

In fact, $1/K'$ is the proportional to $\langle |E(\mathbf{q})|^2 \rangle$, and we then arrive at

$$\langle g_1(\mathbf{q}, \tau) \rangle = \exp\left(-\frac{K'}{\eta'}\tau\right), \quad (4.67)$$

Now, we would like to consider $g_1(\tau)$ in the multiple scattering case. As in the colloids case, we might have

$$g_1(\tau) = \int_0^{\infty} ds P(s) \left[\exp\left(-\frac{K'}{\eta'}\tau\right) \right]^{s/\bar{l}}, \quad (4.68)$$

where $P(s)$ now depends on both D_{\parallel} and D_{\perp} and \bar{l} is the averaged mean free path. The value of \bar{l} should be an average value over all possible \mathbf{k}_{in} . This formulation is not, however, suitable to the case of nematics since photons travel in different speeds in different directions if they are in extraordinary mode. Besides, $P(s)$ is not a directly measurable quantity. In experiment, it's $P(t)$ that we can measure. We should rewrite eqn.4.69 in the following form of

$$g_1(\tau) = \int_0^{\infty} dt P(t) \left[\exp\left(-\frac{K'}{\eta'}\tau\right) \right]^{t/\langle t \rangle}, \quad (4.69)$$

$\langle t \rangle = \langle n(\mathbf{k}_i, \mathbf{i})l(\mathbf{k}_i, \mathbf{i}) \rangle_{\mathbf{k}_i, \mathbf{i}/c}$ is the average time between scattering events in the sample. Here $n(\mathbf{k}_i, \mathbf{i})$ and $l(\mathbf{k}_i, \mathbf{i})$ are the index of refraction and mean free path for a photon traveling with wave vector \mathbf{k}_i and polarization \mathbf{i} respectively. After carrying out the appropriate average, it can be proved that[18]

$$g_1(\tau) = \int_0^{\infty} dt P(t) \exp\left(-A \frac{\tau t}{\gamma_{eff}}\right), \quad (4.70)$$

where

$$A = \frac{2}{9\pi} \frac{\omega^4 k_B T \Delta \epsilon^2}{c^3 \epsilon_{\perp}^{1/2}}. \quad (4.71)$$

In Eq. 4.70, we find that the photon diffusion only effects $P(t)$. This is different from the case in isotropic colloidal suspensions where the photon random walk step appears in the dynamical decay rate as well as in $P(t)$. Physically, this arises from the fact that light scattering process in liquid crystals is the same process that effects the dynamics of the system, whereas in colloids light scattering does not depend on the dynamics of the system. If we are able to obtain $P(t)$, we then can independently obtain the dynamical information of the system via determining the effective rotational viscosity γ_{eff} .

4.4 Computer Simulation

Generally, the multiple light scattering problem is a very complicated problem. Only in the case of strong multiple scattering in random media, can we apply the photon diffusion approximation to simplify the problem. One might ask, if it is possible to apply the photon diffusion approximation to anisotropic media, such as nematic liquid crystal? To answer this question, of course, the final resort is doing experiment. We may, however, obtain some insights of this problem by means of computer simulation. In this section, we will discuss the principles we applied in the computer simulation and present some simulation results. In Appendix A, the source code of the simulation is also presented.

If we imagine that a photon with Poynting vector \mathbf{S}_{in} and polarization \mathbf{i} propagates from vacuum into a nematic liquid crystal with its director along the z -axis, the survival probability of this photon to travel a distance r without been scattered in the nematic liquid crystal is given by

$$P_{\mathbf{s}_{in}}(r) = \exp[-\sigma(\mathbf{S}_{in}, \mathbf{i})r], \quad (4.72)$$

where $\sigma(\mathbf{S}_{in}, \mathbf{i})$ is the total cross-section and is defined as

$$\sigma_o = \sigma_{oe} + \sigma_{oo} = \sigma_{oe} = \int_{\Omega} \frac{d\sigma_{oe}}{d\Omega} d\Omega, \quad (4.73)$$

and

$$\sigma_e = \sigma_{ee} + \sigma_{eo} = \int_{\Omega} \left(\frac{d\sigma_{ee}}{d\Omega} + \frac{d\sigma_{eo}}{d\Omega} \right) d\Omega. \quad (4.74)$$

Here the notation (oe) indicates that the photon is been scattered from the ‘ordinary’ mode into ‘extraordinary’ mode. Note that in nematics, the Poynting vector \mathbf{S} is not always in the same direction as the wave vector \mathbf{k} . Since the direction of the Poynting vector is also the energy propagation direction, we should use \mathbf{S} as the photon propagation direction in the computer simulation. In most cases, however, the calculation of scattering related quantities are based on the incident wave vector \mathbf{k}_i and scattered wave vector \mathbf{k}_f . In the simulation, for a given \mathbf{S}_i , we have to obtain its associated \mathbf{k}_i and use it to obtain the survival probability. As the photon is determined to be scattered, we have to use \mathbf{k}_f to obtain \mathbf{S}_f . In the simulation, we let the photon propagate in a given direction with a given polarization under a given time step. The time step, of course, has to be much smaller than the time required for the photon to travel a distance of $1/\sigma$. At each step, we use a random number generator to produce a random number and compare it with the associated survival probability P_s . Note that P_s is not the survival probability given in eqn. 4.72. To clarify this point, let’s assume that there are N photons entering the nematic liquid crystal and traveling in the x direction. From eqn. 4.72 we know that there will be $N \exp(-\sigma x_1)$ photons remaining unscattered at position x_1 and $N \exp(-\sigma x_2)$ photons remaining unscattered at position x_2 . It is obvious that the probability for a photon to travel from x_1 to x_2 without being scattered is $\exp[-\sigma(x_2 - x_1)]$ if $x_2 > x_1$. Therefore, we arrive at

$$P_s = \exp(-\sigma \Delta s), \quad (4.75)$$

where Δs is the distance that the photon travels in one time step. If the random number is greater than the survival probability, then the photon is set to be scattered.

The next question is, which direction, which mode should it be scattered into. For the ‘ordinary’ mode photon, it can only be scattered into the ‘extraordinary’ mode. Therefore, we can use $d\sigma_{oe}/d\Omega$ to determine which direction the photon should be scattered right away. For the ‘extraordinary’ mode photon, however, we have to calculate the relative strength of σ_{ee} to σ_{eo} first and again use a random number to determine which mode the photon will be scattered into. Next, we use the associated $d\sigma/d\Omega$ to determine the scattering direction. Unlike the case of isotropic media where we can use a random number generator to linearly map to the outgoing angle, in the nematic to determine the outgoing direction via $d\sigma/d\Omega$ is a tricky business. To utilize the random number for a given $d\sigma/d\Omega$, unavoidably, we have to divide the whole solid angle into grids. We then calculate the relative strength w of $d\sigma/d\Omega$ for each grid and use this to determine how many sites in a probability array this grid will be assigned to. One trivial thought to assign the sites will be like: for a probability array with N sites, the number of sites can be assigned to a grid is the integer part of wN . For example, if the relative strength of $d\sigma/d\Omega$ in the grid $(\theta, \theta + \Delta\theta; \phi, \phi + \Delta\phi)$ is 0.035, then it will be assigned 3 sites in a probability array with 100 sites. Due to the fact that we cannot use probability array with infinite number of sites, it is obvious that this probability array method is prone to truncation errors. Let’s take the example we just discussed above again. If we have a lot of grids with relative strength smaller than 0.01, these grids can not be assigned to any site in the probability array though they may sum up to a significant contribution to the extinguishing coefficient. Of course, one might think that we can increase the size of the array. This can improve the situation at the cost of more computer memories and execution time, but doesn’t really solve the problem. We may, however, use another random number generator to solve this problem statistically. In the process of assigning sites to a given grid, we use a random number in the interval $[0,1)$ and compare it with the decimal part of the wN of the grid. If the random number is smaller, then the number of sites assigned to this grid will then be the closest bigger

integer of wN . On the other hand, if the random number is bigger, then the number of sites assigned to this grid will then be the closest smaller integer of wN .

For nematic liquid crystal with its director along z -axis, we have azimuthal symmetry. We can always rotate the coordinates system about z -axis to make any incoming wavevector be in the x - z plane. Therefore, we only have to build up the probability arrays for the incoming wavevectors with the form as $(k \sin M\Delta\theta, 0, k \cos M\Delta\theta)$ where M is a positive integer and $M\Delta\theta \leq \pi$. After the probability arrays have been built up, we are ready for photon propagation simulation. As illustrated in Fig. 4.8, we first initialize the position \mathbf{r} , wavevector \mathbf{k} , velocity \mathbf{v} , travel length s , and propagation mode (ordinary or extraordinary) of the photon. In each time step, we update \mathbf{r} and s . Then, depending on the current propagation mode of photon, we use the random number generator to produce a random number in the interval $[0,1)$. If this random number is greater than the survival probability, the photon is determined to be scattered. We then use a random number to pick up a site in the associated probability array and determine the new \mathbf{k} , \mathbf{v} , and propagation mode. Utilizing the simulation technique discussed above, we found that photon diffusion approximation can be used in the nematic liquid crystal system with some modification. In the simulation program list in Appendix A, we initialize 1000 photons at origin with their direction in x -direction. The magnetic field direction is along the z -axis. For every certain time steps, we take a snap shot of the positions of the photons. The positional distribution of the photons can be fitted by a Gaussian distribution

$$\rho(x, y, z) = \frac{1}{(2\pi)^{3/2}} \frac{1}{\sigma_x \sigma_y \sigma_z} \exp \left\{ - \left(\frac{(x - x_o)^2}{2\sigma_x^2} + \frac{(y - y_o)^2}{2\sigma_y^2} + \frac{(z - z_o)^2}{2\sigma_z^2} \right) \right\}. \quad (4.76)$$

Comparing it with the solution of the diffusion equation

$$\frac{\partial U}{\partial t} = D_x \frac{\partial^2 U}{\partial x^2} + D_y \frac{\partial^2 U}{\partial y^2} + D_z \frac{\partial^2 U}{\partial z^2} \quad (4.77)$$

for an instantaneous point source in infinite wide medium, we have the following

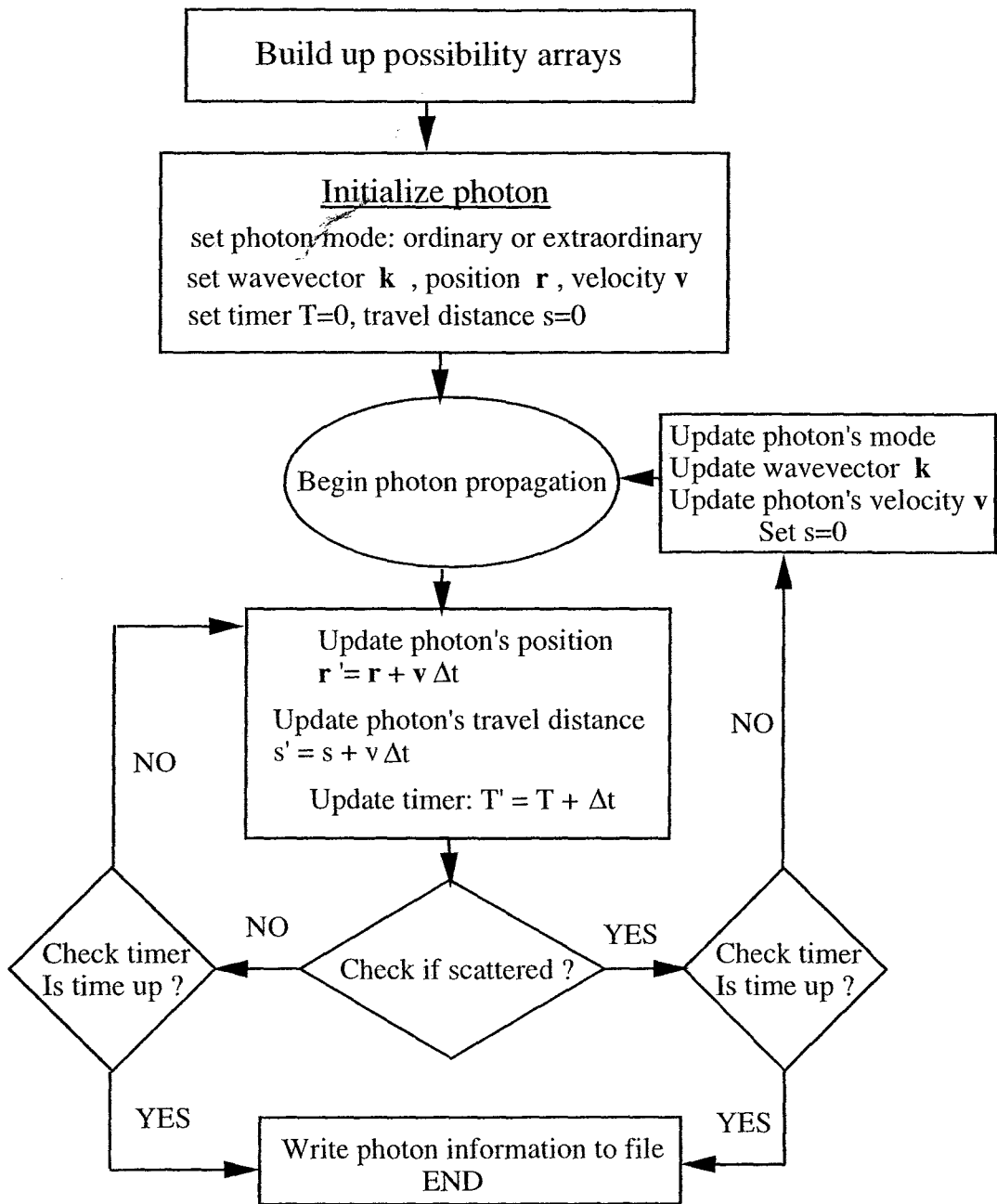


Figure 4.8: Logical procedures of the simulation

relations:

$$\begin{aligned}
 \sigma_x^2 &= 2D_x t \\
 \sigma_y^2 &= 2D_y t \\
 \sigma_z^2 &= 2D_z t
 \end{aligned}
 \tag{4.78}$$

In one set of computer simulation we have performed, we let photons begin to propagate with their initial incident directions along the $+X$ direction. All the physical parameters used in the simulation were taken from the measured results for 5CB at $\lambda = 546\text{nm}$. In Fig. 4.9, 4.10, and 4.11, we show three cross-sectional views of the positional distribution of the photons at $t = 10\text{psec}$ and $t = 100\text{psec}$. At $t = 10\text{psec}$, photons still have memory of their incident directions. At $t = 100\text{psec}$, however, we can see photons' directions are total randomized. From the snap shots we have taken, we can plot σ_i^2 ($i = x, y, z$) as a function of time t . If there exists a linear relation, we can say that photon is diffusion and a half of the slope gives the diffusion constant.

Utilize the simulation and data-analysis procedure described above to 5CB(K15) liquid crystal, we obtained some interesting results. As shown in Fig. 4.12, the linear relation does exist between σ^2 and t . We also observe that D_z is significantly larger than D_x and D_y while D_x and D_y are basically the same. A closer examine of the data for D_x and D_y , we find that these two sets of data do not converge until $t = 500\text{psec}$. In photon diffusion approximation, we assume that photons begin to diffuse at a certain position inside the sample. This position usually is taken to be one transport mean free path away from the incident boundary. Our simulation data also suggest that this assumption is correct. In Fig. 4.12(b), we also plot the $\langle x \rangle$ as a function of t . We can see that $\langle x \rangle$ reaches a constant value $\sim 1.5\text{mm}$ after certain time. From another set of simulations we have performed for photons with the incident directions along the $Z - axis$, we find that we obtained basically the

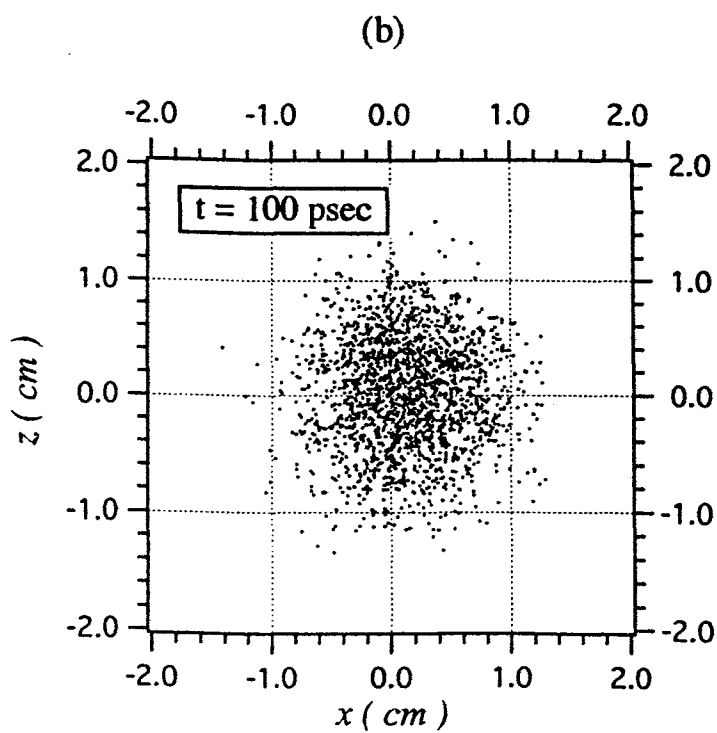
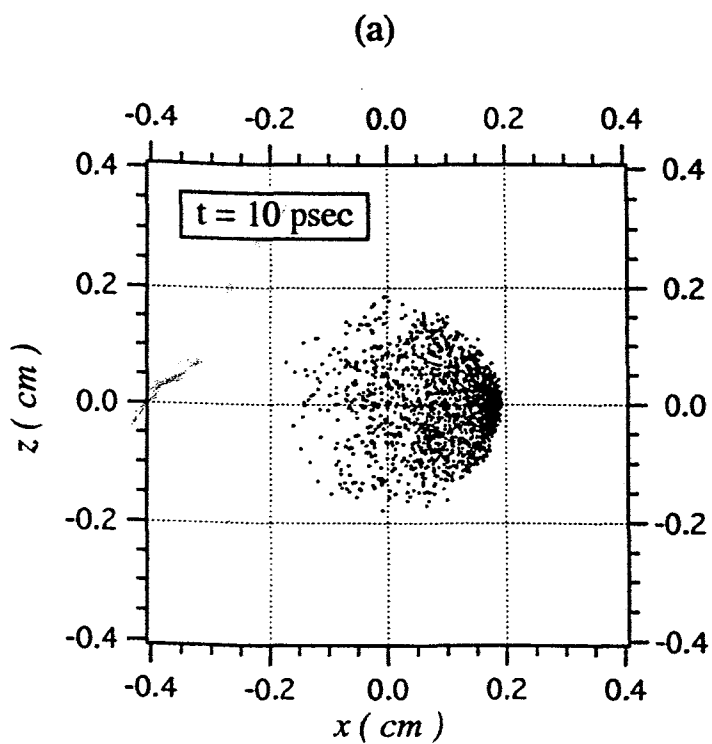


Figure 4.9: Z-X cross-sectional view of the positional distribution of the photons:
(a) $t = 10$ psec (b) $t = 100$ psec

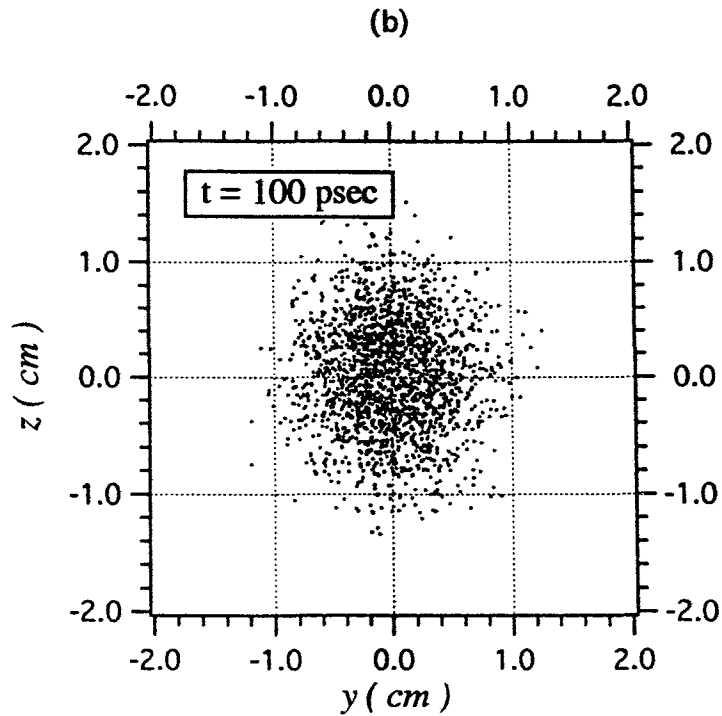
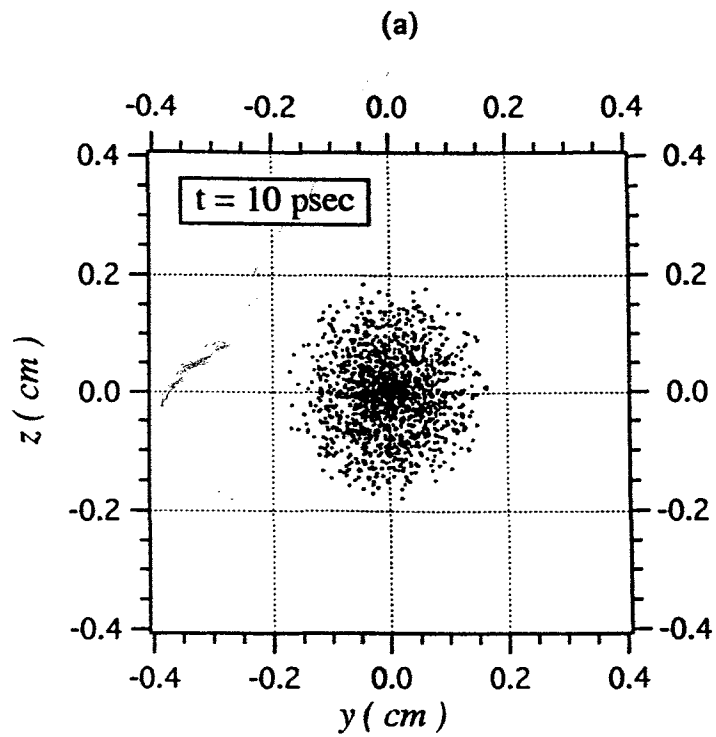


Figure 4.10: Z-Y cross-sectional view of the positional distribution of the photons:
(a) $t = 10$ psec (b) $t = 100$ psec

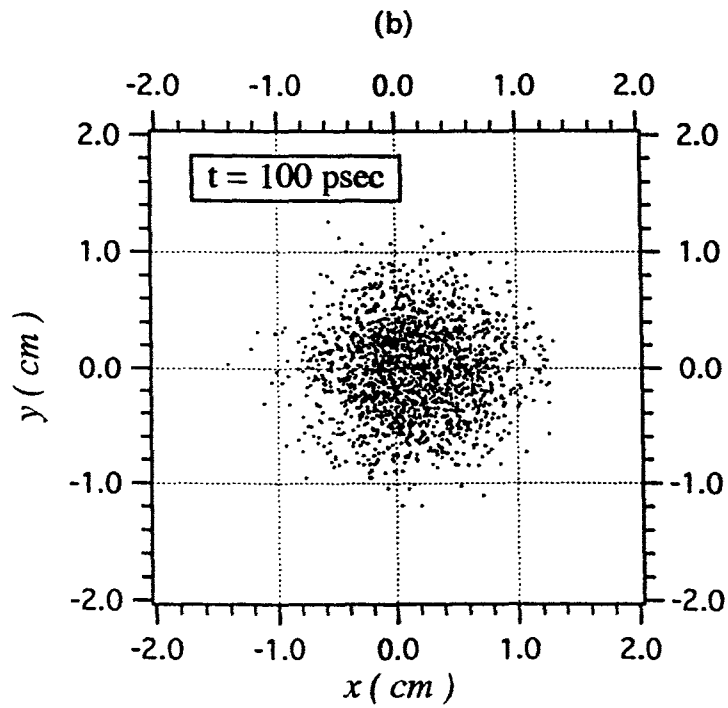
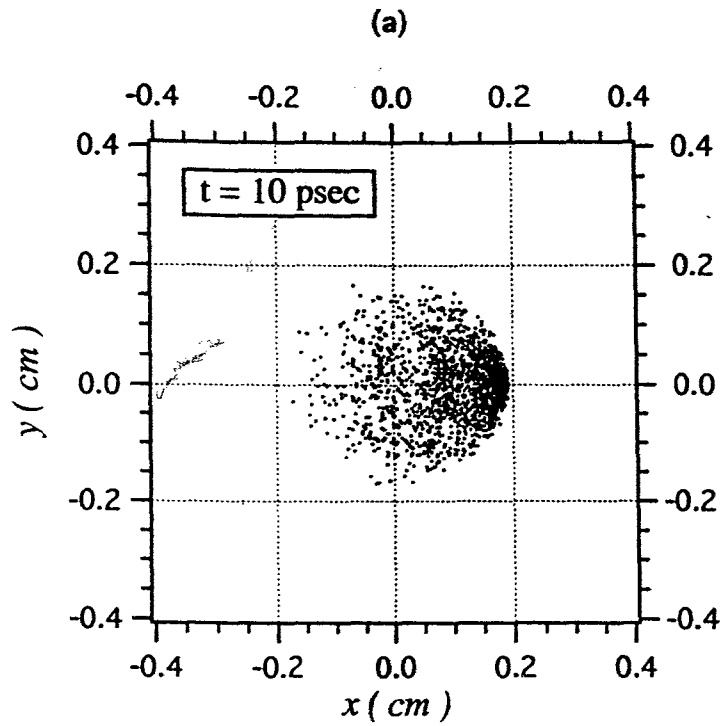
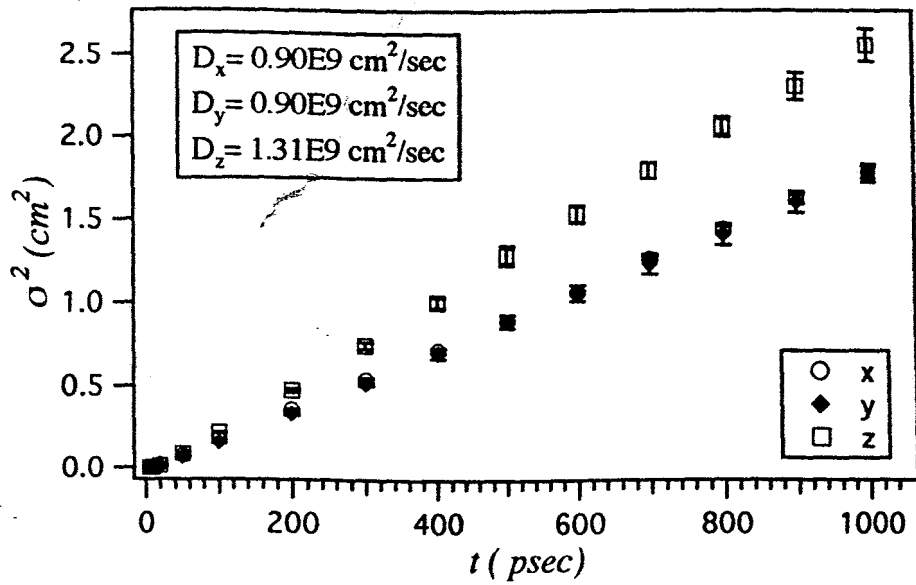


Figure 4.11: Y-X cross-sectional view of the positional distribution of the photons:
(a) $t = 10\text{psec}$ (b) $t = 100\text{psec}$

(a)



(b)

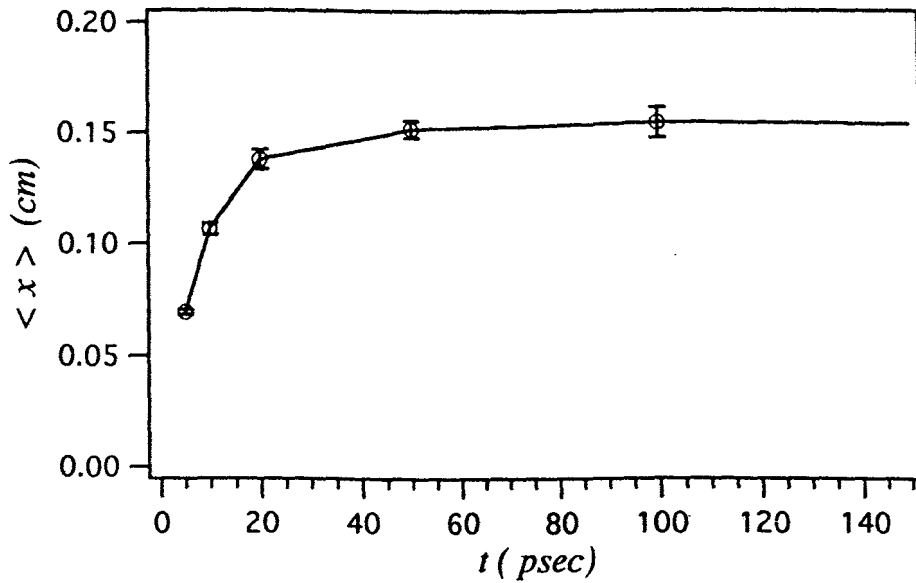


Figure 4.12: Results of simulation: (a) Photon diffusion coefficients are derived from eqn. 4.79. (b) The x -component of the averaged photon position approaches a constant value.

same diffusion constants but $\langle z \rangle \sim 2.4\text{mm}$. From these results, we can conclude that if we replace the diffusion constant with a diffusion tensor in the photon diffusion equation, photon diffusion approximation should work in nematic liquid crystals.

4.5 Experiment set up and results

In the previous section, we discussed the possibility of applying photon diffusion equation and DWS to nematic liquid crystal system. We find from the simulation results that photon diffusion approximation is applicable with some modifications. First of all, we no longer have a scalar photon diffusion constant; instead, a photon diffusion tensor should be put in the diffusion equation. With suitable choice of coordinates system, this tensor can be diagonalized. Furthermore, it also suggests that photons ‘diffuse’ with different speeds in different directions. The simplest experiment one can imagine regarding this will be a transmission measurement as suggested in the previous section. We expect different transmission intensity profiles along different major axes. The practical experiment becomes only a little bit more complicated. The nematic liquid crystal we used is called K15 or 5CB. Its critical temperature is only about 35°C . This provides some advantages in our experiment. The K15 liquid crystal was stored in a 1-cm-thick cylindrical cell. The diameter of the cell is only 1.95 cm. Due to the fact that the dielectric constant of liquid crystal is sensitive to temperature fluctuations, the sample was placed in a temperature controlled housing during experiment. Fig. 4.13 shows the sample holder and the cell used in this experiment. To obtain a well defined director direction, the sample was heated up to its isotropic phase and then slowly cooled down in a 2000 gauss magnetic field. This way assures the director will be in the direction of the magnetic field. In 2000 gauss magnetic field, the magnetic coherence length for the sample we used was about $11.8\ \mu\text{m}$. Comparing with the dimension of our sample, the boundary effects can be neglected in most cases. The end surfaces of the cell are

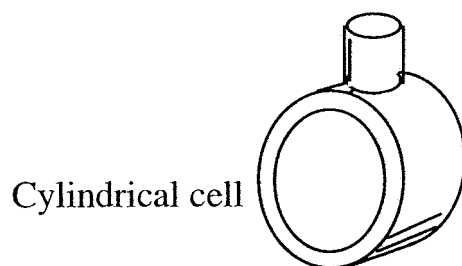
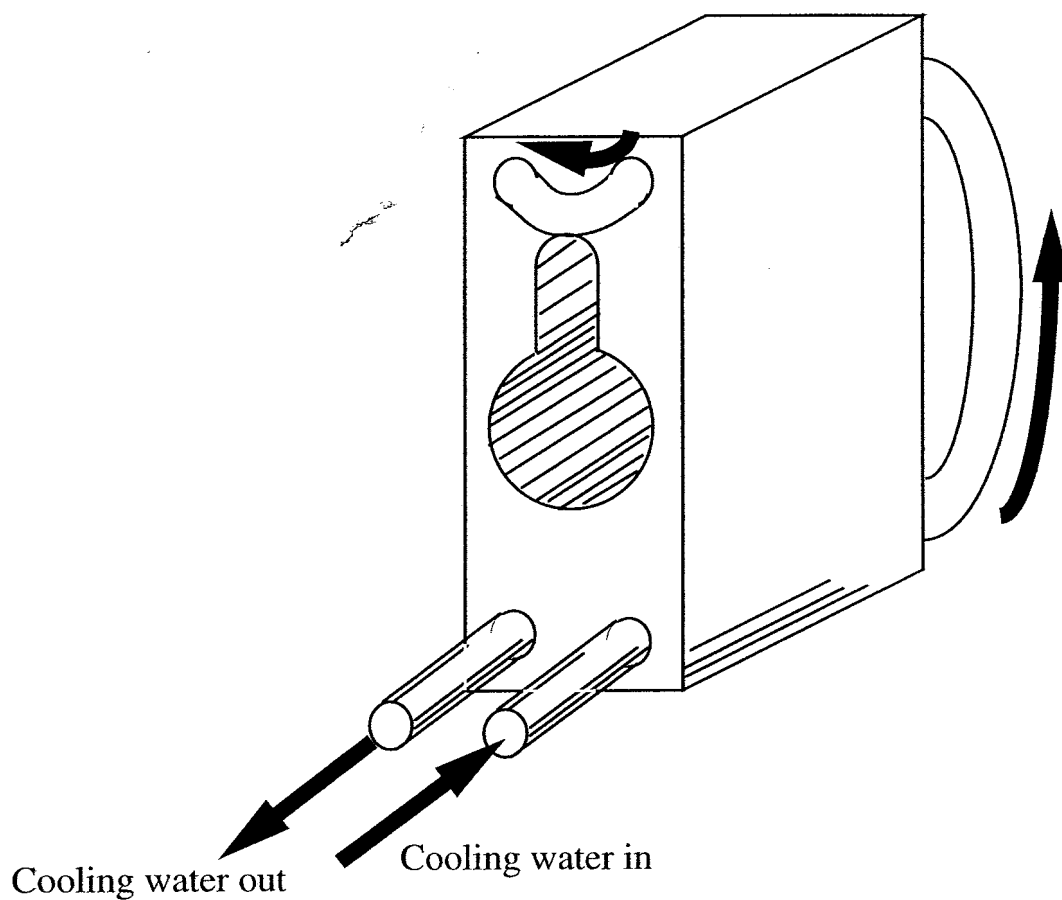
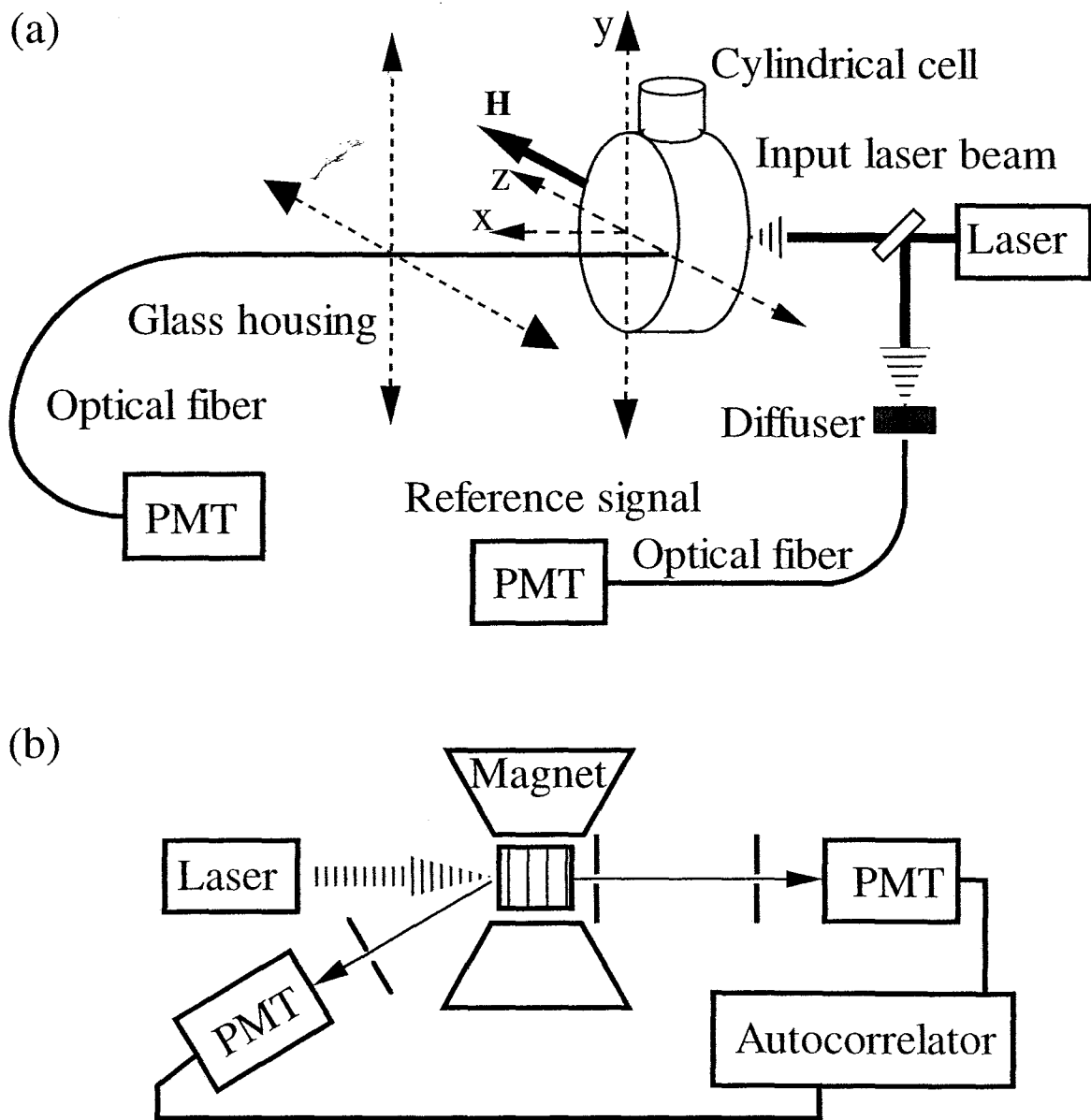


Figure 4.13: Sample holder and cell.

oriented to be parallel to the magnetic field. Fig. 4.14 shows a simplified schematic draw of the experiment set-up. The green light ($\lambda = 514.5nm$) from a Argon ion laser impinges on the center of one end surface of the sample with 90° incident angle. The size of illuminating area was limited to be only 1-mm in diameter by a pin hole. On the other side, a glass housing for the detecting optical fiber was mounted on a translation stage and was capable to translate both in the direction parallel or perpendicular to the magnetic field. The tip of the optical fiber was made as close to the cell as possible to limit the collection area and increase the spatial resolution. As shown in Fig. 4.14, the laboratory coordinates system was set up as the following: z-axis was in the direction of the magnetic field, x-axis was in the direction of incident beam and passed the central axis of the cell, and y-axis was perpendicular to both x-axis and z-axis. We manually moved the detecting fiber to scan the intensity profile along the z-axis and y-axis for several times. Fig. 4.15 shows the results we have obtained and it does prove that photon diffuse with different diffusion constants in different directions. Assuming the knowledge of the diffusive reflectivity on the boundaries, we can solve the photon diffusion equation for a given set of $(D_{\perp}, D_{\parallel})$ and obtain the intensity profile. Though analytical solution is not always possible for a given sample geometry, we can solve the equation numerically. For a infinite-wide slab geometry with a point input light source, if we plot the equal-energy contours of the solution at the output plane, we obtain ellipses with their ratios of major-axis/minor-axis equal to $\sqrt{D_{\parallel}/D_{\perp}}$. For the cylindrical cell geometry in our experiment with a point source impinging at the center, the shapes of these equal-energy contours at the output plane change from a ellipse at the center to a circle at the boundary. Due to the difficulty of measuring the absolute transmitted intensity, the relative intensity profile could be more meaningful. Comparing with the experiment data with the calculation, we can at least get an idea of the ratio D_{\parallel}/D_{\perp} . As shown in Fig. 4.15, we have $D_{\parallel}/D_{\perp} \sim 1.4$. Compared with the result of



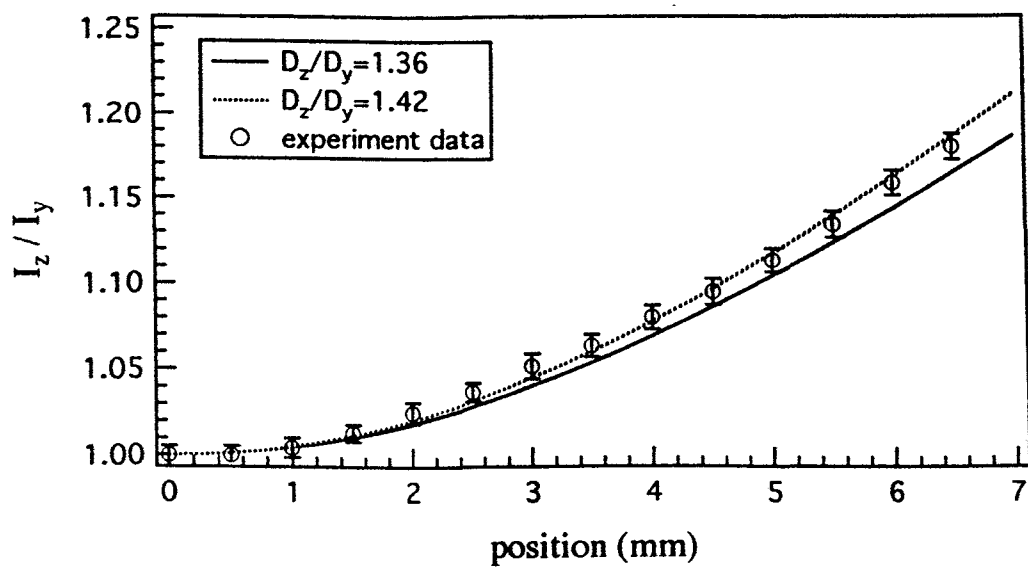
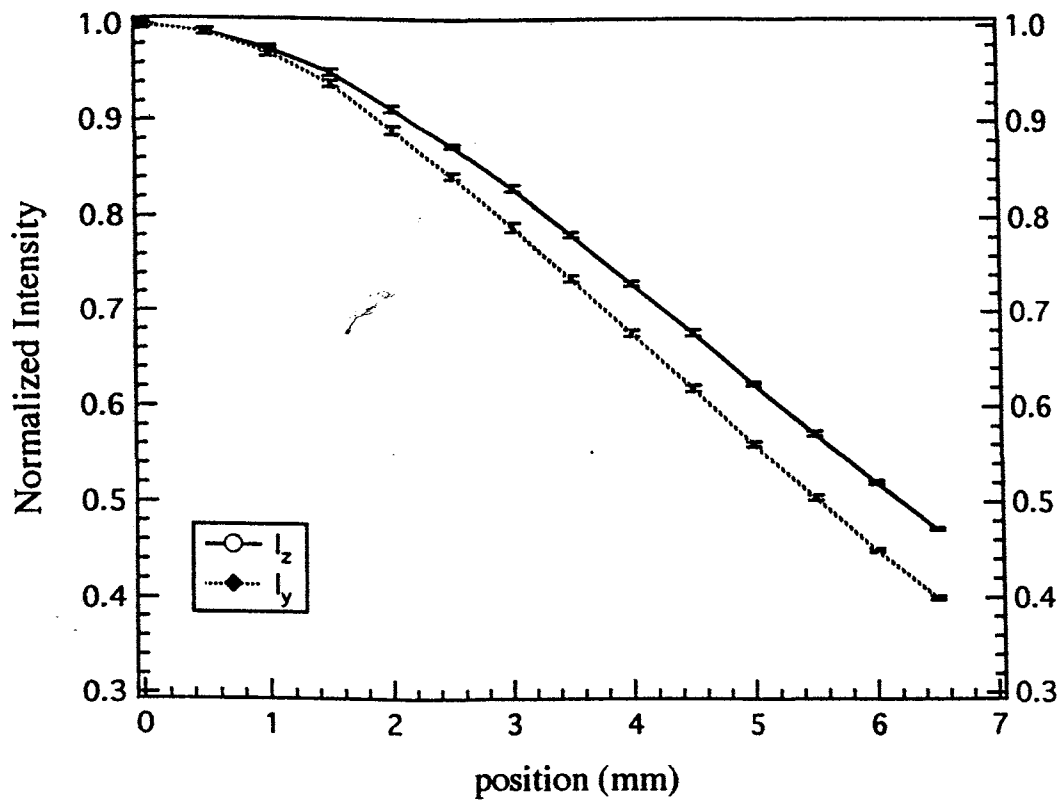


Figure 4.15: Results of diffusive transmission measurement

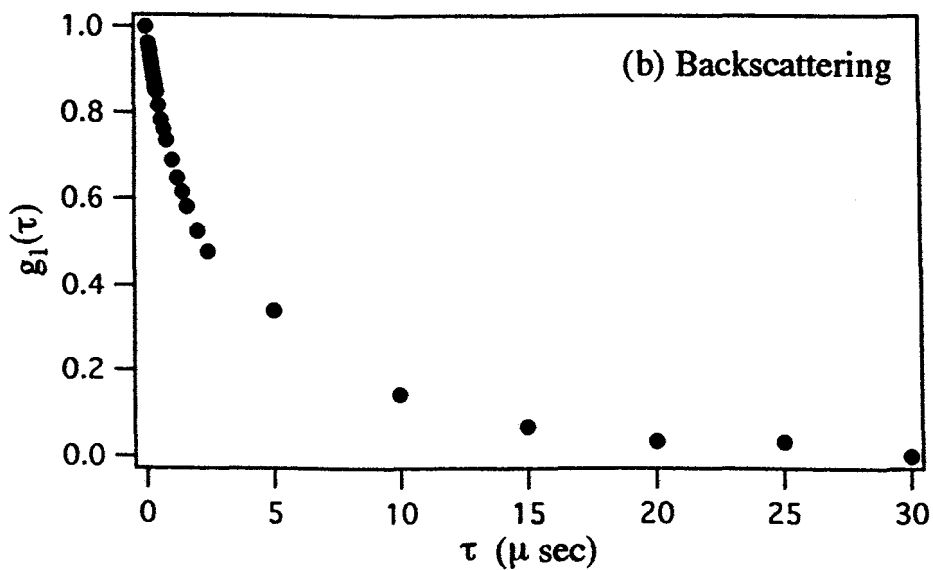
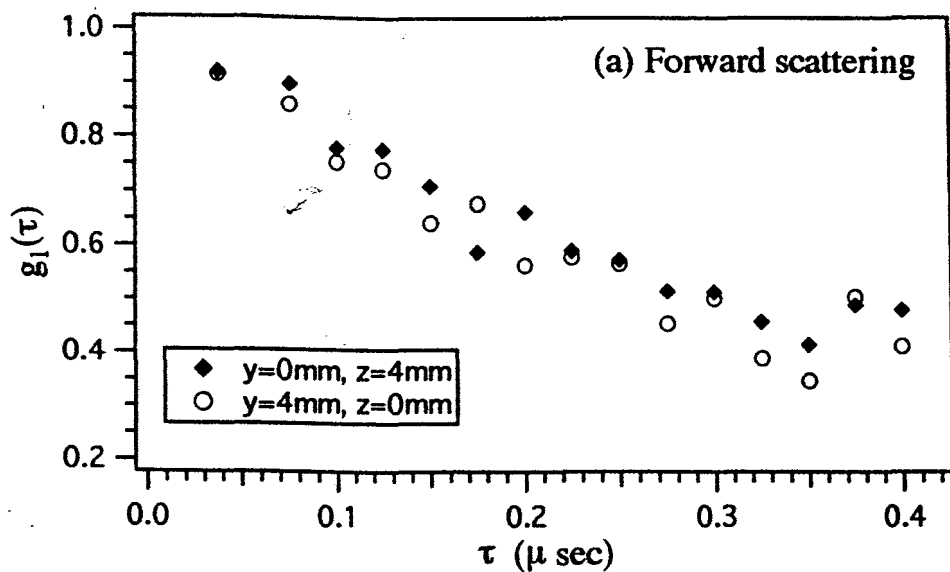


Figure 4.16: Results of dynamical measurements

Chapter 5

Conclusions

In this dissertation we investigate the multiple light scattering phenomenon both in isotropic and anisotropic turbid media. We have performed experiments utilizing DWS technique to probe the Brownian dynamics on the time scales shorter than the hydrodynamic time of the studied system. Our results indicate the importance of hydrodynamic interactions between the suspended particles. We also performed series of experiments to test the validity of DWS for the sample with dimensions comparable to the transport mean free path. We found that, in a plane-wave/slab geometry, the required cell thickness to use DWS depends on the size of the particle.

For the multiple light scattering in nematic liquid crystal, we performed both computer simulations and experiments to test the validity of photon diffusion approximation. Our results suggest that the photon diffusion approximation is valid if we use a photon diffusion tensor instead of a photon diffusion constant. We also measured the electric field autocorrelation function for both forward and backward scattering geometries and were able to obtain the effective rotational viscosity of the sample. In conclusion, we demonstrate the validity and usefulness of DWS both in isotropic and anisotropic turbid media.

Appendix A

Code List of The Simulation Performed in Chapter 4

```

/*****/
/*                                     */
/* Photon Propagation in Nematic Liquid Crystal */
/*                                     */
/*      Written by Ming Hsu Kao in 1995      */
/*                                     */
/*****/

#include <stdio.h>
#include <stdlib.h>
#include <math.h>
#define pi 3.1415926535898
#define c 29979245800./* speed of light in vacuum in cgs units */
#define dt 1E-13      /* time step size in simulation      */

/*****/
/* Declaration of some data types, functions, and variables */
/*****/

typedef struct
{
    double x;
    double y;
    double z;
} vector;

/** Vector manipulating function **/

```

```

double dot(vector a, vector b);
vector timeconst(double a, vector v);
vector SVT( double a1, double a2, double a3);

/**/ Calculate Wave Vectors ***/

void CalInVectors(double t_in,double p_in);
void CalOutVectors(double t_out,double p_out);
void CalQVectors();

/**/ Calculate differential cross-section ***/
double F(vector ki,vector ko,int mode_in,int mode_out);

short int now_theta,now_phi,now_theta_in,chance;
short int k,iq,old_lable,new_lable,deno,nom;
short int p_mode[1000],polar[1000],azi[1000],p_e[1000],p_o[1000];
short int tmp[1720],poe[91][1720],peo[91][1720],pee[91][1720];
short int aoe[91][181][600],aeo[91][181][600],aee[91][181][600];
short int Namp[181][181],Npoe[91],Npeo[91],Npee[91];
short int Naoe[91][181],Naeo[91][181],Nae[91][181];

double ss1[181],ss2[181],ss3[181],s1[181],s2[181],s3[181];
double Ne[181],freq,wlen,no,ne,nr2,qz,qp,dg;
double KK[4],Xa,Ea,H,kb,T,L,Eo,Ee,temamp;
double d_i[2],d_o[2],n_i[2],n_o[2],E_e;
double p_max_x[1000],p_min_x[1000],p_max_y[1000],p_min_y[1000];
double p_max_z[1000],p_min_z[1000],p_pt[1000],p_st[1000];

```

```

double Amp_oe[181][181],Amp_ee[181][181],Amp_eo[181][181];
double p_ps[1000],asum[181],chance_o[181],chance_e[181];

vector eki,eko,ki[2],ko[2],i[2],f[2],q[2][2];
vector photon[1000],ski[2],sko[2],e[2][2][2];

main(argc, argv)
int argc;
char *argv[];
{
    int    theta_in,theta_out,phi_in,phi_out;
    double angle,sum_f12,sum_f21,sn,sum1,sum2,sum3,sum_f22,ls,dls;
    double ox,oy,oz,ps;
    double gp,tau;
    double mcl,cx,cy,cz;
    double OF3,F3,osum1,osum2,osum3,F1,F2,OF1,OF2,rn;
    int    j,m,p,l,index_p,out_p,new_azi,index_o;
    int    k,tsteps,dsteps,N_o_photon;
    float tmp1,tmp2,tmp3,tmp4,tmp5,snf;
    char fname[20],fname1[20],fname2[20],fname3[20];
    long rseed;
    int tp,i_angle,snd,ipo,iph,recal,pm;
    FILE *ftp1,*ftp2,*ftp3;

    if(argc!=8)
        {
            printf("Usage: xplc mcl(cm) r_seed fname toatl_steps
                    steps_to_save switch i_angle\n");
        }

```

```

    exit(1);
}
else
{
    mcl=atof(argv[1]);
        rseed=atol(argv[2]);
        tsteps=atoi(argv[4]);
        dsteps=atoi(argv[5]);
        recal=atoi(argv[6]);
    i_angle=atoi(argv[7]);
        }
chance=1;
dg=pi/180;
no=1.543;
ne=1.710;

/* In c.g.s units */
wlen=546E-7;
freq=2.0*pi*c/wlen;
nr2=ne*ne/no/no;
Eo=no*no;
Ee=ne*ne;
Ea=ne*ne-no*no;
KK[1]=0.42E-6;
KK[2]=0.23E-6;
KK[3]=0.53E-6; /* in cgs units */
kb=1.38066E-16;
T=300;

```

```

Xa=KK[3]/mcl/mcl;
H=1;
d_i[0]=0;
d_o[0]=0;
n_i[0]=no;
n_o[0]=no;
/*  comments on the variables */
/*
ki,eki  :  input wave vector and its unit vector;
ko,eko  :  output wave vector and its unit vector;
freq    :  frequence of light in vacuum
wlen    :  wavelength of light in vacuum
no      :  ordinary index of refraction
ne      :  extraordinary index of refraction
d_i     :  angle between E and D for the input beam
d_o     :  angle between E and D for the output beam
qz      :  z component of the scattering vector q
qp      :  perpendicular component of the scattering vector q
*/

/* calculate the values of ne(theta) for 0 degree to 359 degree */

for(j=0;j<=90;j++)
{
  angle=j*dg;
  Ne[j]=1/sqrt(cos(angle)*cos(angle)/no/no+sin(angle)*sin(angle)/ne/ne);
  Ne[180-j]=Ne[j];
}

```

```

Ne[180]=no;
Ne[90]=ne;
Ne[0]=no;

/***** Main loop to calculate cross-section *****/

srand48(rseed);
for(p=0;p<=90;p++)
{
  if(recal==1)
  {
    theta_in=p;
    now_theta_in=p;
    phi_in=0;
    CalInVectors((double)theta_in,(double)phi_in);
    sum_f12=0;
    sum_f21=0;
    sum_f22=0;
    osum1=0;
    osum2=0;
    osum3=0;
    for(j=0;j<=180;j++)
    {
theta_out=j;
      now_theta=theta_out;
      if((j==0)||(j==180))
{
        sn=sin(0.000025*dg)*0.5;

```

```

        theta_out=0.000025;
    }
else
{
sn=sin(theta_out*dg);
}
sum1=0;
sum2=0;
sum3=0;

    CalOutVectors((double)theta_out,0.0);
    CalQVectors();
    OF1=F(ki[0],ko[1],0,1);
    OF2=F(ki[1],ko[0],1,0);
    OF3=F(ki[1],ko[1],1,1);
    for(m=0;m<=180;m++)
    {
        phi_out=m;
        now_phi=phi_out;
        if((j==0)|| (j==180))
CalOutVectors(0.25,(double)phi_out);
        else
            CalOutVectors((double)theta_out,(double)phi_out);

        CalQVectors();
        Amp_oe[j][m]=sn*F(ki[0],ko[1],0,1);
        Amp_eo[j][m]=sn*F(ki[1],ko[0],1,0);
        Amp_ee[j][m]=sn*F(ki[1],ko[1],1,1);

```

```

if((m==0)||(m==180))
{
    sum1+=Amp_oe[j][m];
    sum2+=Amp_eo[j][m];
    sum3+=Amp_ee[j][m];
}
else
{
    sum1+=Amp_oe[j][m];
    sum2+=Amp_eo[j][m];
    sum3+=Amp_ee[j][m];
    sum1+=Amp_oe[j][m];
    sum2+=Amp_eo[j][m];
    sum3+=Amp_ee[j][m];
}
}
sum_f12+=sum1;
sum_f21+=sum2;
sum_f22+=sum3;
osum1+=sum1;
osum2+=sum2;
osum3+=sum3;
}
ss1[p]=sum_f12*dg*dg*(freq*freq/4.0/pi/c/c)
        *(freq*freq/4.0/pi/c/c)*kb*T*Ea*Ea;
ss2[p]=sum_f21*dg*dg*(freq*freq/4.0/pi/c/c)
        *(freq*freq/4.0/pi/c/c)*kb*T*Ea*Ea;
ss3[p]=sum_f22*dg*dg*(freq*freq/4.0/pi/c/c)

```

```

*(freq*freq/4.0/pi/c/c)*kb*T*Ea*Ea;

s1[p]=osum1;
s2[p]=osum2;
s3[p]=osum3;
ss1[180-p]=ss1[p];
ss2[180-p]=ss2[p];
ss3[180-p]=ss3[p];
s1[180-p]=s1[p];
s2[180-p]=s2[p];
s3[180-p]=s3[p];
chance_o[p]=1-exp(-ss1[p]*dt*c/no);
chance_e[p]=1-exp(-(ss2[p]+ss3[p])*dt*c/Ne[p]);
chance_o[180-p]=chance_o[p];
chance_e[180-p]=chance_e[p];

/***** Calculate poe *****/

for(j=0;j<=180;j++)
{
  asum[j]=Amp_oe[j][0];
  for(m=1;m<180;m++)
  {
    asum[j]+=2*Amp_oe[j][m];
  }
  asum[j]+=Amp_oe[j][180];
  deno=600;
  nom=200;
  for(iq=0;iq<200;iq++)

```

```

        {
            old_lable=0;

for(m=0;m<=180;m++)
{
    if((m==0)|| (m==180))
        {
            temamp=nom*Amp_oe[j][m]/asum[j];
        }
    else
        {
            temamp=nom*2*Amp_oe[j][m]/asum[j];
        }
    rn=drand48();
    if(rn<(temamp-(int)temamp))
        Namp[j][m]=1+(int)temamp;
    else
        Namp[j][m]=(int)temamp;

    new_lable=old_lable+Namp[j][m];
        if(new_lable>600)
break;

for(k=old_lable;k<new_lable;k++)
{
    tmp[k]=m;
}
old_lable=new_lable;

```

```

    }
    deno=new_lable;
    nom+=50;
    if(new_lable>600)
    {
        break;
    }
    else
    {
        Naoe[p][j]=new_lable;
        for(k=0;k<Naoe[p][j];k++)
            aoe[p][j][k]=tmp[k];
    }
}
}
deno=720;
nom=520;
for(iq=0;iq<200;iq++)
{
    old_lable=0;
    if(p==90)
    {
        for(j=0;j<=90;j++)
        {
rn=drand48();
            temamp=nom*asum[j]/s1[p];
            if(rn<(temamp-(int)temamp))
                Namp[j][0]=1+(int)temamp;

```

```

else
    Namp[j][0]=(int)temamp;

new_lable=old_lable+Namp[j][0];
if(new_lable>1720)
    break;

for(k=old_lable;k<new_lable;k++)
    tmp[k]=j;

old_lable=new_lable;
if(j!=90)
{
    new_lable=old_lable+Namp[j][0];
    for(k=old_lable;k<new_lable;k++)
    {
        tmp[k]=180-j;

    }
    old_lable=new_lable;
}
if(new_lable>1720)
    break;
}

}

else
{

```

```

for(j=0;j<=180;j++)
{
rn=drand48();
temamp=nom*asum[j]/s1[p];
    if(rn<(temamp-(int)temamp))
        Namp[j][0]=1+(int)temamp;
    else
        Namp[j][0]=(int)temamp;

    new_lable=old_lable+Namp[j][0];
    if(new_lable>1720)
        break;

    for(k=old_lable;k<new_lable;k++)
    {
        tmp[k]=j;
    }
    old_lable=new_lable;
    if(new_lable>1720)
        break;
}
}
deno=new_lable;
nom+=200;
if(new_lable>1720)
{
    break;
}

```

```

else
{
    Npoe[p]=new_lable;
    for(k=0;k<Npoe[p];k++)
        poe[p][k]=tmp[k];
}
}

/***** Calculate peo *****/

for(j=0;j<=180;j++)
{
    asum[j]=Amp_eo[j][0];
    for(m=1;m<180;m++)
    {
        asum[j]+=2*Amp_eo[j][m];
    }
    asum[j]+=Amp_eo[j][180];
    deno=600;
    nom=300;
    for(iq=0;iq<200;iq++)
    {
        old_lable=0;
        for(m=0;m<=180;m++)
        {
            if((m==0)|| (m==180))
            {
                temamp=nom*Amp_eo[j][m]/asum[j];
            }
        }
    }
}

```

```

    }
    else
    {
        temamp=nom*2*Amp_eo[j][m]/asum[j];
    }
rn=drand48();
    if(rn<(temamp-(int)temamp))
        Namp[j][m]=1+(int)temamp;
    else
        Namp[j][m]=(int)temamp;

    new_lable=old_lable+Namp[j][m];
    if(new_lable>600)
        break;

    for(k=old_lable;k<new_lable;k++)
        tmp[k]=m;

    old_lable=new_lable;
}
deno=new_lable;
nom+=50;
if(new_lable>600)
{
    break;
}
else
{

```

```

        Naeo[p][j]=new_lable;
        for(k=0;k<Naeo[p][j];k++)
            aeo[p][j][k]=tmp[k];
    }
}
}
deno=1720;
nom=520;
for(iq=0;iq<200;iq++)
{
    old_lable=0;
    if(p==90)
    {
        for(j=0;j<=90;j++)
        {
            rn=drand48();
            temamp=nom*asum[j]/s2[p];
            if(rn<(temamp-(int)temamp))
                Namp[j][0]=1+(int)temamp;
            else
                Namp[j][0]=(int)temamp;

            new_lable=old_lable+Namp[j][0];
            if(new_lable>1720)
                break;

            for(k=old_lable;k<new_lable;k++)
                tmp[k]=j;

```

```

old_label=new_label;
if(j!=90)
{
    new_label=old_label+Namp[j][0];
    for(k=old_label;k<new_label;k++)
        tmp[k]=180-j;

    old_label=new_label;
}
if(new_label>1720)
    break;
}

}
else
{
    for(j=0;j<=180;j++)
    {
rn=drand48();
        temamp=nom*asum[j]/s2[p];
        if(rn<(temamp-(int)temamp))
            Namp[j][0]=1+(int)temamp;
        else
            Namp[j][0]=(int)temamp;

        new_label=old_label+Namp[j][0];
        if(new_label>1720)

```

```

        break;

    for(k=old_lable;k<new_lable;k++)
        tmp[k]=j;

    old_lable=new_lable;
    if(new_lable>1720)
        break;
}
}
deno=new_lable;
nom+=200;
if(new_lable>1720)
{
    break;
}
else
{
    Npeo[p]=new_lable;
    for(k=0;k<Npeo[p];k++)
        peo[p][k]=tmp[k];
}
}

/***** Calculate pee *****/

for(j=0;j<=180;j++)
{

```

```

asum[j]=Amp_ee[j][0];
for(m=1;m<180;m++)
{
    asum[j]+=2*Amp_ee[j][m];
}
asum[j]+=Amp_ee[j][180];
deno=600;
nom=300;
for(iq=0;iq<200;iq++)
{
    old_lable=0;
    for(m=0;m<=180;m++)
    {
        if((m==0)||(m==180))
        {
            temamp=nom*Amp_ee[j][m]/asum[j];
        }
        else
        {
            temamp=nom*2*Amp_ee[j][m]/asum[j];
        }
    }
rn=drand48();
    if(rn<(temamp-(int)temamp))
        Namp[j][m]=1+(int)temamp;
    else
        Namp[j][m]=(int)temamp;

    new_lable=old_lable+Namp[j][m];

```

```

        if(new_lable>600)
            break;

        for(k=old_lable;k<new_lable;k++)
            tmp[k]=m;

        old_lable=new_lable;
    }
    deno=new_lable;
    nom+=50;
    if(new_lable>600)
    {
        break;
    }
    else
    {
        Naee[p][j]=new_lable;
        for(k=0;k<Naee[p][j];k++)
            aee[p][j][k]=tmp[k];
    }
}
deno=1720;
nom=520;
for(iq=0;iq<200;iq++)
{
    old_lable=0;
    if(p==90)

```

```

{
for(j=0;j<=90;j++)
{
rn=drand48();
temamp=nom*asum[j]/s3[p];
if(rn<(temamp-(int)temamp))
    Namp[j][0]=1+(int)temamp;
else
    Namp[j][0]=(int)temamp;

new_lable=old_lable+Namp[j][0];
if(new_lable>1720)
    break;
for(k=old_lable;k<new_lable;k++)
    tmp[k]=j;

old_lable=new_lable;
if(j!=90)
{
new_lable=old_lable+Namp[j][0];
for(k=old_lable;k<new_lable;k++)
    tmp[k]=180-j;

old_lable=new_lable;
}
if(new_lable>1720)
    break;
}
}

```

```

}
else
{
  for(j=0;j<=180;j++)
  {
rn=drand48();

    temamp=nom*asum[j]/s3[p];
    if(rn<(temamp-(int)temamp))
      Namp[j][0]=1+(int)temamp;
    else
      Namp[j][0]=(int)temamp;

    new_lable=old_lable+Namp[j][0];
    if(new_lable>1720)
      break;

    for(k=old_lable;k<new_lable;k++)
    {
      tmp[k]=j;
    }
    old_lable=new_lable;
    if(new_lable>1720)
      break;
  }
}
deno=new_lable;
nom+=200;
if(new_lable>1720)

```

```

    {
        break;
    }
    else
    {
        Npee[p]=new_lable;
        for(k=0;k<Npee[p];k++)
            pee[p][k]=tmp[k];
    }
}
printf("%d\t%d\t%d\n",Npoe[p],Npeo[p],Npee[p]);
}
}
if(recal==1)
{
ftp2=fopen("SS","w");
for(p=0;p<=90;p++)
{
    fprintf(ftp2,"%e %e %e %e %e %e\n",
s1[p],s2[p],s3[p],ss1[p],ss2[p],ss3[p]);
    sprintf(fname1,"poe%d",p);

    ftp1=fopen(fname1,"w");
    fprintf(ftp1,"%d\n",Npoe[p]);
    for(j=0;j<Npoe[p];j++)
        fprintf(ftp1,"%d\n",poe[p][j]);
    fclose(ftp1);
    sprintf(fname1,"peo%d",p);

```

```

ftp1=fopen(fname1,"w");
fprintf(ftp1,"%d\n",Npeo[p]);
for(j=0;j<Npeo[p];j++)
    fprintf(ftp1,"%d\n",peo[p][j]);
fclose(ftp1);
if((p%10)==0)
{
sprintf(fname1,"pee%d",p);
ftp1=fopen(fname1,"w");
fprintf(ftp1,"%d\n",Npee[p]);
for(j=0;j<Npee[p];j++)
    fprintf(ftp1,"%d\n",pee[p][j]);
fclose(ftp1);
}
}
}
fclose(ftp2);
}
printf("Begin to simulate\n");
printf("Input angle=%d\n",i_angle);
for(pm=0;pm<=1;pm++)
{
for(p=0;p<1000;p++)
{
photon[p]=SVT(0,0,0);
p_st[p]=0;
polar[p]=i_angle;
azi[p]=0;

```

```

    p_ps[p]=0;
    p_pt[p]=0;
    p_o[p]=0;
    p_e[p]=0;
    p_max_x[p]=0;
    p_max_y[p]=0;
    p_max_z[p]=0;
    p_min_x[p]=0;
    p_min_y[p]=0;
    p_min_z[p]=0;
}

if(pm==0)
sprintf(fname,"%s_o",argv[3]);
else
sprintf(fname,"%s_e",argv[3]);

for(p=0;p<1000;p++)
p_mode[p]=pm;

for(j=1;j<=tsteps;j++)
{
    srand48((long)(rn*1E8));
    for(p=0;p<1000;p++)
    {
        switch(p_mode[p])
        {
            case 0:

```

```

    if(polar[p]>90)
    {
index_p=180-polar[p];
    }
    else
    {
        index_p=polar[p];
    }

    ls=dt*c/no;
    p_pt[p]+=dt;
    p_ps[p]+=ls;
    p_st[p]+=dt;
    photon[p].x+=ls*sin(polar[p]*dg)*cos(azi[p]*dg);
    photon[p].y+=ls*sin(polar[p]*dg)*sin(azi[p]*dg);
    photon[p].z+=ls*cos(polar[p]*dg);
    rn=drand48();
    if(rn<chance_o[index_p])
{
    rn=drand48();
    index_o=(int)(Npoe[index_p]*rn);
    out_p=poe[index_p][index_o];
    if(polar[p]>90)
    {
        polar[p]=180-out_p;
    }
    else
    {
        polar[p]=out_p;
    }
}

```

```

    }
    rn=drand48();
    index_o=(int)(Naoe[index_p][polar[p]]*rn);
    out_p=aoe[index_p][out_p][index_o];
    if(chance>0)
{
    azi[p]+=out_p;
}
    else
{
azi[p]+=(360-out_p);
}
chance=-1*chance;
    azi[p]=azi[p]%360;
    p_st[p]=0;
    p_e[p]+=1;
    p_mode[p]=1;
    /** turn direction into poynting vector **/
    if(drand48()>(s_ang[polar[p]]-(int)s_ang[polar[p]]))
        polar[p]-=(short int)s_ang[polar[p]];
    else
        polar[p]-=(1+(short int)s_ang[polar[p]]);
    }
break;

case 1:
    ls=cos(dg*s_ang[polar[p]])*dt*c/Ne[polar[p]];
    p_pt[p]+=dt;

```

```

    p_ps[p]+=1s;
    photon[p].x+=1s*sin(polar[p]*dg)*cos(azi[p]*dg);
    photon[p].y+=1s*sin(polar[p]*dg)*sin(azi[p]*dg);
    photon[p].z+=1s*cos(polar[p]*dg);
    p_st[p]+=dt;
    rn=drand48();
    if(rn<chance_e[polar[p]])
        {
            if(polar[p]>90)
                {
index_p=180-polar[p];
                }
            else
                {
                    index_p=polar[p];
                }
            rn=drand48();
            if(rn<(s2[index_p]/(s2[index_p]+s3[index_p])))
                {
                    rn=drand48();
                    index_o=(int)(Npeo[index_p]*rn);
                    out_p=peo[index_p][index_o];
                    if(polar[p]>90)
                        {
                            polar[p]=180-out_p;
                        }
                    else
                        {

```

```

        polar[p]=out_p;
    }
rn=drand48();
    index_o=(int)(Naeo[index_p][polar[p]]*rn);
    out_p=aeo[index_p][out_p][index_o];
    if(chance>0)
    {
        azi[p]+=out_p;
    }
    else
    {
        azi[p]+=(360-out_p);
    }
chance=-1*chance;
    azi[p]=azi[p]%360;
    p_st[p]=0;
    p_mode[p]=0;
    p_o[p]+=1;
}
else
{
rn=drand48();
    index_o=(int)(Npee[index_p]*rn);
    out_p=pee[index_p][index_o];
    if(polar[p]>90)
    {
        polar[p]=180-out_p;
    }
}

```

```

else
{
    polar[p]=out_p;
}
rn=drand48();
index_o=(int)(Nae[e[index_p][polar[p]]*rn]);
out_p=aee[index_p][out_p][index_o];
if(chance>0)
{
azi[p]+=out_p;
}
else
{
azi[p]+=(360-out_p);
}

    chance=-1*chance;
azi[p]=azi[p]%360;
p_st[p]=0;
p_mode[p]=1;
p_e[p]+=1;

    /** turn k vector into poyting vector **/
if(drand48()>(s_ang[polar[p]]-(int)s_ang[polar[p]]))
    polar[p]-=(short int)s_ang[polar[p]];
else
    polar[p]-=(1+(short int)s_ang[polar[p]]);
}
}

break;

```

```

    }
}
if((j==100)|| (j==200)|| (j==500)|| (j==50)|| (j%dsteps)==0)
{
    sprintf(fname1,"%s_o_%d",fname,j);
    sprintf(fname2,"%s_e_%d",fname,j);
    ftp1=fopen(fname1,"w");
    ftp2=fopen(fname2,"w");
    for(p=0;p<1000;p++)
    {
        if(p_mode[p]==0)
            fprintf(ftp1,"%e\t%e\t%e\n",photon[p].x,photon[p].y,photon[p].z);
        else
            fprintf(ftp2,"%e\t%e\t%e\n",photon[p].x,photon[p].y,photon[p].z);
    }
    fclose(ftp1);
    fclose(ftp2);
}
}
sprintf(fname1,"%s_log",argv[3]);
ftp1=fopen(fname1,"w");
fprintf(ftp1,"d_t=%e\n",dt);
fclose(ftp1);
return 0;
}

```

```

/* utilities function for vector */

double dot(vector a, vector b)
{
    return a.x * b.x + a.y * b.y + a.z * b.z;
}

vector timeconst(double a, vector v)
{
    vector vv;
    vv.x=v.x*a;
    vv.y=v.y*a;
    vv.z=v.z*a;
    return vv;
}

vector SVT( double a1, double a2, double a3)
{
    vector v;

    v.x=a1;
    v.y=a2;
    v.z=a3;
    return v;
}

void CallInVectors(double t_in,double p_in)

```

```

{
  double tin,pin,K,n1,a,b,D_angle,sn,cs;

  tin=t_in*dg;
  pin=p_in*dg;
  sn=sin(tin);
  cs=cos(tin);

  eki.x=sn*cos(pin);
  eki.y=sn*sin(pin);
  eki.z=cs;

  K=no*freq/c;
  ki[0]=timeconst(K,eki);
  n1=1.0/sqrt(cs*cs/Eo+sn*sn/Ee);

  n_i[1]=n1;
  K=n1*freq/c;
  ki[1]=timeconst(K,eki);

  if(t_in>90)
  {
    D_angle=atan(nr2*tan(tin-0.5*pi));
    d_i[1]=D_angle-(tin-0.5*pi);
    a=D_angle;
  }
  else
  {

```

```

    D_angle=pi+atan(nr2*tan(tin+0.5*pi));
    d_i[1]=0.5*pi+tin-D_angle;
    a=D_angle;
}

b=pin;
E_e=a/dg;
i[0]=SVT( sin(b),-cos(b),0);
i[1]=SVT( sin(a)*cos(b),sin(a)*sin(b),cos(a));
if(t_in==90)
{
    i[0]=SVT(0,-1,0);
    i[1]=SVT( 0,0,1);
}

}

```

```

void CalOutVectors(double t_out,double p_out)
{
    double K,n1,a,b,D_angle,sn,cs,tout,pout;

    tout=t_out*dg;
    pout=p_out*dg;
    sn=sin(tout);
    cs=cos(tout);
    eko.x=sn*cos(pout);
    eko.y=sn*sin(pout);
    eko.z=cs;
}

```

```

K=no*freq/c;
ko[0]=timeconst(K,eko);
n1=1.0/sqrt(cs*cs/Eo+sn*sn/Ee);
n_o[1]=n1;
K=n1*freq/c;
ko[1]=timeconst(K,eko);

if(t_out>90)
{
D_angle=atan(nr2*tan(tout-0.5*pi));
d_o[1]=D_angle-(tout-0.5*pi);
a=D_angle;
}
else
{
D_angle=pi+atan(nr2*tan(tout+0.5*pi));
d_o[1]=0.5*pi+tout-D_angle;
a=D_angle;
}

b=pout;
f[0]=SVT( sin(b),-cos(b),0);
f[1]=SVT( sin(a)*cos(b),sin(a)*sin(b),cos(a));

if(t_out==90)
{
f[0]=SVT(0,-1,0);

```

```

    f[1]=SVT(0,0,1);
}
}

void CalQVectors()
{
    double a,b;

    q[0][0]=SVT( ko[0].x-ki[0].x,ko[0].y-ki[0].y,ko[0].z-ki[0].z);
    q[0][1]=SVT( ko[1].x-ki[0].x,ko[1].y-ki[0].y,ko[1].z-ki[0].z);
    q[1][0]=SVT( ko[0].x-ki[1].x,ko[0].y-ki[1].y,ko[0].z-ki[1].z);
    q[1][1]=SVT( ko[1].x-ki[1].x,ko[1].y-ki[1].y,ko[1].z-ki[1].z);
    b=(sqrt(q[0][0].x*q[0][0].x+ q[0][0].y*q[0][0].y));

    if(b!=0)
        a=1.0/b;
    else
        a=0.0;

    e[0][0][0]= SVT( a*q[0][0].x,a*q[0][0].y,0);
    e[0][0][1]= SVT( a*q[0][0].y,-a*q[0][0].x,0);
    b=(sqrt(q[1][0].x*q[1][0].x+ q[1][0].y*q[1][0].y));

    if(b!=0)
        a=1.0/b;
    else
        a=0.0;
}

```

```

e[1][0][0]= SVT( a*q[1][0].x,a*q[1][0].y,0);
e[1][0][1]= SVT( a*q[1][0].y,-a*q[1][0].x,0);
b=(sqrt(q[0][1].x*q[0][1].x+ q[0][1].y*q[0][1].y));

if(b!=0)
    a=1.0/b;
else
    a=0.0;

e[0][1][0]= SVT( a*q[0][1].x,a*q[0][1].y,0);
e[0][1][1]= SVT( a*q[0][1].y,-a*q[0][1].x,0);
b=(sqrt(q[1][1].x*q[1][1].x+ q[1][1].y*q[1][1].y));

if(b!=0)
{
    a=1.0/b;
    e[1][1][0]= SVT( a*q[1][1].x,a*q[1][1].y,0);
    e[1][1][1]= SVT( a*q[1][1].y,-a*q[1][1].x,0);
}
else
{
    e[1][1][0]= SVT( 1.0,0,0);
    e[1][1][1]= SVT( 0,1.0,0);
}
}

/** Function to calculate differential cross-section */

```

Bibliography

- [1] R. Brown, *Philos. Mag.* **4**, 161(1828);
- [2] A. Einstein, *Ann. Physik* **17**, 549 (1905); **19**, 371 (1906).
- [3] A. Rahman *Phys. Rev. A* **136**, 405(1964).
- [4] B. J. Alder and T. E. Wainwright, *Phys. Rev. A* **1**, 18 (1970);
- [5] R. Zwanzig and M. Bixon, *J. Fluid Mech.* **69**, 21 (1975).
- [6] E. J. Hinch, *J. Fluid Mech.* **72**, 499 (1975).
- [7] D. A. Weitz, D. J. Pine, P. N. Pusey, and R. J. A. Tough, *Phys. Rev. Lett.* **63**, 1747 (1989).
- [8] J. X. Zhu, D. J. Durian, J. Müller, D. A. Weitz, and D. J. Pine, *Phys. Rev. Lett.* **68**, 2559 (1992).
- [9] G. Maret and P. E. Wolf, *Z. Phys. B* **65**, 409 (1987).
- [10] M. J. Stephen, *Phys. Rev. B* **37**, 1(1988).
- [11] D. J. Pine, D. A. Weitz, J. X. Zhu, and E. Herbolzheimer, *J. Phys. France* **51**, 2101 (1990).
- [12] A. G. Yodh, N. Georgiades and D. J. Pine, *Optics Communications* **83**, 56 (1991).

- ✓ [13] M. H. Kao, A. G. Yodh and D. J. Pine, Phys. Rev. Lett. **70**, 242-245(1993).
- [14] H. C. van de Hulst, *Light Scattering by Small Particles*, 124
- [15] Vlasov, D.V., Zubkov, L., Orekhova, N., and Romanov, V., JETP Lett . **48**, 91(1988).
- [16] P. N. Pusey and R. J. A. Tough(1981). In *Dynamic light scattering: applications of photon correlation spectroscopy*(ed. R. Pecora). Plenum Press, New York.
- [17] Vithana H., Asfaw, L., and Johnson, D.L., Phys. Rev. Lett. **70**, 3561(1993)
- [18] T. C. Lubensky and Holger Stark, submitted to Phys. Rev. Lett.
- [19] H. M. Lindsay, Ph.D. dissertation, *The Elastic And Viscous Properties of Colloidal Crystals*, UCLA(1988).
- [20] P. D. Kaplan, Ph.D. dissertation, *Optical Studies of the Structure and Dynamics of Opaque Colloids*, U. PENN(1993). A. J. C. Ladd, H. Gang, J. X. Zhu, and D. A. Weitz, Phys. Rev. Lett. **72**, 318-321(1995).
- ⊙ [21] R. H. Pathria, *Statistical Mechanics*, Pergamon Press, Oxford.
- [22] A. Ishimaru, *Wave propagation and scattering in random media* Academic Press, New York(1978).
- [23] M. P. Van Albada, B. A. van Tiggelen, A. Lagendijk, and A. Tip, Phys. Rev. Lett. ,**66**, 3132(1991).
- [24] S. Feng, C, Kane, P. A. Lee, and A. D. Stone, Phys. Rev. Lett. **61**, 834(1988).
- [25] M, Stephen and G. Cwilich, Phys. Rev. Lett., **59**, 285.
- [26] F. C. MacKintosh, J. X. Zhu, D. J. Pine, and D. A. Weitz, Phys. Rev. B, **40**, 9342(1989).

- [27] S. Fraden and G. Maret, Phys. Rev. Lett., **65**, 512(1990).
- [28] A. J. C. Ladd, Phys. Rev. Lett., **70**, 1339-1342(1993).
- [29] P. E. Wolf and G. Maret in *Scattering in Volumes and Surfaces*, edited by M. Nieto-Vesperinas and J. C. Dainty (Elsevier, Amsterdam, 1990),p.37; T. Bellini, M. A. Glaser, N. A. Clark, and V. Degiorgio, Phys. Rev. A **44**, 5215 (1991).
- [30] H. S. Carslaw and J. C. Jaeger, *Conduction of Heat in Solid*. 2nd ed. (Clarendon, Oxford,1959).
- [31] P. D. Kaplan, A. G. Yodh, and D. J. Pine, Phys. Rev. B, **83**,4744(1990).
- [32] J. Zhu, Ph.D. thesis, City University of New York, 1992.
- [33] J. L. Lebowitz, Phys. Rev. A **133**, 895 (1964).
- [34] C. W. J. Beenakker and P. Mazur, Physica **120A**, 388 (1983); C. W. J. Beenakker and P. Mazur, Physica **126A**, 349 (1984).
- [35] D.J. Durian, Appl. Optics. **34**, 7100-7105(1995)
- [36] C. W. J. Beenakker, Physica **128A**, 48(1984).
- [37] J. X. Zhu, D. J. Pine, and D. A. Weitz, Phys. Rev. A **44**, 3948-3959(1991).
- [38] F. C. MacKintosh and S. John, Phys. Rev. B, **40**, 2838(1989).
- [39] M. S. Wertheim, Phys. Rev. Lett. **10**, No. 8, 321-323(1963).
- [40] P. G. de Gennes and J. Prost, *The Physics of Liquid Crystals*, Oxford Science Publications(1993)
- [41] P. Chatelain, *Acta Crystallogr.* **1**, 315(1948).
- [42] A. Yu. Val'kov and V. P. Romanov, Sov. Phys. JETP **63**(4), 737-743(1986)

- [43] V. L. Kuz'min, V. P. Romanov, L. A. Zubkov, Phys. Rep. **248**, 71(1994).
- [44] J. L. Ericksen, Phys. Fluids **9**, 1205(1966).
- [45] F. M. Leslie, Arch. ration. Mech. Analysis **28**, 265(1968).
- [46] O. J. Parodi, J. Phys.(Paris) **31**, 581(1970).
- [47] D. Forster, T. Lubensky, P. Martin, J. Swift, and P. Pershan, Phys. Rev. Lett. **26**,1016(1971)
- [48] N. V. Madhusudana and R. Pratibha, Mol. Cryst, Liq. Cryst., 1982, **89**,249-257.